Galvanomagnetic and thermonagnetic effects, in quenched bismuth

Sumengen, Ziya

GALVANOMAGNETIC AND THERMOMAGNETIC EFFECTS IN QUENCHED BISMUTH

A thesis submitted to the University of Durham

for the degree of

Doctor of Philosophy

by

Ziya Sümengen

Department of Applied Physics and Electronics

University of Durham

November 1971

ABSTRACT

An experimental study of the quenching effects on the galvanomagnetic and thermomagnetic properties of bismuth single crystals is presented. Measurements made include components of the magnetoresistivity and magnetothermoelectric power tensors at low and intermediate magnetic fields for samples in both the annealed and quenched conditions, at temperatures between 77°K and room temperature. Marked effects of quenching on each set of tensor components have been observed. After quenching the anisotropy ratio ρ_{11}/ρ_{33} of the zero field resistivity inverts from 0.9446 to 1.030 and the thermomagnetic data show a general reduction in magnetic field dependence. The quenching effects anneal out below room temperature.

To allow a detailed quantitative investigation, a formalism has been developed by which the thermomagnetic data and the predictions of both the phenomenological theory and of the band transport theory can be compared on the same basis as the galvanomagnetic effects. The expressions provide for the first time an analytical explanation for the Umkehr effect and lead to its prediction. The occurrence of Umkehr effect and sign reversal in the thermomagnetic power of bismuth directly follows from the nature of the Fermi surface.

Measurements at low and intermediate magnetic fields have been analysed in terms of a two-band multi-valley Fermi surface model, using a least-means-square procedure. Reasonable agreement

obtains between the model parameters computed from different sources. Magnetoresistivity data at low and intermediate fields evidence consistent quenching-induced changes on the model parameters. Quenching results in an increase in carrier densities from 4.4 $10^{23}m^{-3}$ in annealed state to 4.6 $10^{23}m^{-3}$ and 5.3 $10^{23}m^{-3}$ for electrons and holes respectively. Carrier mobilities in the xy-plane are reduced but those along the trigonal (z) axis are increased slightly. The energy separation between the band edges increases markedly. Quenched-in defects have predominantly accepter-like character.

ACKNOWLEDGEMENT

I am greatly indebted to Dr. G.A. Saunders for initiating this research topic and enthusiastically guiding its progress.

I wish to thank Professor D.A. Wright for providing many facilities and the Scientific and Technical Research Council of Turkey for their financial support.

My thanks also go to the technical staff led by Mr. F. Spence for their friendly and valuable help, in particular to Mr. R. Waite. Thanks also to Mrs. Nichols and Mrs. Henderson for their careful typing of the thesis and to my friends, the research group for many cheerful and memorable discussions.

Finally, I thank my wife, for her understanding and patient help in many ways.

CONTENTS

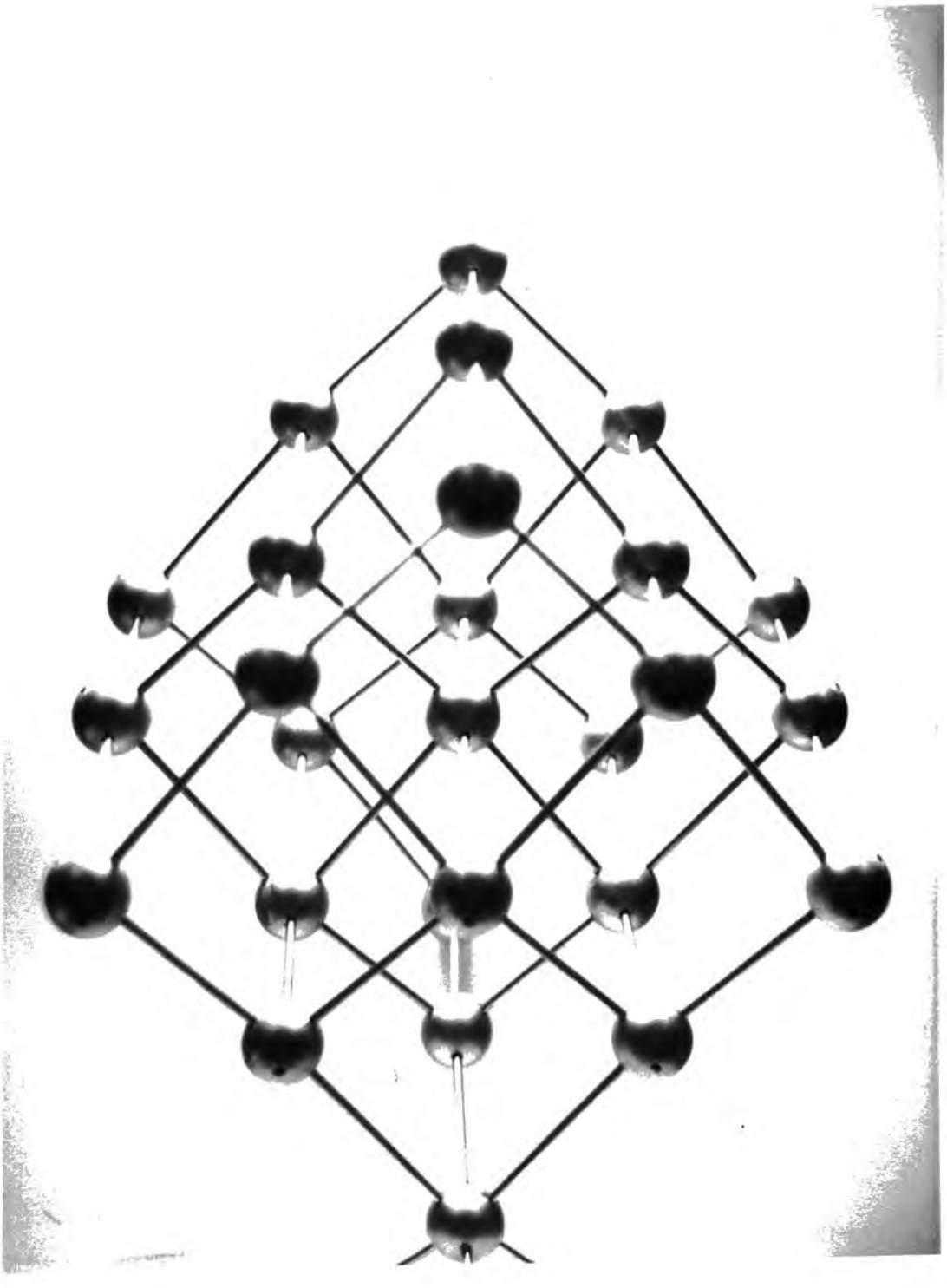

The rhombohedral ($\bar{3}$m), A7 crystal structure of bismuth, viewed along the bisectrix (y) axis.

CHAPTER I

INTRODUCTION

Interpretation of carrier transport properties on the basis of electron band theory has led to major contributions in our understanding of the electrical conduction in solids. Certain transport effects, particularly the Hall effect and magnetoresistance, are frequently used as tools for the investigation of the Fermi surface of semimetals and metals. By virtue of their unique carrier properties the semimetals bismuth, antimony and arsenic play a special role in experimental studies of transport effects. The presence, in these materials, of carriers with small effective masses, high carrier mobilities and long relaxation times results in large changes, as compared with those in metals, in the thermoelectric power and electrical resistivity in the presence of a magnetic field. In bismuth in particular the carrier transport properties are dramatic; many of the fundamental properties, among them the Hall, Ettinghausen, Nernst, de Haas - van Alphen, Shubnikov - de Haas effects were first discovered in this semimetal.

The galvanomagnetic effects in semimetals have been extensively studied. Combined application of the results of the phenomenological theory and band theory has resulted in correlation of the experimental observations with the main features of the Fermi surface model. Thus the low field tensor components of bismuth (Abeles and Meiboom 1956, Zitter 1962, Hartman 1969), antimony (Öktü and Saunders 1967) and arsenic (Jeavons and Saunders 1969) have been measured and interpreted

using multivalley, ellipsoidal Fermi surface models; the marked anisotropy of the galvanomagnetic effects in semimetals has been directly connected to the Fermi surface topology. As a result of these and other extensive studies, the features of the low field galvanomagnetic tensors have been explained satisfactorily. But the thermomagnetic effects are less well understood and studies of these effects have contributed little to this end. Large, anisotropic magnetothermoelectric effects in bismuth with unusual features, not hitherto accounted for on a formal basis, have been observed. On magnetic field reversal the magnetothermoelectric voltage alters for certain crystallographic directions (Grüneisen and Gielessen 1936), a property usually termed the Umkehr or commutation effect; this behaviour is particularly marked for the thermomagnetic voltage measured along the y-axis when a temperature gradient is developed along that direction and the magnetic field directed either along the +x or -x axis (Smith et al. 1964, Gitsu et al. 1970 and Michenaud et al. 1970); a sign reversal occurs, when the magnetic field is made sufficiently large; striking polar diagrams of the thermoelectric voltage have been obtained, when the magnetic field is taken around the xz-plane.

A treatment of the thermomagnetic data on a similar basis as that used for the galvanomagnetic effects has been considered necessary. This should answer the open questions as to whether the interesting features observed in the thermomagnetic power can be accounted for from the results of both the phenomenological theory and the band theory. One of the objectives in this work has been

to develop such a formalism by which the results of the thermomagnetic data and the predictions of the phenomenological theory and the established Fermi surface model could be related and compared. The basic reason for this part of the study has been to lay a firm foundation on which to base a quantitative investigation of the effect of quenched-in defects on the transport properties.

All crystalline structures contain point defects; in fact, a real crystal without point defects can not be in thermodynamic equilibrium at temperatures above absolute zero. The presence of point defects follows as a condition of the thermodynamical equilibrium and the equilibrium concentration of point defects at a temperature T is given by (Damash and Dienes 1963)

$$\frac{n}{N} = e^{-E/kT} \qquad (1\text{-}1)$$

where E is the defect formation energy and k is Boltmann's constant. Equation (1-1) shows that the defect concentration is zero at $0^{o}K$ and increases as the temperature rises. Thus this equation determines the optimal condition corresponding to maximum defect concentration at premelting temperatures. An excess of frozen-in defects can be produced at a low temperature T_e by quenching from a high temperature T_a at which the equilibrium concentration of point defects is high. The excess defect concentration created through quenching can then be used in the investigation of changes induced by point defects or the characteristics of defects themselves.

Quenching techniques have been extensively employed to investigate defect induced changes in physical properties of crystalline solids. The imperfections introduced influence most strongly those properties that are structure sensitive, such as density and volume. Early studies of point defects were carried out on ionic crystals and many properties of colour centres were explained. In turn an interpretation of more complex behaviour of technically important substances, such as photographic emulsion and luminescent materials resulted. Similar theoretical and experimental techniques have shown that point defects play an important role in semiconductors and in aspects of semiconductor technology. Point defects and the distorted regions around them scatter the electrons and thus manifest themselves in changes in the electrical resistivity; by behaving as acceptors and donars they can also change the carrier densities.

Although quenching techniques have been used to study extensively the behavoiur of frozen-in defects in metals, no previous work on the group V semimetals appears to have been carried out. Nor are there detailed measurements of the magnetoresistivity and thermomagnetic power measurements in metals, although much of the knowledge of the behaviour of point defects has accrued from the direct approach of resistivity measurements (see Burton and Lazarus 1970, for a recent study and earlier references). In pure metals the resistivity changes produced by quenching are small. No measurable variations are found in the Fermi level or the Fermi surface or in the carrier density.

Bismuth lends itself well to an investigation of the effects of quenched-in defects on the carrier transport properties. Pronounced

effects might well be anticipated because the carrier density in this material is low (each band contains only 4.4×10^{17} carriers/cm^3 at 77°K) and the band overlap is small (0.036 eV). A marked shift in the Fermi level and in the carrier density should ensue from the creation of defects which either donate or accept carriers. Carrier effective masses are very small and the relaxation times long; carrier mobilities are high; quenched-in defects would be expected to increase the carrier scattering and lead to an alteration in the carrier mobilities. Because of the direct dependence of most of the tensor components on the carrier density and mobilities, measurements of the galvanomagnetic and thermomagnetic effects on quenched samples should provide quantitative information on the effects of quenched-in defects on these parameters.

CHAPTER II

THE CRYSTAL STRUCTURE AND THE FERMI SURFACE OF BISMUTH

I INTRODUCTION

The group - V semimetals bismuth, antimony and arsenic crystallise in the rhombohedral, A7 structure (space group $\bar{3}m$), which has two atoms in each unit cell. Their electrical properties reveal certain characteristics typical of metals and others like those of semiconductors. For example on the one hand the occurrence of relatively high electrical conductivity with a positive temperature coefficient, at all temperatures resembles metallic behaviour. On the other hand carrier properties, such as density, energy, effective mass and mobility, and their sensitivities to impurities and defects are similar to those observed in semiconductors. Because there are two atoms in the unit cell, each contributing five valence electrons, there are just sufficient electrons to be accommodated by the first five Brillouin zones. Thus, depending on the width of the gap between the conduction and valence bands either semiconducting or semimetallic behaviour could result. However in the A7 structure semimetallic behaviour is the rule because there is a small energy overlap between the fifth and sixth energy bands; this creates equal numbers of holes and electrons in small, nearly ellipsoidal pockets. Cohen, Falicov and Golin (1964) have shown that most of the qualitative features of the energy bands and semimetallic characters result directly from the rhombohedral A7 crystal structure itself. Therefore

it is worthwhile examining this particular crystal structure in more detail.

II THE A7 CRYSTAL STRUCTURE

The space lattice adopted by bismuth, antimony and arsenic is in the rhombohedral system. It can be obtained from the cubic lattice by small displacements of the atoms. This is best illustrated by reference to the NaCl structure, which is made up of two independent face centred cubic lattices, one of which contains the cation and the other the anion. The A7 structure can be generated by the application of two independent distortions, figure (2-1):

1 - The sublattices formed by Na and Cl atoms, which in the case of group - V semimetals are occupied by identical ions, are displaced along a body diagonal with respect to one another.

2 - A pull along the body diagonals to transform each sublattice into a face-centred rhombohedron.

The resulting face centred rhombohedral lattice contains four primitive rhombohedral cells, each with two atoms. The primitive rhombohedral translation vectors can also be generated in the same way from the face-centred cubic structure by including the effect of the distortion. They are

$$\begin{aligned} \bar{a}_1 &= a_o\{\epsilon\ ,\ 1,\ 1\} \\ \bar{a}_2 &= a_o\{\ 1,\ \epsilon\ ,\ 1\} \\ \bar{a}_3 &= a_o\{1,\ 1,\ \epsilon\} \end{aligned} \qquad (2\text{-}1)$$

where a_o is the half of the face-centred cubic lattice parameter and is related to the primitive rhombohedral angle α by

$$\cos\alpha = (1 + 2\epsilon) / (2 + \epsilon^2) \qquad (2\text{-}2)$$

The amount of distortion differs for each of the elements and can be indicated by the primitive rhombohedral angle α and an internal displacement parameter $u\ (= \frac{\tau}{d})$, where d is the length of the rhombohedral body diagonal and 2τ is the smallest distance between the two atoms along this diagonal direction. These parameters, in comparison to the cubic case, for the three isomorphous elements bismuth, antimony and arsenic are:

Element		
Bi	57° 19'	0.237
Sb	57° 14'	0.234
As	54° 10'	0.226
Cubic	60°	0.250

The distortion of bismuth and antimony from a cubic structure is small: some directions, which would be symmetry axes in a cubic structure, still produce back reflection Laue X-ray pictures which look as if the symmetry is preserved. Such directions are usually referred to by the prefix "pseudo". An orthogonal set of crystalogrphic coordinates is usually defined as follows. The binary (x) axis is normal to any one of the three mirror planes, mutually oriented at 120°, which intersects in a threefold inversion (z) axis.

The bisectrix (y) axis is in the mirror plane and completes the right handed orthogonal set. However for the A7 structure this choice of the coordinate system is not complete; it introduces ambigiuties in defining the sign of some tensor components and hence the sense of ellipsoidal angle of tilt (see Öktu 1967, Öktü and Saunders 1967, Brown et al 1968). The usual convention for definition of a right handed coordinate system is based on the geometry of the basis vectors of the primitive rhombohedral unit cell: the positive z-axis is taken along the body diagonal of the primitive rhombohedral unit cell defined by the lattice translation vectors $\bar{a}_1$, $\bar{a}_2$ and $\bar{a}_3$ of equation (2-1). The y-axis is then defined by projecting one of the $\bar{a}_i$ on to the trigonal plane: the positive y direction is taken outward from the origin O of the $\bar{a}_i$ (see figure 2-2). A positive x-axis completes the right handed set.

III THE BRILLOUIN ZONE

The Brillouin zone can be obtained by geometrical construction in the reciprocal lattice. The reciprocal lattice vectors are defined in terms of the real space vectors by

$$\bar{g}_i = 2\pi \frac{\bar{a}_j \wedge \bar{a}_k}{\bar{a}_i(\bar{a}_i \wedge \bar{a}_k)} \qquad (2\text{-}3)$$

When the primitive translation vectors $\bar{a}_i$, are substituted into equation (2-3), we have for the reciprocal lattice vectors:

$$\begin{aligned} \bar{g}_1 &= g_o\{-(1+\epsilon), 1, 1\} \\ \bar{g}_2 &= g_o\{1, -(1+\epsilon), 1\} \\ \bar{g}_3 &= g_o\{1, 1, -(1+\epsilon)\} \end{aligned} \qquad (2\text{-}4)$$

where $g_o = (1-\epsilon)/a_o(\epsilon^3 - 3\epsilon + 2)$. The reciprocal lattice for the A7 structure is also a distortion of the reciprocal lattice for the face centred cubic structure; the cube, and hence the Brillouin zone is compressed along one of the body diagonals. Figure (2-3) shows the first Brillouin zone constructed inside this slightly distorted cubic structure. The compression is along the trigonal (TT) direction. The hexagonal faces containing T are still regular hexagons but the other six hexagonal faces are irregular and the six square faces are now rectangles. The symmetry elements of the Brillouin zone are the same as those of crystal lattice. Therefore the ambiguity of the definition of a right handed axial set in real space is carried through into reciprocal space. In the mirror plane ΓTLX (see figure (2-4)), rotations from the trigonal axis ΓT by equal amounts in opposite directions are not equivalent. The sense of rotation may be such as to tip the trigonal axis ΓT towards either the L points or the X points. Hence the directional dependence of parameters in this plane must be described with reference to the geometry of the basis vectors of the primitive rhombohedral unit cell of the Bravais lattice. The conversion, defining a positive angle in the mirror plane, corresponds to the tilting of +y through the first quadrant toward +z (see figure (2-4)). Thus the ellipsoid in this figure has its major axes tilted by a small positive angle from the bisectrix direction. These points will be used at appropriate places throughout this thesis.

IV THE FERMI SURFACE OF BISMUTH

The Pauli exclusion principle determines the way in which the electrons occupy the energy states available to them; the lowest energy

states are filled first and then the states in order of increasing energy. At the absolute zero of temperature the boundary between the occupied and unoccupied states is sharp; this boundary, which occurs at the constant energy surface, at the so-called Fermi energy, is known as the Fermi surface. For the case of a simple free electron gas, the surfaces of constant energy are spheres in $\underline{k}$-space; and so the Fermi surface is a sphere. Electrons well inside the Fermi surface cannot be excited thermally or by electric or magnetic fields becasuse the states within the appropriate energy range are already occupied. Only the electrons near the Fermi surface can be excited and hence electron transport is mainly due to these electrons. This approach of using weakly excited states of carriers located in the vicinity of the Fermi surface is preferred in band theory because of the difficulties in describing the interactions of the quasi particles in terms of an average field. However in a real solid neither this idealized spherical Fermi surface nor the simple excitation model can be a true description; but the main ideas leading to an understanding of electrical conduction are essentially valid and an appropriate Fermi surface topology developed along these lines lays the foundation for the study of transport properties.

Most of the experimental and theoretical techniques available for band structure determinations have been employed in the Fermi surface studies of bismuth, in fact, many of them were first discovered in this semimetal. The de Haas - van Alphen effect (Shoenberg 1939, Brandt 1960, Bhargava 1967) Azbel' - Kaner cyclotron resonance experiment (Aubrey et al 1957, Galt et al 1959),

galvanomagnetic effects (Abeles and Meiboom 1956, Zitter 1962, Hartman 1969), anamalous skin effect (Aubrey 1961), infrared measurements (Boyl et al 1960) and ultrasonic attenuation (Giura et al 1967) to name some have all been investigated thoroughly. As a result the main features of bismuth's Fermi surface are established (Figure 2-5). The electron Fermi surface consists of three geometrically equivalent, extremely prolate ellipsoids, with each ellipsoid centred about an energy minimum at L points on the six irregular hexagonal faces of the Brillouin zone. These energy minima lie in the three reflection planes. Each electron ellipsoid has one principal axis coincident with an axis of two fold symmetry - there are three of these, each obtainable from the others by a rotation of $\pm$ 120° about the trigonal axis - while the other ellipsoid principal axes lie in the mirror plane. The energy dispersion relation, in momentum space is then

$$2\epsilon = \bar{p}\,\hat{\alpha}\,\bar{p} = (\alpha_{11}p_1^2 + \alpha_{22}p_2^2 + \alpha_{33}p_3^2 + 2\alpha_{23}p_2p_3) \qquad (2\text{-}5)$$

where 1, 2 and 3 refer to the binary, bisectrix and trigonal axes respectively. The α_{ij} are the components of the inverse electron effective mass tensor. Geometric equivalence of the electron ellipsoids is obtained by the application of $\pm$ 120° rotations around the trigonal axis. The Fermi surface for the holes consists of a single ellipsoid of rotation about the trigonal axis probably sited at T, the centre of the two regular hexagonal faces of the Brillouin zone. The energy dispersion relation in momentum space corresponding to this pocket of holes is

$$2\epsilon = \bar{p}\,\hat{\beta}\,\bar{p} = \beta_{11}p_1^2 + \beta_{11}p_2^2 + \beta_{22}p_3^2 \qquad (2\text{-}6)$$

where the β_{ij} are the components of the inverse hole effective mass tensor.

The inverse effective mass tensors $\hat{\alpha}$ and $\hat{\beta}$ are related to the mobility tensors $\hat{\mu}$ and $\hat{\nu}$ for electrons and holes by

$$\hat{\alpha} = \hat{\mu} / e\tau = \begin{bmatrix} \alpha_{11} & 0 & 0 \\ 0 & \alpha_{22} & \alpha_{23} \\ 0 & \alpha_{23} & \alpha_{33} \end{bmatrix} \qquad (2\text{-}7)$$

and

$$\hat{\beta} = \hat{\nu} / e\tau = \begin{bmatrix} \beta_{11} & 0 & 0 \\ 0 & \beta_{11} & 0 \\ 0 & 0 & \beta_{33} \end{bmatrix} \qquad (2\text{-}8)$$

The ellipsoidal model described by equations (2-5) and (2-6), accounts quantitatively for most of the experimental data obtained. But Lax et al (1960) have suggested that the energy dispersion relation of the conduction band deviates significantly from that of the parabolic ellipsoidal model and have used a nonparabolic energy relation as

$$\epsilon \left(1 + \frac{\epsilon}{\epsilon_g}\right) = \bar{p}\, \hat{\alpha}\, \bar{p} \qquad (2\text{-}9)$$

where ϵ_g is a small energy gap between the valence and conduction bands. The experimental evidence indicates that the deviation of the electron Fermi surface from the ellipsoidal model is slight (Khaikin and Edel'man 1965, Bhargava 1967, Brandt 1963 and Korolyuk 1966).

The Fermi surface parameters for electrons and holes measured by different experimental techniques are listed in table (2-1).

The appropriate relationships for the galvanomagnetic and thermomagnetic effects based on the ellipsoidal Fermi surface model will now be developed.

TABLE (2-1)

EXPERIMENTAL METHOD	α_{11}	α_{22}	α_{33}	α_{23}	β_{11}	β_{33}	SOURCE
de Haas - van Alphen	420	0.8	40	4.0			Shoenberg (1939)
de Haas - van Alphen					20	1.43	Brandt (1960)
Cyclotron resonance	202	1.67	83.3	8.33			Aubrey et al (1957)
Cyclotron resonance	114	1.39	108	9.47	14.7	1.07	Galt et al (1959)
Acoustic attenuation	178	1.1	84.5	7.2			Reneker (1959)
Infrared absorption	133	1.2	91	6.1			Boyl et al (1960)
Anomalous skin effect	160	1.56	83	6.7	1.7	0.13	Smith (1959)

$\hat{\alpha}$ and $\hat{\beta}$ are in units of m_o

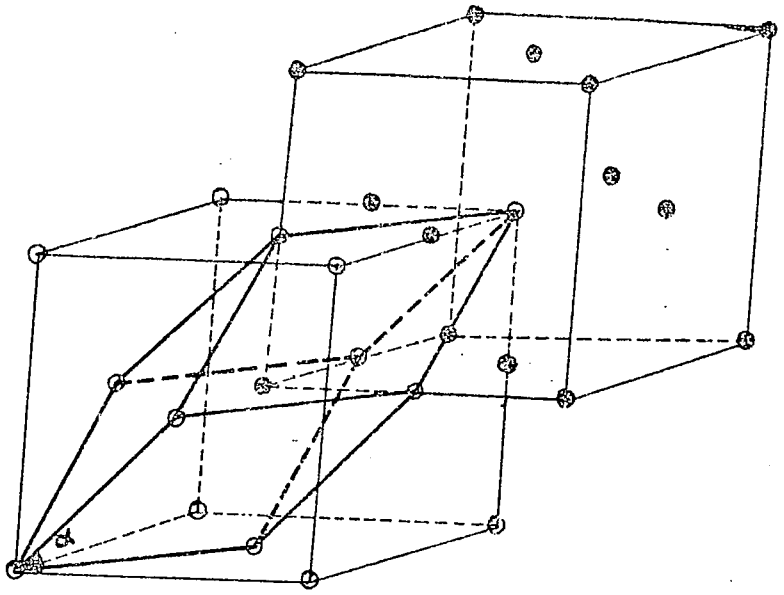

Figure (2-1) : The relationship between the cubic lattice and the rhombohedral unit cell of the A7 structure.

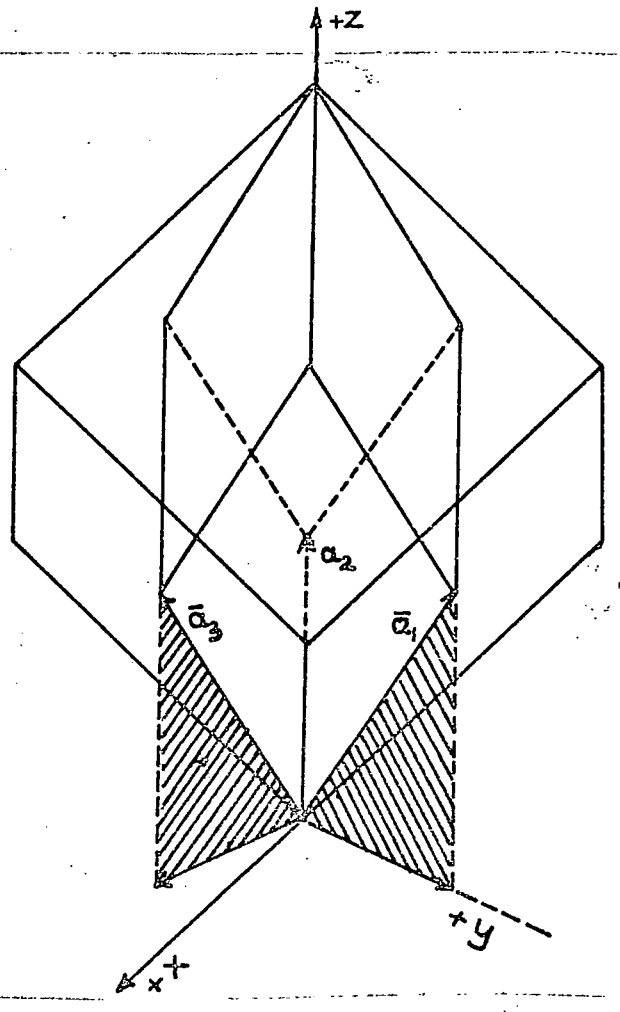

Figure (2-2) : The primitive rhombohedral cell sited inside the large face-centred rhombohedron. The primitive translation vectors are denoted by $\bar{a}_i$ (i = 1,2,3), y axis is chosen by projecting one of the $\bar{a}_i$ on to (1 1 1) plane and the positive direction points outwards from the origin O of the $\bar{a}_i$.

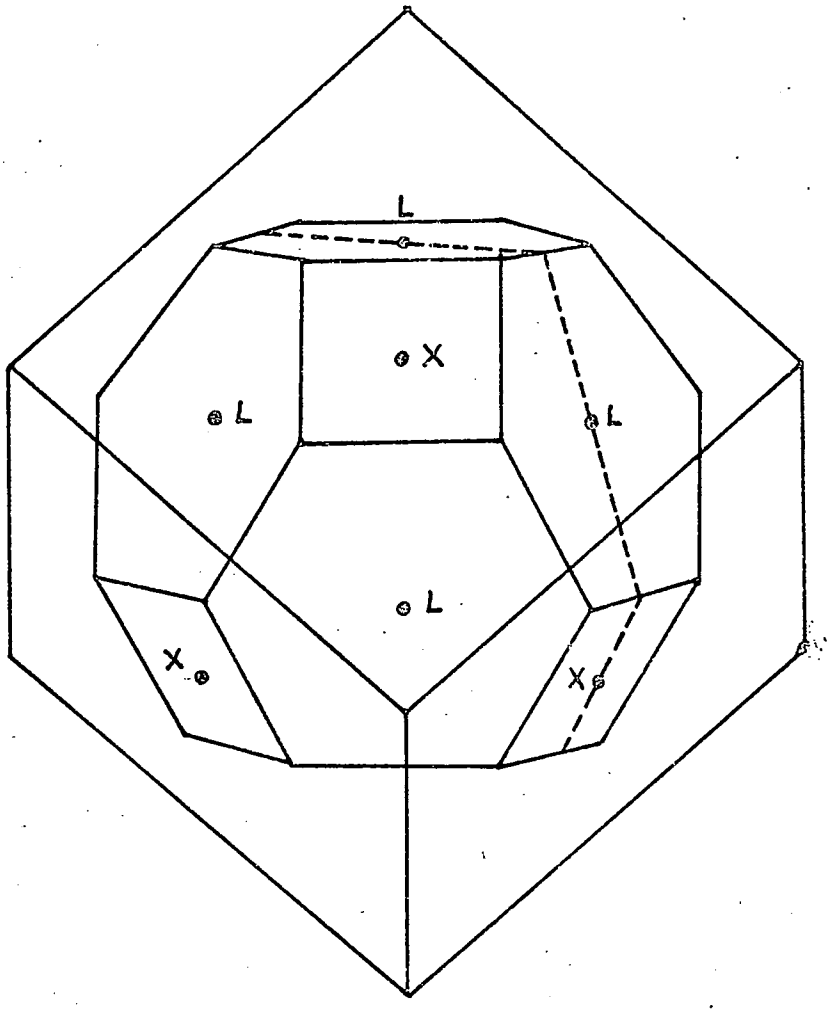

Figure (2-3) : The Brillouin zone of the slightly distorted face centred cubic lattice of Bismuth.

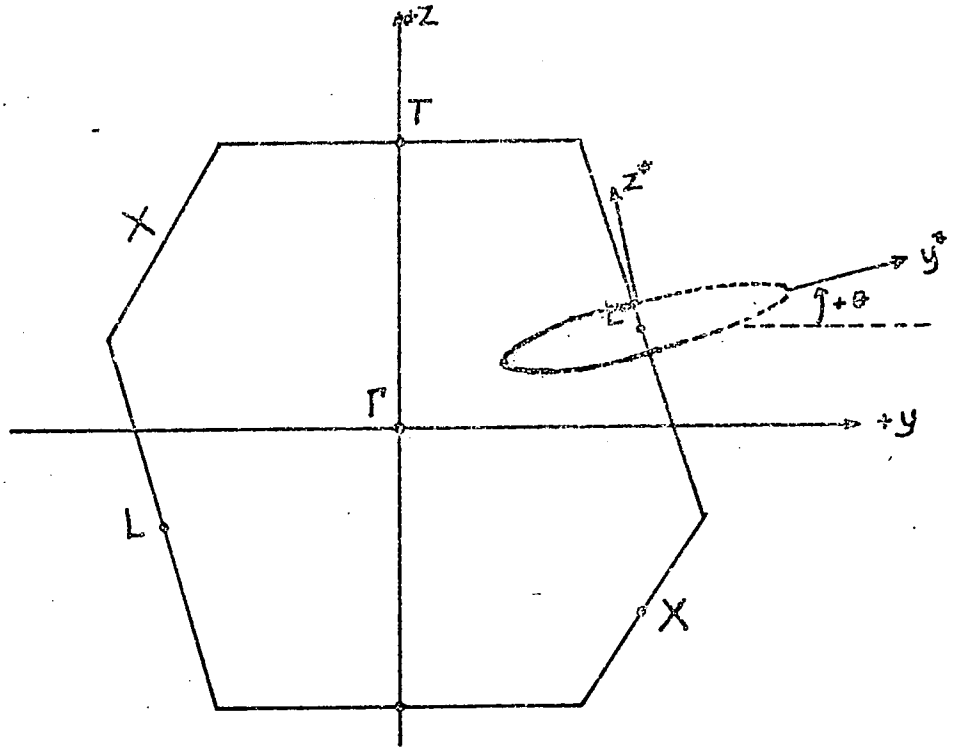

Figure (2-4) : A binary plane of the bismuth Brillouin zone showing the cross section of the electron Fermi surface in the neighbourhood of one L point. Positive tilt angle is indicated.

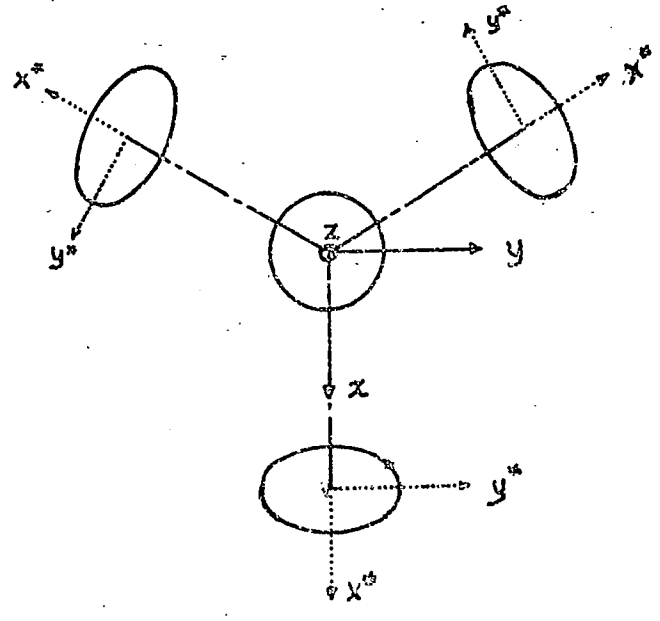

Figure (2-5) : Cross section of electron and hole ellipsoids in the trigonal plane.

CHAPTER III

THEORY OF GALVANOMAGNETIC AND THERMOMAGNETIC EFFECT IN BISMUTH

I INTRODUCTION

The Onsager formulation of the thermodynamics of irreversible processes has resulted in a rigorous phenomenological framework for defining the magnetotransport coefficients. In an anisotropic medium, the kinetic coefficients of thermogalvanomagnetic effects are tensors defined by the kinetic equations:

$$\bar{J} = \hat{\sigma}(\bar{B})\,\bar{E}^{*} + \hat{M}(\bar{B})\,\bar{\nabla}T$$

$$\bar{q} = \hat{N}(\bar{B})\,\bar{E}^{*} + \hat{L}(\bar{B})\,\bar{\nabla}T \qquad (3\text{-}1)$$

which express the electric and thermal current densities as linear combinations of the effective electromotive force $\bar{E}^{*}$ (which includes the thermodynamic force associated with the chemical potential of the electronic carriers and plays the role of measurable electric field) and the temperature gradient $\bar{\nabla}T$. The kinetic coefficients so defined are: $\hat{\sigma}(\bar{B})$ the electrical conductivity tensor, $\hat{M}(\bar{B})$ the thermoelectric tensor, $\hat{N}(\bar{B})$ the Peltier tensor and $\hat{L}(\bar{B})$ the thermal conductivity tensor.

An analytic calculation of the kinetic coefficients in equation (3-1) based on microscopic theory requires drastic specializations and simplifying assumptions. One useful model is due to Sondheimer and Wilson (Wilson 1959), which assumes conduction

by independent quadratic bands of carriers of either type each achieving equilibrium by a relaxation process and each contributing additively to the total conductivity. However, although the simple model of spherical energy surfaces employed is useful for some cubic materials, it fails to provide the anisotropy of galvanomagnetic effects. Some success in explaining the anisotropic galvanomagnetic effects in bismuth results from the single valley ellipsoidal model (Jones 1936). In particular, the large transverse magnetoresistance can be explained, but still no longitudinal magnetoresistance is predicted. A theory based on a model of several energy extrema at equivalent points in $\bar{k}$ - space and ellipsoidal energy surfaces centred on these points has been developed by Abeles and Meiboom (1954) and Herring (1955). This 'many-valley' model does predict the anisotropy associated with galvanomagnetic effects. On the basis of this model, quantitative analyses of galvanomagnetic effects in bismuth (Abeles and Meiboom 1956), antimony (Freedman and Juretschke 1961), Öktü and Saunders 1967) and arsenic (Jeavons and Saunders 1969) have been successfully carried out.

Expressions describing galvanomagnetic and thermomagnetic effects for such a model will now be derived by adopting the procedure of Mackey and Sybert (1969) to include the effect of thermal gradients.

II DERIVATION OF GALVANOMAGNETIC AND THERMOMAGNETIC TENSORS FOR ARBITRARY MAGNETIC FIELDS

The Boltzman equation in the relaxation time formalism for the carriers takes the form:

$$\bar{v}\cdot\bar{\nabla}_r f + \bar{\nabla}_p f\cdot[-e\bar{E} - e\bar{v}\wedge\bar{B}] + f_1/\tau = 0 \qquad (3\text{-}2)$$

where f_1 is the perturbation of the distribution function from the equilibrium value fo. The Boltzmann equation can be solved (Wilson 1959) by putting:

$$f_1 = -(\bar{p}\cdot\bar{C})\frac{\partial fo}{\partial \varepsilon} \qquad (3\text{-}3)$$

where $\bar{p}$ is the momentum and $\bar{C}$ is a function of the energy ε. For ellipsoidal Fermi surfaces the energy can be written as

$$2\varepsilon = \bar{p}\,\hat{\alpha}\cdot\bar{p} = \bar{p}\,\hat{m}^{-1}\cdot\bar{p} \qquad (3\text{-}4)$$

in the principal coordinate system of a particular ellipsoid. By use of the equations (3-3) and (3-4) the transport equation can be written as

$$-\bar{E} + \frac{T}{e}\bar{\nabla}\left(\frac{\varepsilon-\zeta}{T}\right) + (\bar{B}\wedge\bar{C}) - \frac{\hat{m}}{e\tau}\bar{C} = 0 \qquad (3\text{-}5)$$

where ζ is the thermodynamic potential of the carriers. Defining $\bar{P}$ as

$$\bar{P} = \bar{E}^* + \frac{1}{eT}(\varepsilon - \zeta)\,\bar{\nabla}_r T \qquad (3\text{-}6)$$

and $\bar{E}^* = \bar{E} + \frac{1}{e}\bar{\nabla}_r \zeta$

equation (3-5) becomes

$$-\bar{P} + (\bar{B}\wedge\bar{C}) - \hat{\mu}^{-1}\bar{C} = 0 \qquad (3\text{-}7)$$

Here $\hat{m}/e\tau$ is replaced by the inverse mobility tensor $\hat{\mu}^{-1}$ in the principle axis system of an ellipsoid. In tensor from

$$\hat{\mu} = \begin{bmatrix} \mu_1^* & 0 & 0 \\ 0 & \mu_2^* & 0 \\ 0 & 0 & \mu_3^* \end{bmatrix} \tag{3-8}$$

Equation (3-7) has a solution for $\bar{C}$ of the form

$$\bar{C} = \hat{G}^T \bar{P} \tag{3-9}$$

where

$$\hat{G} = (\hat{\mu}^{-1} \pm \hat{B})^{-1} \tag{3-10}$$

and

$$\hat{B} = \begin{bmatrix} 0 & -B_3 & B_2 \\ B_3 & 0 & -B_1 \\ -B_2 & B_1 & 0 \end{bmatrix} \tag{3-11}$$

The positive and negative signs apply for holes and electrons respectively.

The perturbation of the distribution function from equilibrium now can be found by substituting equation (3-9) into equation (3-3), when

$$f_1 = \bar{p} \cdot \hat{G}^T \bar{P} \cdot \frac{\partial f_o}{\partial \varepsilon} \tag{3-12}$$

Thus the cuffent density given by

$$\bar{J} = -2eh^{-3} \int \bar{v} \, f_1 \, d^3p \tag{3-13}$$

becomes

$$\bar{J} = 2eh^{-3} \int \bar{v} \; \bar{p} \cdot \hat{G}^T \bar{P} \; \frac{\partial f_o}{\partial \varepsilon} \; d^3 p \tag{3-14}$$

or using equation (3-6)

$$\bar{J} = 2e\, h^{-3} \int \bar{v}\, \bar{p}\cdot \hat{G}^T \bar{E}^* \frac{\partial f_o}{\partial \varepsilon} d^3 p \qquad (3\text{-}15)$$

$$+ 2e\, h^{-3} \int (\varepsilon - \zeta)\, \bar{v}\, \bar{p} \cdot G^T \bar{\nabla}_r T \frac{\partial f_o}{\partial \varepsilon} d^3 p$$

we now seek a form of this equation which can be compared directly with the phenomenological equation for the current density in equation (3-1). This requires expression of $\bar{J}$ in a linear combination of $\bar{E}^*$ and $\bar{\nabla}_r T$. To facilitate this a transformation

$$\bar{p} = a_o^{\frac{1}{2}} \hat{a}^{-\frac{1}{2}} \bar{W} \qquad (3\text{-}16)$$

$$\bar{v} = a_o^{\frac{1}{2}} \hat{a}^{\frac{1}{2}} \bar{W}$$

is introduced Fuchser, Mackey and Sybert (1970), which transforms the integration in equation (3-15) from ellipsoidal to spherical surfaces where the energy is expressed by

$$2\varepsilon = a_o \bar{W} \cdot \bar{W} \qquad (3\text{-}17)$$

An appropriate change of variables now permits the integration over spherical energy surfaces; terms containing multiples of $W_i W_j$ for $i \neq j$ vanish: $\bar{E}^*$ and $\bar{\nabla}_r T$ are independent of energy and can be carried outside the integral in vector from. The similarity to the phenomenological equations is hence achieved by

$$\bar{J} = \frac{16\sqrt{2}}{3} e\, h^{-3} \pi (m_1 m_2 m_3)^{\frac{1}{2}} \int \varepsilon^{3/2} (\hat{\mu}^{-1} \pm \hat{B})^{-1} \frac{\partial f_o}{\partial \varepsilon} d\varepsilon \quad \bar{E}^* \qquad (3\text{-}18)$$

$$+ \frac{z}{T} \frac{16\sqrt{2}}{3} h^{-3} \pi (m_1 m_2 m_3)^{\frac{1}{2}} \int (\varepsilon - \zeta) \varepsilon^{3/2} (\hat{\mu}^{-1} \pm \hat{B})^{-1} \frac{\partial f_o}{\partial \varepsilon} d\varepsilon \quad \bar{\nabla}_r T$$

The first part of equation (3-18) contains only even powers of

electronic charge so it is additive for different types of carriers. But in the second part odd powers are obtained and it is necessary to distinguish the electron contribution from that of the holes. This is done by introducing Z(= ± 1) and suffixing ($\epsilon - \zeta$). The comparison of equation (3-18) with the phenomenological equation (3-1) gives

$$\hat{\sigma}(\bar{B}) = \frac{16\sqrt{2}}{3} e h^{-3} \pi (m_1 m_2 m_3)^{\frac{1}{2}} \int \varepsilon^{3/2} (\hat{\mu}^{-1} \pm \hat{B})^{-1} \frac{\partial f_o}{\partial \varepsilon} d\varepsilon \tag{3-19}$$

$$\hat{M}(\bar{B}) = \frac{z}{T} \frac{16\sqrt{2}}{3} h^{-3} \pi (m_1 m_2 m_3)^{\frac{1}{2}} \int (\varepsilon - \zeta_{e,h}) \varepsilon^{3/2} (\hat{\mu}^{-1} \pm \hat{B})^{-1} \frac{\partial f_o}{\partial \varepsilon} d\varepsilon$$

Explicit evaluation of $\hat{\sigma}(\bar{B})$ and $\hat{M}(\bar{B})$ requires knowledge of the energy dependence of the relaxation time τ. Integration at the Fermi level avoids the complications which arise from the energy dependence of τ and we obtain for Fermi - Dirac statistics.

$$\hat{\sigma}(\bar{B}) = e n_{e,h} (\hat{\mu}^{-1} \pm \hat{B})^{-1} \tag{3-20}$$

and

$$\hat{M}(\bar{B}) = \frac{k}{ze} \left[\frac{5F_{3/2}(\eta_{e,h})}{3F_{\frac{1}{2}}(\eta_{eh})} - \eta_{e,h} \right] \hat{\sigma}(\bar{B}) \tag{3-21}$$

where F denotes the Fermi - Dirac integrals, and the partial reduced Fermi energies for electrons and holes are $\eta_{e,h} = \frac{\zeta_{e,h}}{kT}$. ζ_e and ζ_h are defined as ($\zeta - \varepsilon_c$) and ($\varepsilon_v - \zeta$) respectively, where ε_c is the energy of the bottom edge of the conduction band and ε_v that of the top edge of the valence band. Thus band overlap - $\Delta\varepsilon_g$ is measured from the top of the valence band to the bottom of the conduction band (Saunders and Öktü 1968).

Substituting equations (3-16) and (3-17) into (3-14) we get for the electric current density for a single valley

$$\bar{J} = \hat{\sigma}(\bar{B})\bar{E}^{*} + \frac{k}{ze}\left[\frac{5F_{3/2}(\eta_{e,h})}{3F_{\frac{1}{2}}(\eta_{e,h})} - \eta_{e,h}\right] \hat{\sigma}(\bar{B})\, \bar{\nabla}_{r}T \qquad (3\text{-}22)$$

The conductivity expression in its compact form (3-20) has been obtained by Mackay and Sybert (1969) and Aubrey (1971). Furthermore, Aubrey, starting from (3-20) has obtained the tensor components of $\hat{\bar{\sigma}}(\bar{B})$ for ellipsoidal Fermi surface in a form applicable to arsenic, antimony and bismuth.

We now turn to a description of $\hat{\sigma}(\bar{B})$ for the Fermi surface of bismuth (see sectn. II,IV) in particular.

III TOTAL CONDUCTIVITY EXPRESSIONS FOR BISMUTH

To calculate the total conductivity of a group of ellipsoids, one may assume that the conductivity of each ellipsoid can be calculated separately, the total conductivity is then given by summing the conductivities of the individual ellipsoids in a common reference system. Because the carrier concentrations in each ellipsoid in a given band are equal and $\bar{B}$ is already expressed in the crystallographic coordinate system, the only quantity in equation (3-20) related to an individual ellipsoid is the mobility tensor $\hat{\mu}$. Hence in the crystallographic coordinate system the partial conductivities are obtained when only the mobility tensors are transformed into this system. Let $\hat{R}_k$ be a rotation matrix relating the k^{th} ellipsoidal principal axis system to the crystallographic axes; then the total conductivity takes the form

$$\hat{\sigma}^{t}(B) = e\, n_e \sum_{k} (\hat{R}_k^{-1}\, \hat{\mu}^{-1}\, \hat{R}_k - \hat{B})^{-1} + e\, n_h\, (\hat{\nu}^{-1} + \hat{B})^{-1} \qquad (3\text{-}23)$$

The matrix R_k for each ellipsoid must now be determined in the context of the known Fermi surface topology.

For the valence band this is trivial because the axis of revolution of the hole mobility ellipsoid coincides with the crystallographic z-axis. R_k is a unit matrix and the mobility tensor is

$$\hat{\nu} = \begin{bmatrix} \nu_1 & 0 & 0 \\ 0 & \nu_1 & 0 \\ 0 & 0 & \nu_3 \end{bmatrix} \tag{3-24}$$

A transformation

$$\hat{R}(\theta) = \begin{bmatrix} 1 & 0 & 0 \\ 0 & \cos\theta & \sin\theta \\ 0 & -\sin\theta & \cos\theta \end{bmatrix} \tag{3-25}$$

around the two fold axis (x-axis) provides the mobilities of one of the electron ellipsoids in the crystallographic coordinate system:

$$\hat{\mu}^I = \hat{R}_1^{-1}(\theta)\ \hat{\mu}\ \hat{R}_1(\theta)$$

$$= \begin{bmatrix} \mu_1 & 0 & 0 \\ 0 & \mu_2 & \mu_4 \\ 0 & \mu_4 & \mu_3 \end{bmatrix} \tag{3-26}$$

The components in (3-26) are related to the mobility components in the principle axis system of equation (3-8) by

$$\mu_1 = \mu_1^*$$

$$\mu_2 = \mu_2^* \cos^2\theta + \mu_3^* \sin^2\theta$$

$$\mu_3 = \mu_2^* \sin^2\theta + \mu_3^* \cos^2\theta \qquad (3\text{-}27)$$

$$\mu_4 = (\mu_2^* - \mu_3^*) \cos\theta \sin\theta$$

or $$\mu_4 = \tfrac{1}{2}(\mu_2 - \mu_3) \tan 2\theta$$

The angle of tilt in terms of the mobilities in crystallographic coordinate system is

$$\theta = \tfrac{1}{2} \tan^{-1} \frac{2\mu_4}{\mu_2 - \mu_3} \qquad (3\text{-}28)$$

Once the position of the first ellipsoid has been fixed with respect to the crystallographic axes, the mobility tensors for the other two electron ellipsoids can be expressed in the same reference system by applying a further transformation around the trigonal axis; the transformation matrix

$$\hat{R}\left(\pm\frac{2\pi}{3}\right) = \begin{bmatrix} -\frac{1}{2} & \mp\frac{\sqrt{3}}{2} & 0 \\ \pm\frac{\sqrt{3}}{2} & -\frac{1}{2} & 0 \\ 0 & 0 & 1 \end{bmatrix} \qquad (3\text{-}29)$$

brings the other two into the position of first one and yields the mobility tensors.

$$\hat{\mu}^{II,III} = R^{-1}\left(\pm\frac{2\pi}{3}\right) \hat{\mu}^{I} \; R\left(\pm\frac{2\pi}{3}\right) \qquad (3\text{-}30)$$

$$= \begin{bmatrix} \frac{1}{4}(\mu_1 + 3\mu_2) & \pm\frac{\sqrt{3}}{4}(\mu_1 - \mu_2) & \pm\frac{\sqrt{3}}{2}\mu_4 \\ \pm\frac{\sqrt{3}}{4}(\mu_1 - \mu_2) & \frac{1}{4}(3\mu_1 + \mu_2) & -\frac{1}{2}\mu_4 \\ \pm\frac{\sqrt{3}}{2}\mu_4 & -\frac{1}{2}\mu_4 & \mu_3 \end{bmatrix}$$

By substituting equations (3-26), (3-29) and (3-30) into (3-23), the total conductivity tensor is obtained. The total conductivity expression is rather cumbersome, so the partial conductivity contributions for the electron ellipsoids are reproduced here from Aubrey (1971).

$$\sigma_{11}^{I} = (\mu_1 + d\,B_1^2)\cdot g^{I}$$

$$\sigma_{22}^{I} = (\mu_2 + d\,B_2^2)\cdot g^{I}$$

$$\sigma_{33}^{I} = (\mu_3 + d\,B_3^2)\cdot g^{I}$$

$$\sigma_{12}^{I} = \left[+\mu_1(\mu_4 B_2 - \mu_2 B_3) + d\,B_1 B_2\right]\cdot g^{I} \qquad (3\text{-}31)$$

$$\sigma_{23}^{I} = \left[\mu_4 - \frac{d}{\mu_1}B_1 + d\,B_2 B_3\right]\cdot g^{I}$$

$$\sigma_{31}^{I} = \left[-\mu_1(\mu_3 B_2 - \mu_4 B_3) + d\,B_3 B_1\right]\cdot g^{I}$$

$$g^{I} = ne\left[1 + \frac{d}{\mu_1}B_1^2 + \mu_1(\mu_3 B_2^2 - 2\mu_4 B_2 B_3 + \mu_2 B_3^2)\right]^{-1}$$

and

$$\sigma_{11}^{II,III} = \tfrac{1}{4}(\mu_1 + 3\mu_2 + 4d\,B_1^2)\,g^{II,III}$$

$$\sigma_{22}^{II,III} = \tfrac{1}{4}(3\mu_1 + \mu_2 + 4d\,B_2^2)\,g^{II,III} \qquad (3\text{-}32)$$

$$\sigma_{33}^{II,III} = (\mu_3 + d\,B_3^2)\,g^{II,III}$$

$$\sigma_{12}^{II,III} = \left[\pm\frac{\sqrt{3}}{4}(\mu_1-\mu_2) + \mu_1\mu_4(\pm\frac{\sqrt{3}}{2}B_1 - \tfrac{1}{2}B_2) - \mu_1\mu_2 B_3 + d\,B_1 B_2\right]g^{II,III}$$

$$\sigma_{23}^{II,III} = \left[-\tfrac{1}{2}\mu_4 - \tfrac{1}{4}(3\mu_1\mu_3 + \frac{d}{\mu_1})B_1 \pm \frac{\sqrt{3}}{4}(\mu_1\mu_3 - \frac{d}{\mu_1})B_2 \pm \frac{\sqrt{3}}{2}\mu_1\mu_4 B_3 + d\,B_2 B_3\right]g^{II,III}$$

$$\sigma_{31}^{II,III} = \left[\pm\frac{\sqrt{3}}{2}\mu_4 \pm (\mu_1\mu_3 - \frac{d}{\mu_1})B_1 - \tfrac{1}{4}(\mu_1\mu_3 + \frac{3d}{\mu_1})B_2 - \tfrac{1}{2}\mu_1\mu_4 B_3 + d\,B_1 B_3\right]g^{II,III}$$

$$g^{II,III} = ne\left[1 + \tfrac{1}{4}(3\mu_1\mu_3 + \frac{d}{\mu_1})B_1^2 + \tfrac{1}{4}(\mu_1\mu_3 + \frac{3d}{\mu_1})B_2^2 + \mu_1\mu_2 B_3^2 \mp \frac{\sqrt{3}}{2}(\mu_1\mu_3 - \frac{d}{\mu_1})B_1 B_2 + \mu_1\mu_4 B_2 B_3 \mp \sqrt{3}\mu_1\mu_4 B_3 B_1\right]^{-1}$$

Here d represents the determinant of equation (3-26) and the remaining components can be found from the Onsager relation $\sigma_{ij}(\bar{B}) = \sigma_{ji}(-\bar{B})$. The partial hole contribution is readily obtained from equation (3-31) by replacing $\bar{B}$ by $-\bar{B}$ and using the mobility components $\nu_1 = \nu_2$, ν_3, $\nu_4 = 0$ instead of the corresponding electron parameters.

The conductivity expressions in equation (3-31) and (3-32) relate to the classical range of magnetic fields, quantum effects arising at higher fields have not been taken into account.

IV THE THERMOMAGNETIC POWER TENSOR

To obtain the thermomagnetic power tensor in a useful form, it is convenient to write partial electron P_e and hole P_h thermoelectric powers as

$$P_e = \frac{k}{e}\left[\frac{5F_{3/2}(\eta_e)}{3F_{\frac{1}{2}}(\eta_e)} - \eta_e\right] \qquad (3\text{-}33)$$

and

$$P_h = -\frac{k}{e}\left[\frac{5F_{3/2}(\eta_n)}{3F_{\frac{1}{2}}(\eta_h)} - \eta_h\right]$$

Then the current density (3-22) is

$$\bar{J} = \hat{\sigma}^t(\bar{B})\,\bar{E}^* + (P_e\,\hat{\sigma}^e(\bar{B}) + P_h\,\hat{\sigma}^h(\bar{B}))\,\bar{\nabla}_r T \qquad (3\text{-}34)$$

where $\hat{\sigma}^t(\bar{B})$, $\hat{\sigma}^e(\bar{B})$ and $\hat{\sigma}^h(\bar{B})$ represent the total and partial electron and hole conductivities respectively. Here the physical conditions imply the control of $\bar{E}^*$ and $\bar{\nabla}_r T$ as independent variables, a situation not readily attained in the laboratory: the practical

experimental arrangement for measuring isothermal coefficients requires control of the current density $\bar{J}$ and the temperature gradient $\bar{\nabla}_r T$. The desired form can be found by multiplying equation (3-34) by $\hat{\sigma}^t(\bar{B})^{-1}$ (or $\hat{\rho}(\bar{B})$), when

$$\bar{E}^* = \hat{\rho}^t(\bar{B})\ \bar{J} - \hat{\rho}^t(\bar{B})\ [P_e \hat{\sigma}^e(\bar{B}) + P_h \hat{\sigma}^h(\bar{B})]\ \bar{\nabla}_r T] \qquad (3\text{-}35)$$

and then setting the external current $\bar{J}$ equal to zero.

$$\bar{E} = - \hat{\rho}^t(\bar{B})\ [P_e \hat{\sigma}^e(\bar{B}) + P_h \hat{\sigma}^h(\bar{B})]\ \bar{\nabla}_r T] \qquad (3\text{-}36)$$

This equation defines the thermomagnetic power tensor $\hat{\alpha}(\bar{B})$ by

$$\hat{\alpha}(\bar{B}) = - \hat{\rho}^t(\bar{B})\ [P_e \hat{\sigma}^e(\bar{B}) + P_h \hat{\sigma}^h(\bar{B})] \qquad (3\text{-}37)$$

or in component form

$$\alpha_{ij}(\bar{B}) = - \rho^t_{ik}(\bar{B})\ [P_e \sigma^e_{kj}(\bar{B}) + P_h \sigma^h_{kj}(\bar{B})] \qquad (3\text{-}37a)$$

When the magnetic field is zero, this expression reduces to the standard form for the thermoelectric power of a two-band conductor

$$\hat{\alpha} = \frac{P_e \hat{\sigma}^e + P_h \hat{\sigma}^h}{\hat{\sigma}^e + \hat{\sigma}^h} \qquad (3\text{-}37b)$$

V THE LOW FIELD MAGNETORESISTIVITY EXPRESSIONS FOR BISMUTH

Much of the work presented in this thesis concerns measurements and analysis of the low field magnetoresistivity tensor and we now turn to obtain quantitative expressions for this particular case.

Although these expressions have been obtained elsewhere (Zitter 1962), they have not been reached as the limiting case of the general forms presented in the foregoing sections of this chapter. For completion, this procedure will now be carried through. But before this can be done, it is necessary to develop the low field tensor components by the phenomenological scheme used by Fumi (1952).

A - PHENOMENOLOGICAL DERIVATION OF THE LOW FIELD TENSOR COMPONENTS

The phenomenological theory of low field galvanomagnetic effects as described by Okada (1955) and Juretsckhe (1955) assumes Ohm's law to hold for the conductivity tensor $\hat{\sigma}(\bar{B})$ or its reciprocal the resistivity tensor $\hat{\rho}(\bar{B})$ in the presence of a magnetic field. In an anisotropic media, these relations can be written

$$J_i = \sigma_{ij}(\bar{B})\ E_j \qquad (i=1, 2,3) \tag{3-38}$$

or

$$E_i = \rho_{ij}(\bar{B})\ J_j \tag{3-39}$$

where summation is implied on repeated indices and E_i and J_i are the components of the electric field and current density in Cartesian coordinates, The effect of magnetic field is included in equations (3-38) and (3-39) by making the conductivity and resistivity tensors general functions of magnetic field.

Assuming that $\hat{\sigma}(\bar{B})$ and $\hat{\rho}(\bar{B})$ will converge for small values of $\bar{B}$, that is that $\hat{\mu}.\bar{B}$ is much less then unity, a series expansion in powers of the magnetic field components is possible.

$$\sigma_{ij}(\bar{B}) = \sigma_{ij}^{(o)} - \sigma_{ij,k_1}^{(1)} B_{k_1} - \sigma_{ij,k_1k_2}^{(2)} B_{k_1} B_{k_2} - \ldots. \quad (3\text{-}40)$$

$$\rho_{ij}(\bar{B}) = \rho_{ij}^{(o)} + \rho_{ij,k_1}^{(1)} B_{k_1} + \rho_{ij,k_1k_2}^{(2)} B_{k_1} B_{k_2} + \ldots \quad (3\text{-}41)$$

This amounts to a Taylor series expansion with the coefficients in the general form

$$\rho_{ij,k_1k_2\ldots k_N}^{(N)} = \frac{1}{N!} \left[\frac{\partial^N \rho_{ij}(\bar{B})}{\partial B_{k_1} \ldots \partial B_{k_N}} \right]_{\bar{B}=0} \quad N = 0,1,2 \ldots \quad (3\text{-}42)$$

The coefficients separate into various groups, each connecting the same power of magnetic field. Experimental studies normally determine the tensor coefficients $\rho_{ij,k_1k_2\ldots k_N}^{N}$ up to N=2. For greater values of N, the number of terms involved makes the task prohibitively difficult. The terms ρ_{ij}^{o}, $\rho_{ij,k_1}^{(1)}$ and $\rho_{ij,k_1k_2}^{(2)}$ containing up to N=2 are often referred to as electrical, Hall and magneto-resistivity tensors. Hence the low field galvanomagnetic effects in bismuth up to the B^2 terms in magnetic field can be detailed through the determination of the components of these tensors. This is achieved by the restrictions imposed from the Onsager reciprocity relation and also the invariance of the tensor components under the point group symmetry operations of the crystal (Juretschke 1955).

The point group $\bar{3}m$ (D_{3d}), isomorphic to bismuth, exhibits a centre of inversion and as a result only even rank polar and odd rank axial tensors do not vanish automatically. This, together with the

application of the Onsager relation, $\rho_{ij}(\bar{B}) = \rho_{ji}(-\bar{B})$, on the resistivity $\hat{\rho}(\bar{B})$ leads to the following types of tensors with the symmetry specifications shown:

$$\rho^{(0)}_{ij} = \rho^{(0)}_{ji} \quad \text{(second rank symmetric polar tensor)}$$

$$\rho^{(1)}_{ij,k_1} = -\rho^{(1)}_{ji,k_1} \quad \text{(Third rank axial tensor)} \tag{3-43}$$

$$\rho^{(2)}_{ij,k_1k_2} = \rho^{(2)}_{ji,\text{(all permutations of k)}} \quad \text{(Fourth rank symmetric polar tensor)}$$

If the symmetric and antisymmetric parts are defined as

$$S_{ij} = \rho^{(0)}_{ij} + \rho^{(2)}_{ij,k_1k_2} B_{k_1} B_{k_2} \tag{3-44}$$

and $\alpha_{ij} = \rho^{(1)}_{ij,k_1} B_{k_1}$

equation (3-39) can be written as

$$E_i = S_{ij} J_j + \alpha_{ij} J_j \tag{3-45}$$

which simply means that the resistivity tensor can be written as the sum of a symmetric and an antisymmetric tensors. Equation (3-45) may further be expressed in terms of an axial vector $\bar{\alpha}$

$$E_i = S_{ij} J_j + (\bar{J} \wedge \bar{\alpha})_i \tag{3-46}$$

showing that the Joule heat $\bar{E} \cdot \bar{J}$ is determined only by the symmetric

part of the resistivity tensor, and also that a magnetic field perpendicular to the current direction gives rise to an electric field in a direction perpendicular to itself and to the current. This phenomenon, known as the Hall effect, is due to the antisymmetric part of the resistivity tensor and is given here as the product of the tensor $\rho^{(1)}_{ij,k_1}$ and the first order term in B_{k_1}. The tensor $\rho^{(1)}_{ij,k_1}$ is called the Hall tensor, which is equivalent to a second rank antisymmetric tensor and an axial vector, that is, it is the same as the product of two axial vectors. The magnetoresistivity tensor $\rho^{(2)}_{ij,k_1k_2}$ relates a symmetric tensor of second rank S_{ij} (equation (3-44)) with vector products like $B_{k_1} B_{k_2}$; it is symmetric with respect to the interchange of suffixes i and j and k_1 and k_2 and may be regarded as relating two symmetric tensors each of rank two.

The non-zero components for the tensors appearing in (3-43) can be obtained by group character analysis. The number of independent components are given by, the number of times the total symmetric representation occurs in the tensor representation $\psi_\rho(R)$ of the group (Bhagavantam 1966). This is carried through by the formula

$$n_i = \frac{1}{g} \sum_\rho h_\rho \; \psi_\rho(R) \; \psi_i(R) \qquad (3\text{-}47)$$

where g is the order of the group, h_ρ is the order of the ρ^{th} class in the group, $\psi_i(R)$ (in this case) is the character of the total symmetric irreducible representations. The number of independent components for a tensor representation of a group is invarient

with respect to the choice of reference frames. So, without loss of generality, one can choose Cartesian orthogonal frames. The number of non-zero components is dictated by this choice.

The Cartesian orthogonal frames employed here are $z//C_3$ and $x//C_2^1$ with respect to the crystallographic axes.

The similarity in transformation properties of the tensor components and the coordinate products in Cartesian orthogonal frames, allows the replacement of the tensor components by coordinate products of corresponding order and intrinsic symmetry (Juretschke 1952). Since even coordinate products are even under the inversion and odd ones are odd, the computations can be carried out with completeness in the subgroup 3m (or D_3) of the group $\bar{3}m = 3m \times i$ (or $D_{3d} = D_3 \times i$).

The characters $\psi_\rho(R)$ appropriate to the various tensor representations in equation (3-43) of the group can be obtained as the character products of simpler representations (Bhagavantam 1966). The group 3m contains only proper rotations and the corresponding character expression for the electrical resistivity tensor is

$$\psi_\rho(R(\phi)) = 4\cos^2\phi + 2\cos\phi \qquad (3\text{-}48a)$$

for the Hall resistivity tensor

$$\psi_\rho(R(\phi)) = 4\cos^2\phi + 2\cos\phi + 1 \qquad (3\text{-}48b)$$

and for the magnetoresistivity tensor

$$\psi_\rho(R(\phi)) = 16\cos^4\phi + 16\cos^3\phi + 4\cos^2\phi \qquad (3\text{-}48c)$$

The characters appropriate to the rotation classes E, C_3, C_2^1 of the group 3m, evaluated for each tensor representation are presented in table (3-1) together with the number of independent components.

Taking the magnetoresistivity tensor $\rho^{(2)}_{ij,k_1k_2}$ as an example, we now evaluate the characters for the rotation classes and the number of independent tensor components.

E represents the identity operation: $\cos \phi = 1$

C_3 represents rotation by $\pm \frac{2\pi}{3}$: $\cos \phi = -\frac{1}{2}$

C_2^1 represents rotation by π : $\cos \phi = -1$

When these results are used with the general character expression (3-48c), the characters $\psi\rho(R)$ for the rotation classes can be obtained as

$$\psi\rho\ (E) = 16 + 16 + 4 = 36$$

$$\psi\rho\ (C_3) = 16\ (-\tfrac{1}{4})^4 + 16\ (-\tfrac{1}{2})^3 + 4\ (-\tfrac{1}{2})^2 = 0$$

$$\psi\rho\ (C_2^1) = 16 - 16 + 4 = 4$$

The total symmetric irreducible representations $\psi_i(R)$ equal unity for all classes; we can now substitute for $\psi\rho\,(E)$, $\psi\rho(C_3)$ and $\psi\rho\,(C_2^1)$ in

$$n_i = \frac{1}{g} \sum_{\rho} h\rho\ \ \psi\rho\,(R)\ \psi_i(R)$$

where $g = 6$, $h\rho$ is 1, 2, 3 for E, C_3 and C_2^1 respectively. The number of independent components obtained is

$$n_1 = \frac{1}{6}(1.(36) + 2.(0) + 3.(4)) = 8$$

TABLE (3-1)

TENSOR REPRESENTATIONS	CLASSES E	$2C_3$	$3C_2^1$	NO. OF INDEPENDENT COMPONENTS
$\rho^{(0)}_{ij}$	6	0	2	2
$\rho^{(1)}_{ij,k_1}$	9	0	1	2
$\rho^{(2)}_{ij,k_1k_2}$	36	0	4	8

Once the number of independent components appropriate to each tensor has been fixed, the non-zero components can be obtained by demanding the invariance of the tensor components under the point group symmetry operations. This procedure needs to be carried out for all the operations of the group, until the number of independent components reduces to those numbers specified in table(3-1).

The procedure is straightforward; denoting the Cartesian orthogonal components of the tensors with the coordinate products that are their indices, for the symmetric second rank tensor $\rho^{(0)}_{ij}$ we have

$$[\rho_{ij}] = \begin{bmatrix} xx & xy & xz \\ xy & yy & yz \\ xz & yz & zz \end{bmatrix}$$

Now the transformation of the coordinates for the symmetry operations are; for C_2^1: $x \rightarrow x$, $y \rightarrow -y$, $z \rightarrow -z$

and for C_3: $x \rightarrow -\frac{1}{2}x + \frac{\sqrt{3}}{2}y$, $y \rightarrow -\frac{\sqrt{3}}{2}x - \frac{1}{2}y$, $z \rightarrow z$

For C_2^1 we can see that the odd product terms of y and z are not invariant because they reverse in sign yielding $xy = xz = 0$. Keeping in mind that the xy and xz components are zero we have for application of C_3:

$$xx \rightarrow \frac{1}{4}x^2 + \frac{3}{4}y^2 + 0$$

$$yy \rightarrow \frac{3}{4}x^2 + \frac{1}{4}y^2 + 0$$

$$zz \rightarrow zz$$

and $yz = 0$. Since the number of independent components is known to be two, xx must equal yy. Therefore, we have for the coefficient scheme

$$[\overset{(o)}{\rho}_{ij}] = \begin{bmatrix} \rho_{11} & 0 & 0 \\ 0 & \rho_{11} & 0 \\ 0 & 0 & \rho_{33} \end{bmatrix} \qquad (3\text{-}49)$$

Similarly for the tensor $\rho^{(1)}_{ij,k_1}$ by adopting the order of indices for i as (x, y, z) and for j,k_1 as (xx, yx, zx, xy, yy, zy, xz, yz, zz), the following coefficient scheme is obtained:

$$[\rho^{(1)}_{ij,k_1}] = \begin{bmatrix} 0 & 0 & 0 & 0 & 0 & \rho 23,1 & 0 & \rho 12,3 & 0 \\ 0 & 0 & -\rho 23,1 & 0 & 0 & 0 & -\rho 12,3 & 0 & 0 \\ 0 & \rho 23,1 & 0 & -\rho 23,1 & 0 & 0 & 0 & 0 & 0 \end{bmatrix} \tag{3-50}$$

and for $\rho^{(2)}_{ij,k_1k_2}$ the adoption of coordinate replacement for ij and k_1k_2 is (xx, yy, zz, yz = zy, xz = zx, xy = yx):

$$[\rho^{(2)}_{ij,k_1k_2}] = \begin{bmatrix} \rho_{11\ 11} & \rho_{11\ 22} & \rho_{11\ 33} & 2\rho_{11\ 23} & 0 & 0 \\ \rho_{11,22} & \rho_{11,11} & \rho_{11\ 33} & -2\rho_{11\ 23} & 0 & 0 \\ \rho_{33,11} & \rho_{33,11} & \rho_{33,33} & 0 & 0 & 0 \\ \rho_{23,11} & -\rho_{23,11} & 0 & 2\rho_{23,23} & 0 & 0 \\ 0 & 0 & 0 & 0 & 2\rho_{23,23} & \rho_{23\ 11} \\ 0 & 0 & 0 & 0 & 2\rho_{11,23} & (\rho_{11,11}-\rho_{11,23}) \end{bmatrix} \tag{3-51}$$

the tensor expressions (3-49), (3-50) and (3-51) can be arranged in

a form suitable to give the total resistivity component $\rho_{ij}(\bar{B})$ in a peculiar matrix sum given by Hartman (1969)

$$\hat{\rho}(\bar{B}) = \begin{bmatrix} \rho_{11} & 0 & 0 \\ 0 & \rho_{11} & 0 \\ 0 & 0 & \rho_{33} \end{bmatrix} + \begin{bmatrix} 0 & \rho_{12,3}B_3 & -\rho_{23,1}B_2 \\ -\rho_{12,3}B_3 & 0 & \rho_{23,1}B_1 \\ \rho_{23,1}B_2 & -\rho_{23,1}B_1 & 0 \end{bmatrix}$$

$$+ \begin{bmatrix} A_{11} & A_{12} & A_{13} & A_{14} & 0 & 0 \\ A_{12} & A_{11} & A_{13} & -A_{14} & 0 & 0 \\ A_{31} & A_{31} & A_{33} & 0 & 0 & 0 \\ A_{41} & -A_{41} & 0 & A_{44} & 0 & 0 \\ 0 & 0 & 0 & 0 & A_{44} & A_{41} \\ 0 & 0 & 0 & 0 & A_{14} & \frac{1}{2}(A_{11}-A_{12}) \end{bmatrix} \begin{bmatrix} B_1^2 \\ B_2^2 \\ B_3^2 \\ 2B_2B_3 \\ 2B_3B1 \\ 2B_1B_2 \end{bmatrix} \qquad (3\text{-}52)$$

Here A_{pq} (p,q = 1, 6) is introduced for $\rho^{(2)}_{ij,k_1k_2}$. p and q each replace the pair of indices ij and k_1k_2 respectively, the following correspondence obtains: 11 = 1, 22 = 2, 33 = 3, 23 = 4, 13 = 31 = 5, 12 = 21 = 6. The factors 2 in $\rho^{(2)}_{ij,k_1k_2}$ have been carried into the magnetic field components. For the first two tensors in equation

(3-52) the matrix sum is applicable, while the last term gives the magnetoresistivity contributions to the $\rho_{ij}(\bar{B})$ components in the following order $\rho_{11}(\bar{B})$, $\rho_{22}(\bar{B})$, $\rho_{33}(\bar{B})$, $\rho_{23}(\bar{B})$, $\rho_{13}(\bar{B})$ and $\rho_{12}(\bar{B})$.

Except for the sign difference in the expansions (3-40) and (3-41), there is a complete correspondence between the conductivity and resitivity tensors and both must exhibit exactly the same symmetry. Therefore, for the conductivity tensor we have

$$\sigma(\bar{B}) = \begin{bmatrix} \sigma_{11} & 0 & 0 \\ 0 & \sigma_{11} & 0 \\ 0 & 0 & \sigma_{33} \end{bmatrix} - \begin{bmatrix} 0 & \sigma_{12,3}B_3 & -\sigma_{23,1}B_2 \\ -\sigma_{12,3}B_3 & 0 & \sigma_{23,1}B_1 \\ \sigma_{23,1}B_2 & -\sigma_{23,1}B_1 & 0 \end{bmatrix}$$

$$- \begin{bmatrix} S_{11} & S_{12} & S_{13} & S_{14} & 0 & 0 \\ S_{12} & S_{11} & S_{13} & -S_{14} & 0 & 0 \\ S_{31} & S_{31} & S_{33} & 0 & 0 & 0 \\ S_{41} & -S_{41} & 0 & S_{44} & 0 & 0 \\ 0 & 0 & 0 & 0 & S_{44} & S_{41} \\ 0 & 0 & 0 & 0 & S_{14} & \tfrac{1}{2}(S_{11}-S_{12}) \end{bmatrix} \begin{bmatrix} B_1^2 \\ B_2^2 \\ B_3^2 \\ 2B_2B_3 \\ 2B_3B_1 \\ 2B_1B_2 \end{bmatrix} \qquad (3\text{-}53)$$

B - GENERAL RELATIONS BETWEEN THE FIELDS AND THE CURRENT

Although the coefficient scheme obtained in the previous section contains all the required information, it is convenient for experimental purposes to have explicit expressions for the field and current directions. The coefficient tensors $\rho_{ij}(B)$ from equation (3-52) can be obtained in terms of $\rho^{(o)}_{ij}$, $\rho^{(1)}_{ij,k_1}$ and A_{pq} as

$$
\begin{aligned}
\rho_{11}(B) &= \rho_{11} + A_{11}B_1^2 + A_{12}B_2^2 + A_{13}B_3^2 + 2A_{14}B_2B_3 \\
\rho_{12}(B) &= \rho_{12,3}B_3 + 2A_{14}B_1B_3 + (A_{11} - A_{12})\,B_1B_2 \\
\rho_{13}(B) &= -\rho_{23,1}B_2 + 2A_{44}B_1B_3 + 2A_{41}B_1B_2 \\
\rho_{22}(B) &= \rho_{11} + A_{12}B_1^2 + A_{11}B_2^2 + A_{13}B_3^2 - 2A_{14}B_2B_3 \\
\rho_{23}(B) &= \rho_{23,1}B_1 + A_{41}B_1^2 - A_{41}B_2^2 + 2A_{44}B_2B_3 \\
\rho_{33}(B) &= \rho_{33} + A_{31}B_1^2 + A_{31}B_2^2 + A_{33}B_3^2 \\
\rho_{21}(B) &= \rho_{12}(-B) \\
\rho_{31}(B) &= \rho_{13}(-B) \\
\rho_{32}(B) &= \rho_{23}(-B)
\end{aligned}
\qquad (3\text{-}54)
$$

When these are substituted into equation (3-39) we have for the electric field components:

$$
\begin{aligned}
E_1 &= (\rho_{11} + A_{11}B_1^2 + A_{12}B_2^2 + A_{13}B_3^2 + 2A_{14}B_2B_3)\,J_1 \\
&+ (\rho_{12,3}B_3 + 2A_{14}B_3B_1 + (A_{11} - A_{12})\,B_1B_2)\,J_2 \\
&+ (-\rho_{23,1}B_2 + 2A_{44}B_3B_1 + 2A_{41}\,B_1B_2)\,J_3
\end{aligned}
\qquad (3\text{-}55)
$$

$$E_2 = (-\rho_{12,3}B_3 + 2A_{14}B_3B_1 + (A_{11} - A_{12})B_1B_2)J_1$$
$$+ (\rho_{11} + A_{12}B_1^2 + A_{11}B_2^2 + A_{13}B_3^2 - 2A_{14}B_2B_3) J_2$$
$$+ (\rho_{23,1}B_1 + A_{41}(B_1^2 - B_2^2) + 2A_{44}B_2B_3) J_3 \qquad (3\text{-}55)$$

$$E_3 = (\rho_{23,1}B_2 + 2A_{44}B_3B_1 + 2A_{41}B_1B_2) J_1$$
$$+ (-\rho_{23,1}B_1 + A_{41}(B_1^2 - B_2^2) + 2A_{44}B_2B_3) J_2$$
$$+ (\rho_{33} + A_{31}(B_1^2 + B_2^2) + A_{33}B_3^2) J_3$$

Thus we have now obtained a basic set of equations that will specify the low field galvanomagnetic effects in bismuth (or any material of the crystallographic point group $\bar{3}m$). The scheme is quite general; $\bar{B}$ and $\bar{J}$ may be directed at any angle to the crystal axis. The long axis of the sample determines the current direction. If the samples employed are cut along a major crystallographic direction, the current density component appropriate to that direction is readily obtained from (3-55). For an arbitrary direction they are determined by resolving into J_1, J_2 and J_3 components. In principle, two samples cut one in the xy-plane and one other in the z-direction are sufficient to measure all the required tensor components of bismuth. Coefficients may be isolated, by choosing special cases of $\bar{E}$, $\bar{J}$, $\bar{B}$ orientations, and measured in turn.

In the present study the measurements were carried out on three samples cut along major crystallographic directions. This

procedure will be discussed in the experimental chapter.

C - DERIVATION OF THE TENSOR COMPONENTS FROM BAND THEORY

Abeles and Meiboom (1956) first obtained the twelve low field, conductivity tensor components for bismuth using an ellipsoidal Fermi surface model with zero tilt angle. They assume only intravalley scattering of the carriers and use the relaxation time approximation. Essentially the vector current contributions for each valley are summed in the frame of the crystal axes. By a series expansion of the current density, for low field cases ($\hat{\mu}.\overline{B} << 1$), the conductivity components are obtained in terms of the specified band parameters. Drabble and Wolf (1956) for bismuth Telluride and later Zitter (1962) for bismuth, using the results of Herring and Vogt (1956), have extended the analysis to an anisotropic relaxation-time tensor $\tau(\varepsilon)$ and have allowed tilt of the ellipsoidal Fermi surface pockets.

A somewhat different and more satisfying approach is to develop the low field limit from the general conductivity tensor $\hat{\sigma}(\overline{B})$ given in the previous section. As an example of the procedure followed, the component $\sigma_{11}(B)$ is now taken and used to obtain the low field tensor coefficients σ_{11} and S_{11} in terms of the band parameters. Thus from equation (3-53) we have for the low field case

$$\sigma_{11}(B_1) = \sigma_{11} - S_{11}B_1^2 \qquad (3\text{-}56)$$

The corresponding tensor component in terms of the band parameters

from equations (3-31) and (3-32) is

$$\sigma_{11}(B_1) = Ne \frac{2(\mu_1+\mu_2) + [\mu_1^2\mu_3 + 3\mu_1(\mu_2\mu_3-\mu_4^2)] B_1^2}{4 + [3\mu_1\mu_3 + (\mu_2\mu_3 - \mu_4^2)] B_1^2} + Pe\nu_1 \qquad (3\text{-}57)$$

Putting $B_1 = 0$, we get $\sigma_{11}(0) = \sigma_{11}^{(1)}$,

$$\sigma_{11}^{(1)} = \tfrac{1}{2}Ne(\mu_1 + \mu_2) + Pe\nu_1 \qquad (3\text{-}58)$$

Solving S_{11} from equation (3-56), we obtain

$$S_{11} = -(\sigma_{11}(B_1) - \sigma_{11}^{(1)}) / B_1^2$$

and constructing $-(\sigma_{11}(B_1) - \sigma_{11}^{(1)}) / B_1^2$ from equations (3-57) and (3-58)

$$S_{11} = -(\sigma_{11}(B_1) - \sigma_{11}^{(1)}) / B_1^2$$

$$= \frac{Ne}{2} \frac{(\mu_1-\mu_2)^2\mu_3 + (5\mu_1-\mu_2)\mu_4^2}{4 + 3\mu_1\mu_3 + (\mu_2\mu_3-\mu_4^2) B_1^2}$$

As $B_1 \longrightarrow 0$, S_{11} becomes

$$S_{11} = \frac{Ne}{8}[(\mu_1-\mu_2)^2\mu_3 + (5\mu_1-\mu_2)\mu_4^2]$$

Similarly the rest of the conductivity tensor components can be obtained as

$$\sigma_{11} = (\tfrac{1}{2}Ne)\,(\mu_1 + \mu_2) + Pe\ \nu_1\ ,\quad \sigma^{o}_{33} = Ne\mu_3 + Pe\ \nu_3$$

$$\sigma_{12,3} = Ne\ \mu_1\mu_2 - Pe\ \nu_1^{\,2}\ ,\quad \sigma_{23,1} = (\tfrac{1}{2}Ne)\,[(\mu_1+\mu_2)\mu_3 - \mu_4^{\,2}] - Pe\ \nu_1\ \nu_3$$

$$S_{11} = (\tfrac{1}{8}Ne)\,[(\mu_1-\mu_2)^2\mu_3 + (5\mu_1-\mu_2)\mu_4^{\,2}]$$

$$S_{12} = (\tfrac{1}{8}Ne)\,[(3\mu_1^{\,2} + 3\mu_2^{\,2} + 2\mu_1\mu_2)\mu_3 - (\mu_1+3\mu_2)\mu_4^{\,2}] + Pe\ \nu_1^{\,2}\ \nu_3$$

$$S_{13} = (\tfrac{1}{2}Ne)\,[\mu_1\mu_2(\mu_1 + \mu_2)] + Pe\ \nu_1^{\,3}$$

$$S_{31} = (\tfrac{1}{2}Ne)\,[(\mu_1 + \mu_2)\mu_3^{\,2} - \mu_3\mu_4^{\,2}] + Pe\ \nu_1\ \nu_3^{\,2} \qquad (3\text{-}59)$$

$$S_{33} = Ne\mu_1\mu_4^{\,2}$$

$$S_{14} = (\tfrac{1}{4}Ne)\ \mu_1\mu_4(\mu_1 - \mu_2)$$

$$S_{41} = -(\tfrac{1}{4}Ne)\ \mu_4\,[\mu_3(\mu_1-\mu_2) + \mu_4^{\,2}]$$

$$S_{44} = -[\,(\tfrac{1}{4}Ne)\ \mu_1\mu_2\mu_3 + (\tfrac{1}{2}Pe)\ \nu_1^{\,2}\ \nu_3]$$

These are the same expressions as those given by Zitter (1962) and Hartman (1969).

The resistivity tensor components are related to the conductivity through the relation $\sigma_{ij}(\bar{B})\ \rho_{jk} = \delta_{ik}$. The relationships between the components are given by Juretschke (1955) as

$$\sigma_{11} = (\rho_{11})^{-1},$$

$$\sigma_{33} \doteq (\rho_{33})^{-1},$$

$$\sigma_{12,3} \doteq \rho_{12,3}(\rho_{11})^{-2},$$

$$\sigma_{23,1} = \rho_{23,1}(\rho_{11}\rho_{33})^{-1},$$

$$S_{11} = A_{11}(\rho_{11})^{-2},$$

$$S_{12} = (\rho_{11})^{-2}[A_{12} \doteq (\rho^2_{23,1}/\rho_{33})], \tag{3-60}$$

$$S_{13} = (\rho_{11})^{-2}[A_{13} + (\rho^2_{12,3}/\rho_{11})],$$

$$S_{31} = (\rho_{33})^{-2}[A_{31} + (\rho^2_{23,1}/\rho_{11})],$$

$$S_{33} = A_{33}(\rho_{33})^{-2},$$

$$S_{14} = A_{14}(\rho_{11})^{-2},$$

$$S_{41} = A_{41}(\rho_{11}\rho_{33})^{-1},$$

$$S_{44} = (\rho_{11}\rho_{33})^{-1}[A_{44} - (\rho_{12,3}\rho_{23,1}/2\rho_{11})].$$

Hence the resistivity tensor components in terms of the band parameters are (here C = P/N)

$$\rho_{11} = (2/Ne)(\mu_1+\mu_2+2C\nu_1)^{-1}, \quad \rho_{33} = (1/Ne)(\mu_3+C\nu_3)^{-1}$$

$$\rho_{12,3} = \frac{4}{Ne}(\mu_1\mu_2-c\nu_1^2)(\mu_1+\mu_2+2c\nu_1)^{-2},$$

$$\rho_{23,1} = \frac{1}{Ne}[\mu_3(\mu_1+\mu_2)-2c\nu_1\nu_3-\mu_4^2](\mu_1+\mu_2+2c\nu_1)^{-1}(\mu_3+c\nu_3)^{-1},$$

$$A_{11} = \frac{1}{2Ne}[\mu_3(\mu_1-\mu_2)^2+\mu_4^2(5\mu_1-\mu_2)](\mu_1+\mu_2+2c\nu_1)-2,$$

$$A_{12} = \frac{1}{2Ne}\{\mu_1(3\mu_1\mu_3+\mu_4^2)+2\mu_1+3\mu_2)(\mu_2\mu_3-\mu_4^2)+8c\nu_1^2\nu_3$$

$$- 2[(\mu_1+\mu_2)\mu_3-2c\nu_1\nu_3-\mu_4^2]^2(\mu_3+c\nu_3)^{-1}\}(\mu_1+\mu_2+2c\nu_1)^{-2}$$

$$A_{13} = \frac{2}{Ne}[\mu_1\mu_2(\mu_1+\mu_2)+2c\nu_1^3-4(\mu_1\mu_2-c\nu_1^2)^2(\mu_1+\mu_2+2c\nu_1)^{-1}]$$

$$(\mu_1+\mu_2+2c\nu_1)^{-2} \qquad (3\text{-}61)$$

$$A_{31} = \frac{1}{2Ne}[2c\nu_1(\mu_1+\mu_2)(\mu_3+\nu_3)^2+\mu_4^2[\mu_3(\mu_1+\mu_2)-\mu_4^2-$$

$$2c\nu_1(\mu_3+2\nu_3)] \quad (\mu_1+\mu_2+2c\nu_1)^{-1}(\mu_3+c\nu_3)^{-2}$$

$$A_{33} = \frac{1}{Ne}(\mu_1\mu_4^2)(\mu_3+c\nu_3)^{-2}$$

$$A_{14} = \frac{1}{Ne}\mu_4[\mu_1(\mu_1-\mu_2)](\mu_1+\mu_2+2c\nu_1)^{-2}$$

$$A_{41} = -\frac{1}{Ne}\mu_4[\mu_3(\mu_1-\mu_2) + \mu_4^2]\ (\mu_1+\mu_2+2c\nu_1)^{-1}(\mu_3+c\nu_3)$$

$$A_{44} = -\frac{1}{Ne}\{\mu_1\mu_2[\mu_4^2+2c\nu_1(\mu_3+\nu_3)] + c\nu_1^2[(\mu_1+\mu_2)(\mu_3+\nu_3) - \mu_4^2]\}\cdot$$
$$(\mu_1+\mu_2+2c\nu_1)^{-2}(\mu_3+c\nu_3)^{-1}$$

VI - THE LOW FIELD THERMOMAGNETIC EFFECTS

In general, systematic measurements and analysis of thermomagnetic effects proves to be more difficult than for galvanomagnetic effetcs. The first observation of thermomagnetic effects was actually in bismuth and dates back to 1886 (Ettingshausen and Nernst 1886). Interest in thermomagnetic effects has been stimulated both from theoretical considerations and by possible practical applications in energy conversion devices. At present the developments do not quite justify the hopes that have been raised for device applications nor have the experimental and theoretical analyses been as successful as in the galvanomagnetic effects. The success in measurement and the interpretation of precise galvanomagnetic data has extensively contributed to our knowledge of the band structure and the mechanisms governing the interaction between the carriers and lattice vibrations or defects. The difficulties associated with thermomagnetic effects are mainly of a theoretical nature. As is well known, the thermomagnetic effects can be attributed to the carrier diffusion together with in some cases phonon drag effects. The relative contributions of these two effects are determined by the electron mobilities and the lattice thermal conductivities in any particular material. Even

for structures with the highest symmetry, it has proved difficult to separate these two contributions quantitatively: it is usual to treat each separately. The contributions to the thermomagnetic effect in bismuth due to diffusion of the electronic carriers will be treated theoretically through the application of equation (3-37), for arbitrary fields, in a later chapter. Here the phenomenological low field expressions are developed in a similar manner to the galvanomagnetic case with a few minor differences. Bhagavantam (1966) lists the non-vanishing coefficient scheme for all point groups. In practice, however rather than being specified in terms of these tensor components the thermomagnetic data is defined primarily by the direction of $\overline{B}$ with respect to the temperature gradient. A definition labelled by conventional names is not suitable and causes ambiguities due to the intermixing of voltages from different order effects in magnetic field powers. It will be shown later that the phenomenological theory expressed in terms of tensor components indeed predicts the peculiar symmetries involved in the thermomagnetic effects in bismuth, including the Umkehr effect. Therefore the best procedure is to perform a straightforward determination of the thermomagnetic tensor coefficients without attaching conventional labels to one or another type of measurement. In following sections the expressions suitable for a particular experimental set up for the measurement of the thermomagnetic effects is obtained and the prediction of an Umkehr effect is briefly touched upon.

A - PHENOMENOLOGICAL DERIVATION OF TENSOR COEFFICIENTS

Starting from equation (3-36) in component form we have

$$E_i = \alpha_{ij}(\bar{B})\ G_j \tag{3-62}$$

where G_j replaces the components of the temperature gradient in a chosen orthogonal frame. A power series expansion for $\alpha_{ij}(\bar{B})$ similar to that (3-41) employed for the galvanomagnetic effects is

$$\alpha_{ij}(B) = \alpha^{(o)}_{ij} + \alpha^{(1)}_{ij,k_1}B_{k_1} + \alpha^{(2)}_{ij,k_1k_2}B_{k_1}B_{k_2} + \cdots \tag{3-63}$$

which gives the coefficient tensors $\alpha^{(N)}_{ij,k_1k_2\ldots k_N}$. The non-vanishing components of these tensors are now determined from the restrictions imposed by the point group symmetry operations of the crystal. The Onsager reciprocity relation for $\alpha_{ij}(\bar{B})$ differs from that for $\rho_{ij}(\bar{B})$. As a result of this, the symmetric and anti-symmetric parts of $\alpha_{ij}(B)$ cannot be taken as odd and even functions of $\bar{B}$ respectively. There are no intrinsic symmetries involved in the tensors $\alpha^{(o)}_{ij}$ and $\alpha^{(1)}_{ij,k_1}$. The tensor $\alpha^{(2)}_{ij,k_1k_2}$ is symmetric only with respect to the indices k_1 and k_2. The corresponding character expressions $\psi_\rho(R)$ for the tensors $\alpha^{(o)}_{ij}$, $\alpha^{(1)}_{ij,k_1}$ and $\alpha^{(2)}_{ij,k_1k_2}$ are

$$\begin{aligned}
\psi_\rho\ (R(\phi)) &= 4\cos^2\phi + 4\cos\phi + 1 \\
\psi_\rho\ (R\ \phi)) &= 8\cos^3\phi + 12\cos^2\phi + 6\cos\phi + 1
\end{aligned} \tag{3-64}$$

and $\psi_\rho\ (R(\phi)) = 16\cos^4\phi + 24\cos^3\phi + 12\cos^2\phi + 2\cos\phi$ respectively. Using these character expressions in equation (3-47), we obtain the characters appropriate to the rotation classes of the group 3m. They are presented in table (3-2) together with the number

of independent components for each tensor.

TABLE (3-2)

TENSOR REPRESENTATION	CLASSES E	$2C_3$	$3C_{\frac{1}{2}}$	NO. OF INDEPENDENT COMPONENTS
$\alpha^{(o)}_{ij}$	9	0	1	2
$\alpha^{(1)}_{ij,k_1}$	27	0	-1	4
$\alpha^{(2)}_{ij,k_1k_2}$	54	0	2	10

It can be seen from table (3-2) that a complete determination of the low field thermomagnetic effects up to B^2 terms in magnetic field requires the measurement of 16 tensor components. The tensor $\alpha^{(o)}_{ij}$ is called the thermoelectric power tensor. But now $\alpha^{(1)}_{ij,k_1}$ does not entirely represent a tranverse effect similar to the Hall tensor, although, it may be called the Nernst tensor. By analogy to the galvanomagnetic effects the tensor $\alpha^{(2)}_{ij,k_1k_2}$ can be called the magnetothermoelectric power tensor. The coefficient scheme for each tensor is obtained as before by denoting the Cartesian orthogonal components of the tensors by the coordinate products that are their indices. The thermoelectric power tensors is

$$\alpha^{(o)}_{ij} = \begin{bmatrix} \alpha_{11} & 0 & 0 \\ 0 & \alpha_{11} & 0 \\ 0 & 0 & \alpha_{33} \end{bmatrix} \qquad (3\text{-}65)$$

and the Nernst tensor (adopting the same replacement as in $\rho^{(1)}_{ij,k_1}$) is

$$\left[\alpha^{(1)}_{ij,k_1}\right]=\begin{bmatrix} \alpha_{11,1} & 0 & 0 & 0 & -\alpha_{11,1} & -\alpha_{23,1} & 0 & \alpha_{123} & 0 \\ 0 & -\alpha_{11,1} & \alpha_{23,1} & -\alpha_{11,1} & 0 & 0 & -\alpha_{12,3} & 0 & 0 \\ 0 & \alpha_{32,1} & 0 & -\alpha_{32,1} & 0 & 0 & 0 & 0 & 0 \end{bmatrix} \quad (3\text{-}66)$$

For the tensor $\alpha^{(2)}_{ij,k_1k_2}$, taking the replacement for ij as (xx, yy, zz, yz, zx, xy, zy, xz and yx) and for k_1k_2 as (xx, yy, zz, yz, zx and xy) we have

$$\left[\alpha^{(2)}_{ij,k_1k_2}\right]=\begin{bmatrix} \alpha_{11,11} & \alpha_{1122} & \alpha_{1133} & -\alpha_{2223} & 0 & 0 \\ \alpha_{1122} & \alpha_{1111} & \alpha_{1133} & \alpha_{2223} & 0 & 0 \\ \alpha_{3311} & \alpha_{3311} & \alpha_{33,33} & 0 & 0 & 0 \\ -\alpha_{2322} & \alpha_{2322} & 0 & \alpha_{13,31} & 0 & 0 \\ 0 & 0 & 0 & 0 & \alpha_{3131} & -\alpha_{32,22} \\ 0 & 0 & 0 & 0 & -\alpha_{22,23} & \tfrac{1}{2}(\alpha_{1111}-\alpha_{1122}) \\ -\alpha_{3222} & \alpha_{3222} & 0 & \alpha_{3131} & 0 & 0 \\ 0 & 0 & 0 & 0 & \alpha_{1331} & -\alpha_{2322} \\ 0 & 0 & 0 & 0 & -\alpha_{2223} & \tfrac{1}{2}(\alpha_{1111}-\alpha_{1122}) \end{bmatrix} \quad (3\text{-}67)$$

Thus an expression similar to (3-52) is obtained:

$$\hat{\alpha}^{(2)}(\vec{B}) = \begin{bmatrix} \alpha_{11} & 0 & 0 \\ 0 & \alpha_{11} & 0 \\ 0 & 0 & \alpha_{33}^{o} \end{bmatrix} + \begin{bmatrix} \alpha_{11,1}B_1 & (\alpha_{12,3}B_3 - \alpha_{11,1}B_2) & -\alpha_{23,1}B_2 \\ -(\alpha_{11,1}B_2 + \alpha_{12,3}B_3) & -\alpha_{11,1}B_1 & \alpha_{23,1}B_1 \\ -\alpha_{32,1}B_2 & \alpha_{32,1}B_1 & 0 \end{bmatrix}$$

$$+ \begin{bmatrix} D_{11} & D_{12} & D_{13} & -D_{24} & 0 & 0 \\ D_{12} & D_{11} & D_{13} & D_{24} & 0 & 0 \\ D_{31} & D_{31} & D_{33} & 0 & 0 & 0 \\ -D_{42} & D_{42} & 0 & D_{85} & 0 & 0 \\ 0 & 0 & 0 & 0 & D_{55} & -D_{72} \\ 0 & 0 & 0 & 0 & D_{24} & \tfrac{1}{2}(D_{11}-D_{12}) \\ -D_{72} & D_{72} & 0 & D_{55} & 0 & 0 \\ 0 & 0 & 0 & 0 & D_{85} & -D_{42} \\ 0 & 0 & 0 & 0 & -D_{24} & \tfrac{1}{2}(D_{11}-D_{12}) \end{bmatrix} \begin{bmatrix} B_1^2 \\ B_2^2 \\ B_3^2 \\ 2B_2B_3 \\ 2B_3B_1 \\ 2B_1B_2 \end{bmatrix} \qquad (3\text{-}68)$$

where D_{pq} ($p = 1, 2 \ldots 9$) and $q = 1, 2 \ldots 6$) is introduced for $\alpha^{(2)}_{ij,k_1k_2}$ and p, q each replace the pair of indices ij and k_1k_2

respectively. The convention for q is the same as before and for p we write 1 = 11, 2 = 22, 3 = 33, 4 = 23, 5 = 31, 6 = 12, 7 = 32, 8 = 13 and 9 = 21. The ordinary matrix summation is valid for the first two tensors and the contributions to $\alpha_{ij}(\bar{B})$ from the last term are in the following order $\alpha_{11}(\bar{B})$, $\alpha_{22}(\bar{B})$, $\alpha_{33}(\bar{B})$, $\alpha_{23}(\bar{B})$, $\alpha_{31}(\bar{B})$, $\alpha_{12}(\bar{B})$, $\alpha_{32}(\bar{B})$, $\alpha_{13}(\bar{B})$ and $\alpha_{21}(\bar{B})$.

B GENERAL RELATIONS BETWEEN THE FIELDS AND TEMPERATURE GRADIENTS

The explicit expressions relating the thermoelectric field components E_i to the temperature gradient G_j can be written down with the help of equations (3-62) and (3-68). The tensor components $\alpha_{ij}(B)$ from the equation (3-68) are

$$\alpha_{11}(\bar{B}) = \alpha_{11} + \alpha_{11,1}B_1 + D_{11}B_1^2 + D_{12}B_2^2 + D_{13}B_3^2 - 2D_{24}B_2B_3$$

$$\alpha_{12}(\bar{B}) = -\alpha_{11,1}B_2 + \alpha_{12,3}B_3 + 2D_{24}B_1B_3 + (D_{11}-D_{12})B_1B_2$$

$$\alpha_{13}(\bar{B}) = -\alpha_{23,1}B_2 + 2D_{85}B_3B_1 - 2D_{42}B_1B_2$$

$$\alpha_{21}(\bar{B}) = \alpha_{11,1}B_2 - \alpha_{12,3}B_3 - 2D_{24}B_1B_3 + (D_{11}-D_{12})B_1B_2$$

$$\alpha_{22}(\bar{B}) = \alpha_{11} - \alpha_{11,1}B_1 + D_{12}B_1^2 + D_{11}B_2^2 + D_{13}B_3^2 + 2D_{24}B_2B_3$$

$$\alpha_{23}(\bar{B}) = \alpha_{23,1}B_1 + D_{42}(B_2^2-B_1^2) + 2D_{85}B_2B_3 \qquad (3\text{-}69)$$

$$\alpha_{31}(\bar{B}) = -\alpha_{32,1}B_2 + 2D_{58}B_1B_3 - 2D_{72}B_1B_2$$

$$\alpha_{32}(\bar{B}) = \alpha_{32,1}B_1 + D_{72}(B_2^2-B_1^2) + 2D_{55}B_2B_3$$

$$\alpha_{33}(\bar{B}) = \alpha_{33} + D_{31}(B_1^2 + B_2^2) + D_{33}B_3^2$$

By substituting these results for $\alpha_{ij}(\bar{B})$ into the equation (3-62), we obtain the following three basic equations:

$$E_1 = [\alpha_{11} + \alpha_{11,1}B_1 + D_{11}B_1^2 + D_{12}B_2^2 + D_{13}B_3^2 - 2D_{24}B_2B_3] G_1$$

$$+ [-\alpha_{11,1}B_2 + \alpha_{12,3}B_3 + 2D_{24}B_1B_3 + (D_{11}-D_{12})B_1B_2] G_2$$

$$+ [-\alpha_{23,1}B_2 + 2D_{85}B_1B_3 - 2D_{42}B_1B_2] G_3$$

$$E_2 = [-\alpha_{11,1}B_2 - \alpha_{12,3}B_3 - 2D_{24}B_1B_3 + (D_{11}-D_{12})B_1B_2] G_1$$

$$+ [\alpha_{11} - \alpha_{11,1}B_1 + D_{12}B_1^2 + D_{11}B_2^2 + D_{13}B_3^2 + 2D_{24}B_2B_3] G_2$$

$$+ [\alpha_{23,1}B_1 + D_{42}(B_2^2-B_1^2) + 2D_{85}B_2B_3] G_3 \qquad (3\text{-}70)$$

$$E_3 = [-\alpha_{32,1}B_2 + 2D_{55}B_1B_3 - 2D_{72}B_1B_2] G_1$$

$$+ [\alpha_{32,1}B_1 + D_{72}(B_2^2-B_1^2) + 2D_{55}B_2B_3] G_2$$

$$+ [\alpha_{33} + D_{31}(B_1^2+B_2^2) + D_{33}B_3^2] G_3$$

These expressions are quite general; by resolving the field and temperature gradient components on any arbitrarily oriented sample it is possible to determine the coefficients. The samples are long, thin cylindrical or rectangular rods. Thus the sample geometry fixes the direction of G_i with respect to the crystal axes. The electric field in the crystal is resolved into three mutually perpendicular components,

one being parallel to the temperature gradient and the other two perpendicular to it.

This is the equation to be employed in the experimental work on the thermomagnetic effects. We now show that the results of the phenomenological theory are consistent with the experimental observations. The Umkehr effect in bismuth is observed for the y-axis sample thermomagnetic power measurements; figure (5-14) shows the sample set up in relation to the field quantities $\bar{E}$, $\bar{B}$ and $\bar{G}$. The requisite equation is then

$$E_2 = \alpha_{22}^{(s)} G_2$$

and also from equation (3-78) we obtain for E_2

$$E_2 = [\, \alpha_{11} - \alpha_{11,1} B_1 + D_{12} B_1^2 + D_{13} B_3^3 \,] \, G_2$$

These two equations define $\alpha_{22}(\bar{B})$ as

$$\alpha_{22}(\bar{B}) = \alpha_{11} - \alpha_{11,1} B_1 + D_{12} B_1^2 + D_{13} B_3^2$$

If $\bar{B} = (0, 0, B_3)$

$$\alpha_{22}(\bar{B}_3) = \alpha_{11} + D_{13} B_3^2 = \alpha_{22}(-\bar{B}_3)$$

and therefore there is no Umkehr effect.

If $\bar{B} = (B_1, 0, 0)$

$$\alpha_{22}(\bar{B}_1) = \alpha_{11} - \alpha_{11,1} B_1 + D_{12} B_1^2 \neq \alpha_{22}(-\bar{B}_1)$$

then the Umkehr effect must occur.

Furthermore in this last equation, as the field values increase, a reversal of sign for $\alpha_{22}(\bar{B}_1)$ is possible, if the sum of $(\alpha_{11,1} B_1 + D_{12} B_1^2)$ is of opposite sign and becomes larger than α_{11}. Finally if $\alpha_{22}(\bar{B})$ is written in the xz-plane as

$$\alpha_{22}(\theta) = \alpha_{11} - \alpha_{11,1} B \cos\theta + D_{12} B^2 \cos^2\theta + D_{13} B^2 \sin^2\theta$$

it satisfies the symmetry relation.

$$\alpha_{22}(\theta) = \alpha_{22}(2\pi - \theta)$$

These results are confirmed experimentally (see Chapter V).

The remaining chapters of this thesis deal with the experimental measurement of the galvanomagnetic and thermomagnetic tensors in annealed and quenched bismuth, and the application of the results obtained in this chapter.

CHAPTER IV

EXPERIMENTAL SYSTEM AND MEASURING PROCEDURE

I - INTRODUCTION

The present chapter deals with the experimental techniques and measuring procedures used for determining the effect of quenching on the galvanomagnetic and thermomagnetic properties of bismuth single crystals.

Two stringent requirements need to be fulfilled for a reliable comparison and assessment of the quenching effects.

1) The galvanomagnetic and thermomagnetic measurements must be performed on the same sample both in the annealed and quenched conditions without changing the contacts and at the same temperatures.

2) Because of the quadratic field dependence of the magnetoresistance and magnetothermoelectric power tensor coefficients, a fixed sample positioning in the magnetic field must be achieved for measurements in both conditions.

Besides these two specific requirements, there are also problems common to all quenching experiments; achievement of a fast cooling rate, prevention of sample contamination and diffusion of foreign impurities are among the important ones. These points have been taken into account in the design of the experiments. The details of the crystal growth, sample preparation, the measuring system and procedures used are presented in the following sections.

II - CRYSTAL GROWTH

Bismuth crystals were grown from 99.9999 % purity starting material by a modified Bridgman technique. Bismuth on solidification expands in volume (3.3 %); crystals grown in rigid containers are subject to severe strain. Soft mould containers, such as tapped alumina or bismuth oxide can be used (Vickers and Greenough 1956; Hurle 1960). Another method of overcoming the problem of straining is to use a smooth-wall conical growth tube where the material is immersed into a silicon oil (Zitter 1962). Expansion on freezing is then no further problem; the crystal is able to "slide up" the conical wall.

The bismuth crystals used here were grown in an evacuated conical tube; it was found that prevention of oxidation at the crystal-glass interface was essential. The growth tubes made of two smooth walled conical pyrex glass funnels (Figure 4-1). Before use the tubes were washed in 5 % HF, 35 % HNO_3 and 60 % water followed by distilled water and then dried. The precast bismuth rods themselves were etched in dilute nitric acid and washed several times in distilled water before being put into the cylindrical extension of the growth tube. The complete tube was placed inside a furnace. To remove any traces of the etching material and volatile oxides several hours of vacuum pumping was carried out below the melting point using a diffusion pump. Then the furnace temperature was raised above the melting point of bismuth (271^{o}C), so that the material melted down into the conical part of the tube while being continuously pumped. The temperature was raised further to about 600^{o}C and the tube tapped

to remove the gas bubbles and to cause the trace of oxide to float to the surface. The tube was then sealed in vacuo and placed in the growth furnace (Figure 4-2). This furnace had three windings and separate controls for the current in each so that the required temperature gradient could be produced. The temperature gradient which experience showed gave satisfactory crystal growth is shown in (Figure 4-3). The current through the windings, and hence the stability of the temperature gradient, was controlled by a solid state potentiometric device. The growth tube was placed on top of a stainless steel rod and lowered through the temperature gradient at a slow constant rate (0.8 mm per hour) by an electric motor coupled through a gear system. The crystals produced had a conical shape of about 3.5 cm diameter and height; they were etched in dilute nitric acid to reveal the grain boundaries, if any: they usually consisted of two big grains. X-ray back reflection Laue photographs showed little indication of their being strained on the surface (Figure 4-4).

III - CRYSTAL ORIENTATION AND SAMPLE PREPARATION

As described in chapter II, for the A7 structure the sign of some tensor components can depend upon the chosen right handed (+x, +y, +z) axial set for a particular crystal under investigation. In the present instance this is the case for the magnetoresistivity tensor components A_{14} and A_{41}. The method of axial assignment to samples used here is now described.

Bismuth cleaves with relative ease along both trigonal and pseudotrigonal directions and etching in both of these planes reveals

sets of slip lines at 60° (or about 60°) to each other. X-ray Laue back reflection photographs along these directions are also difficult to distinguish. As a result, use of the cleavage planes in bismuth, if relied on alone, can result in misorientation of samples. On the basis of the convention for a right handed crystallographic axial set the quadrant in the mirror plane formed by the +y and +z axes contains a pseudo-three fold axis and that formed by the -y and +z axes a pseudo-four fold axis. X-ray back reflection Laue photographs of the crystal were taken to establish the crystallographic directions in relation to these two pseudo-symmetry axes. The y-axis picture (Figure 4-5) is easy to recognise and there is little chance of confusing it with the pseudo-bisectrix direction, and furthermore X-ray Laue back reflection photographs in this direction alone can establish the crystal orientation uniquely (Brown et al. 1968).

Rectangular bar samples (2.5 x 0.25 x 0.25 cm), along the three major crystallographic directions were spark cut and planed. To remove the surface damage due to spark planing the samples were etched in dilute nitric acid and washed. Sample sizes were measured by a travelling microscope.

IV - SAMPLE HOLDER DESIGN

Different sample holders were employed for galvanomagnetic and thermomagnetic effect measurements. Cycling of sample temperature between $77^{\circ}K$ and $544^{\circ}K$ had to be employed during the study. For galvanomagnetic measurements the design of sample holder and sample contacts was intended to meet the following requirements:

1) Thermal expansion resulting from large temperature changes had to be compensated for, otherwise the samples would be strained.

2) Strong and clean contacts were necessary to give Ohmic conductivity during the whole process of quenching.

3) Sample holder design had to allow very fast cooling.

4) In a liquid coolant medium (either liquid nitrogen or water), the temperature gradient between the sample ends had to be so small that negligible thermoelectric voltages were produced.

5) The overall design had to permit easy sample replacement and alignment.

The sample holder design shown in figures (4-6) was found to meet the requirements outlined above satisfactorily, after several trial designs. It consisted of two rectangular copper bars, screwed onto the sides of a cylindrical syndanyo base. To hold the samples copper rods were grooved and fitted with supporting clamps. The sample ends were kept in direct contact with the copper bars by the tension of the light adjustable copper tabs; sample length changes due to the thermal expansion were not restricted. Electrical insulation was provided by the syndanyo base, which was supported by a stainless steel tube. The other end of this tube was soldered to a brass head enabling accurate rotation of the specimen. Thermocouple measurements showed that the temperature gradient along the sample for a sample current of about 0.6 A was negligibly small.

Besides the previous sample holder design requirements it is essential in thermomagnetic measurements to have an additional

heat source and sink, so as to give a steady temperature gradient along the sample length. The sample holder built for this purpose was machined from a cylindrical syndanyo rod (see figure 4-7). The sample was positioned vertically with its axis parallel to that of the rod. It was held between a spring loaded copper plunger with a recessed end to locate the sample and prevent sideways movement and a fixed copper heat sink which made good thermal contact with the copper base of the stainless steel vacuum jacket. A resistance heater in thermal contact with the top copper plunger formed the heat source. The syndanyo rod was supported by a stainless steel tube through which the thermocouples and heater leads passed. The whole sample holder was enclosed by a stainless steel vacuum jacket. The thermocouple leads were passed out from the vacuum jacket through a seal which comprised of a ring and a pad of neoprene.

V - SAMPLE CONTACTS

The sample contacts were spot welded. Platinum wires were found to be the best sample contacts: they bonded ohmically and suffered no work hardening during the quenching process; platinum was used whenever possible. The four-probe configuration usual for galvanomagnetic effect measurements was employed; that is two longitudinal contacts, separated by about 2 cm , and two transverse contacts centred on the sample. The longitudinal voltage probes were positioned well away from the sample ends to minimise Hall field shorting (Volger 1950). Hall voltage measurements were made either using the two transverse voltage probes or by balancing out the 'IR' drop with a 1 Ω rheostat: the latter case was preferred if the probe

positioning was off-centre.

VI - MEASURING SYSTEM

The block diagram shown in figure (4-8) represents the main features of the system used for measuring sample voltages for determination of the galvanomagnetic tensor coefficients. Essentially it was the same system as used for measurements of the low field galvanomagnetic tensor coefficients in antimony (Öktü 1967) and arsenic (Jeavons 1969).

The potentiometer was a precision instrument (Pye type 7600) based on the decade principle (see Stout 1960). Switches were employed throughout; the smallest switched voltage step was 0.1 μV. A Keithley (type 149) electronic millimicrovoltmeter was used as a null detector for measurements at the nonovolt level. This instrument has a sensitivity comparable to the best light-beam galvanometer systems and combines the advantage of fast response, high input resistance and robustness. The resolution of the instrument was sufficient to detect signals below the nonovolt level with a stability of 10 nonovolts in 24 hours. The speed of response was three seconds on the 0.01 microvolt range and increased to less than 0.5 seconds on the 0.1 microvolts and higher ranges (see Erdman and Praglin 1964). Because of the inherent isolation and line pick-up problems involved in these types of null detectors, the elimination of severe mains pick-up required a modification (see Jeavons 1969) mainly confined to some isolations such as the mains transformer and the change of the original 50 Hz chopper frequency to a value of 60 Hz. Stray thermal

e.m.f.s in the measuring circuit were minimised by using copper wires throughout; connections were carefully cleaned and clamped where possible, 'low thermal' solder (70 % Cd 30 % Sn) was used whenever soldering was absolutely necessary.

VII - SAMPLE CURRENT AND TEMPERATURE GRADIENT CONTROL

The detection of the small changes in some tensor components due to quenching required accurate voltage measurements. To measure the small components to an accuracy of 1 % required a system with a resolution of 5 parts in 10^6 and thus a drift stability of approximately 1 in 10^6. The usual stability obtained by manual control of current was quite impractical in this case. To obtain such a stability a transistorised current stabilizer (Palmer 1966) was employed. Figure (4-9) shows the circuit diagram. In principle the current stabilizer acted as a high resistance (about 50 KΩ) inseries with the sample so that any temperature or otherwise induced resistance change in the measuring circuit comprises only a very small fraction of the total circuit resistance; hence fluctuations in sample current were minimised. After a few hours of warm-up a current stability of better than 1 part in 10^6 was achieved. A sample current of about 15A per cm^2 was passed during the measurements and was measured from the potential drop across a 0.01 Ω standard resistance. The current stabilizer, standard resistance, and standard cell were all kept in an oil bath to prevent temperature changes in them.

Similar stability and drift requirements applied for the control of sample temperature and temperature gradient in the thermo-

electric and magnetothermoelectric power measurements. At fixed temperatures, (liquid nitrogen and dry ice in acetone) when the evacuated stainless steel jacket was immersed directly into these liquids, there was no problem in obtaining stable temperature gradients. But to obtain a continuous and slow sample temperature change with small thermal gradients, it was found that the best result was obtained by using the arrangement shown in figure (4-10). It consisted of small inner and large outer dewars. The evacuated stainless steel jacket was held inside the small dewar covered with charcoal. The space between the two dewars was filled with solid CO_2 and then liquid nitrogen poured into both the dewars. The whole system was finally covered by an expanded polystyrene top. This arrangement was found to be very effective both in controlling the average sample temperature change and the temperature gradients along the sample. The system took more than three days to reach room temperature, without creating large temperature gradients and there was hardly any need to use the heater.

VIII - MAGNETIC FIELD ALIGNMENT AND MEASUREMENT

The magnetic fields were obtained from a 4" electromagnet. The magnetic field and the sample were centralized on the axis of rotation. The sample alignment in the magnetic field was achieved mechanically by reference to the plane pole-tip faces, and then checked by plotting the magnetoresistance polar diagrams at moderate fields. Because of the quadratic field dependence of some of the low field tensor components, accurate magnetic field measurements were necessary; a Radio Frequency Labs., Inc. Gaussmeter (type 750)

was used for this purpose. This instrument operated on the Hall effect principle, enabling a sensing element of small physical size to be used for flux densities. The instrument was capable of maesuring from 0 - 1,000 G on the low range and from 0 - 50,000 G on the high range, both these ranges contained twelve subranges. The resolution was 1/10th of a scale division, the reproducibility of a measurement being 2/10th of a scale division. Thus the reading accuracy varied between $\pm$ 0.00002 G on the low range (0.1 G) to $\pm$ 500 G on the high range (50,000 G). A standard 1,000 G magnet and a zero Gauss chamber enabled instrument calibration before every measurement.

IX - QUENCHING AND ANNEALING CYCLES AND EXPERIMENTAL PROCEDURE

In quenching experiments, specimens have to be cooled down rapidly from elevated temperatures. The usual method is to heat a sample either by passing a direct current through the sample or by use of a furnace just above a quenching bath and to plunge the sample rapidly into the coolant medium. As coolants, depending on the required quenching temperature, water, iced brine, liquid nitrogen or liquid helium have often been used.

In this work for annealing and quenching purposes the same system was used. It consisted of a specially built furnace, with a gas supply and a temperature control system attached to it. In order to secure a fixed sample position with respect to the graduated angular scale of the magnet turntable, the sample holder head was located by an assymmetric screw arrangement. Hence the sample holder

could be removed and replaced without readjustment.

Bismuth oxidizes rapidly on heating. The impurities introduced due to oxidation or atomic diffusion from materials in contact can have a very serious effect on the electrical properties of the sample and hence can easily conceal the quenched-in properties. To assure that the sample surroundings were free from oxygen, the inner furnace tube was sealed against the outside atmospheric pressure and heating carried out in oxygen free nitrogen above atmospheric pressure. Two copper constantan thermocouples, precalibrated at the melting point of bismuth and spot welded onto the samples were used to measure the sample temperature inside the furnace accurately. The furnace current and thus the temperature stability was controlled by a Eurotherm TR series temperature controller which allowed a control accuracy of better than 1 %.

The procedure followed for annealing and quenching was as follows.

1) The sample holder was put into the furnace and the system was sealed from the atmospheric pressure.

2) The nitrogen pressure was adjusted through a needle valve to a value slightly above atmospheric pressure and then was left running.

3) The furnace current was switched on and slowly increased.

4) The sample temperature was measured carefully by the thermocouples and finally the rise in furnace temperature stopped when the sample temperature had reached $267 \pm 1^{\circ}C$.

5) The system was kept running at this temperature for at least 36 hours and then the sample temperature lowered slowly to room temperature in steps of 10°C over a period of 6 hours to complete the annealing procedure.

6) For quenching, after the sample had been kept at the premelting temperature for approximately the same time as before, the sample holder system was quickly transferred into a large liquid nitrogen container and in the mean time the thermocouple voltages were recorded on an y - t recorder to indicate the rate of cooling during the quench. Tests showed that the welded thermocouples on the bismuth sample indicate the sample cooling rate fairly well; thermocouples free from a sample showed an instantanious cooling to liquid nitrogen temperature.

Because of the requirements related to the sample alignment in the magnetic field the sample holder head had to be kept fixed to the rest of the system and as a result, during the sample transfer from the furnace a little sample cooling occured. During the quench while the specimen temperature was above the liquid nitrogen temperature the system was stirred. Repeated quenching and annealing cycles were performed in every case to check reproducibility of the results.

The thermoelectric voltages developed along the sample required special attention since their magnitude for a material like bismuth is very large. At nanovolt levels their elimination was essential for accurate galvanomagnetic measurements. Thermoelectric voltages developed along the sample for two reasons.

1) There were standing temperature gradients, mainly related to sample holder design and environment.

2) Temperature gradients resulted from Peltier heating; with a magnitude proportional to the sample current.

Contributions to the sample voltage from the standing temperature gradients can be eliminated by current reversal and averaging, but Peltier heating is an intimate part of the Ohmic voltage and cannot be averaged out. This difficulty, in relation to the sample holder design was avoided by employing small sample currents (0.6 A) and performing the galvanomagnetic measurements in a liquid coolant medium, in fact in either liquid nitrogen or ion-free distilled water. To remove the error voltages due to inexact probe positioning and to separate Hall and magnetoresistance coefficients (which will be described in the experimental configuration section) both current and magnetic field reversal was employed. The measurement procedure was as follows.

1) The apparatus was switched on and left overnight to allow it to establish stability.

2) The magnetic field orientation was set and the Gaussmeter calibrated.

3) The presence of any a.c. pick-up by the millimicrovoltmeter was checked with an oscilloscope.

4) The potentiometer was standardised, the sample current accurately set and checked for any longitudinal temperature gradient in the sample.

5) The potentiometer was switched to measure the sample voltage and the system checked for drift.

6) The voltages and magnetic fields were measured at the required fields and directions.

7) The sample current was reversed and the measurements repeated.

For the case of thermoelectric and magnetothermoelectric power measurements, the steps from 1 to 6 were the same, except that in this case the current control and setting was replaced by the control and setting of the temperature and temperature gradients.

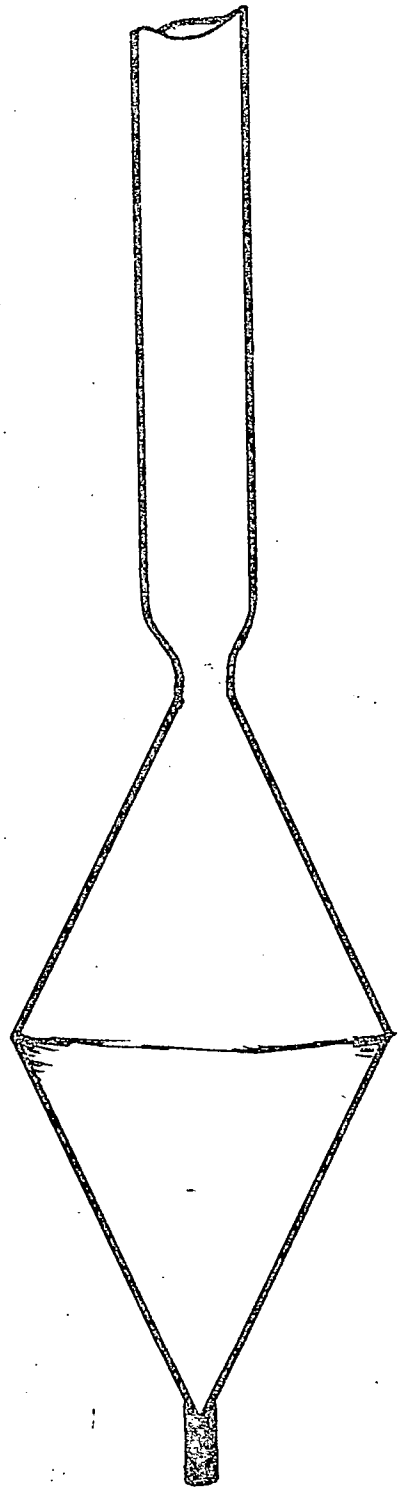

Figure (4-1) : The pyrex growth tube.

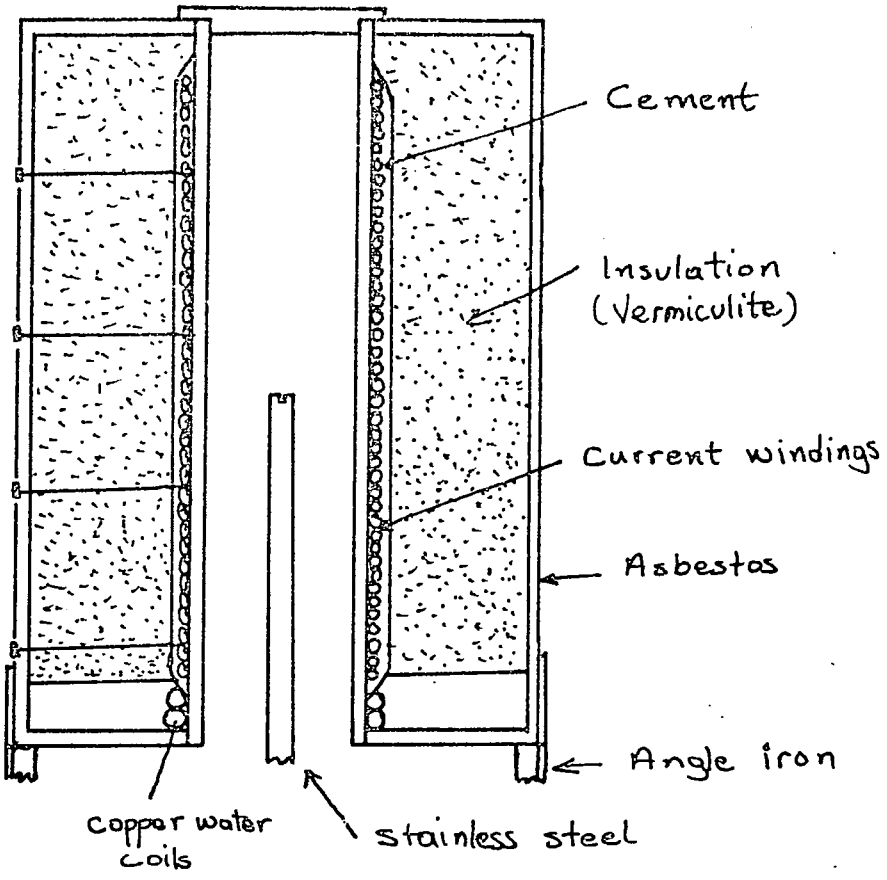

Figure (4-2) : The furnace used for growth of bismuth crystals.

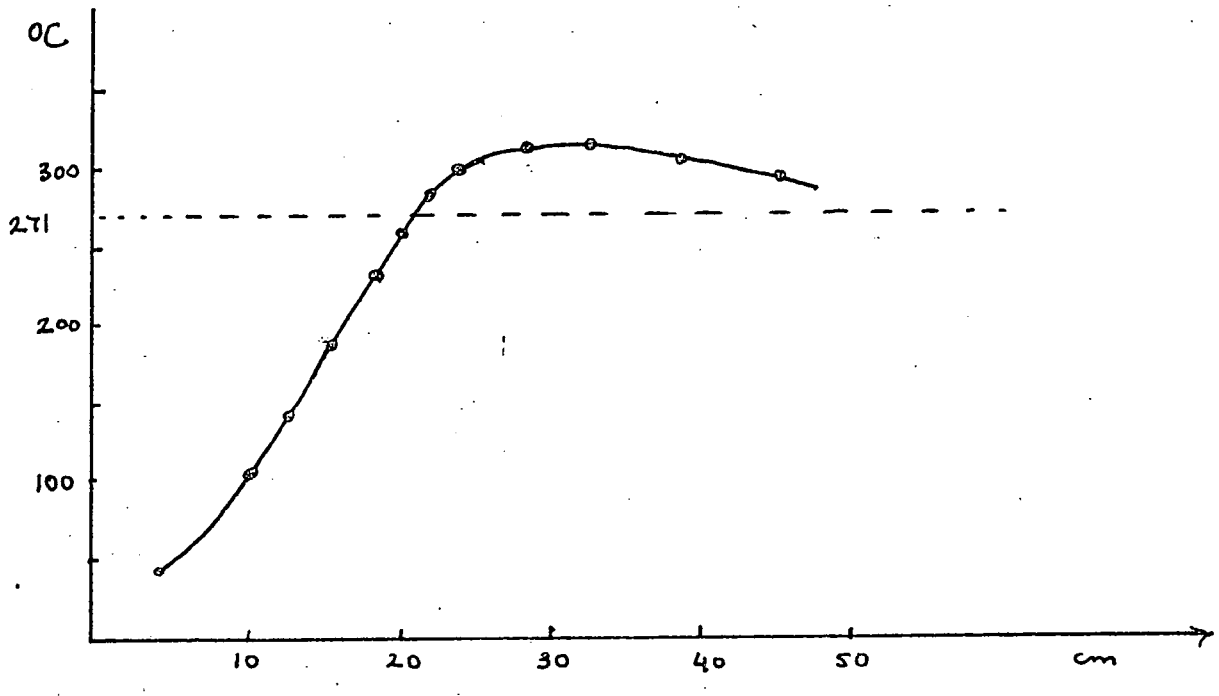

Figure (4-3) : Furnace temperature gradient.

a)

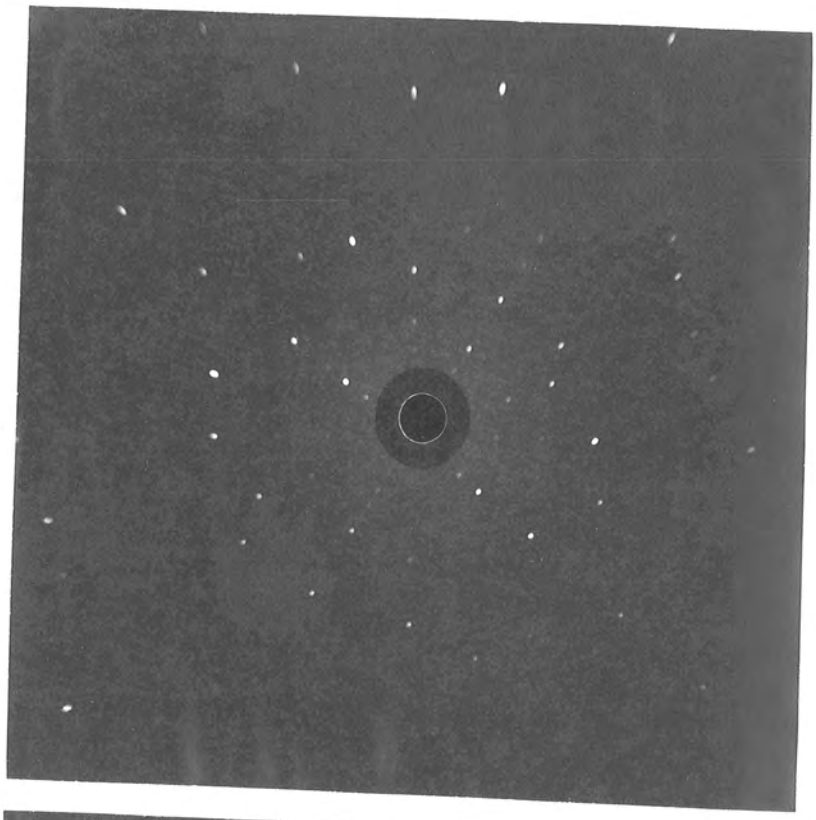

b)

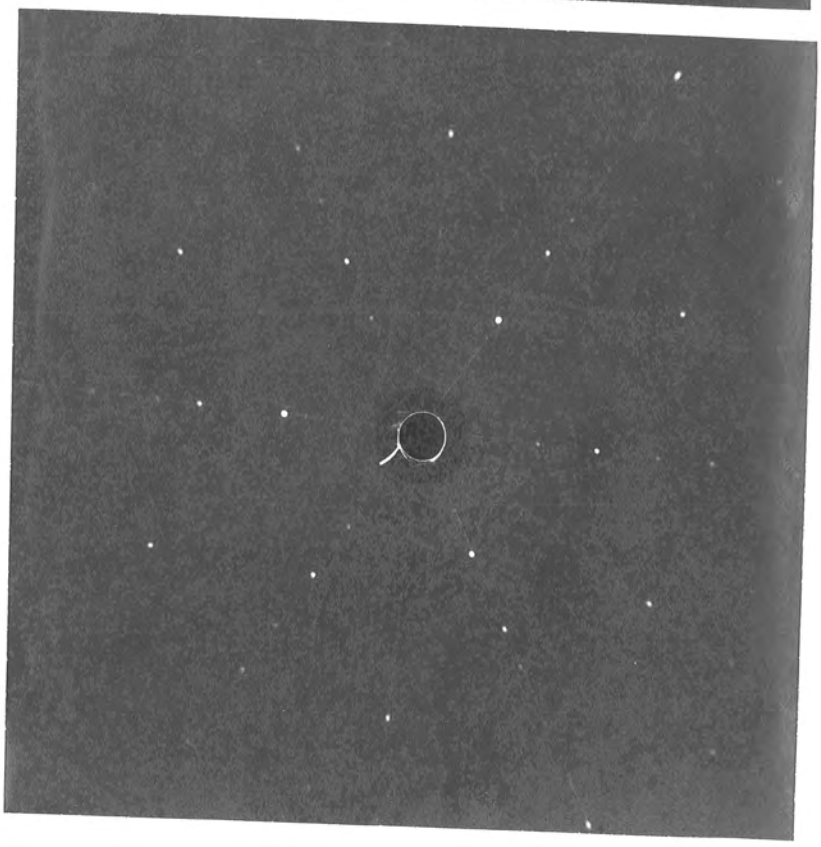

Figure (4-4) : Laue back-reflection X-ray photographs of bismuth. a) along the binary (x) axis; b) along the trigonal (z) axis.

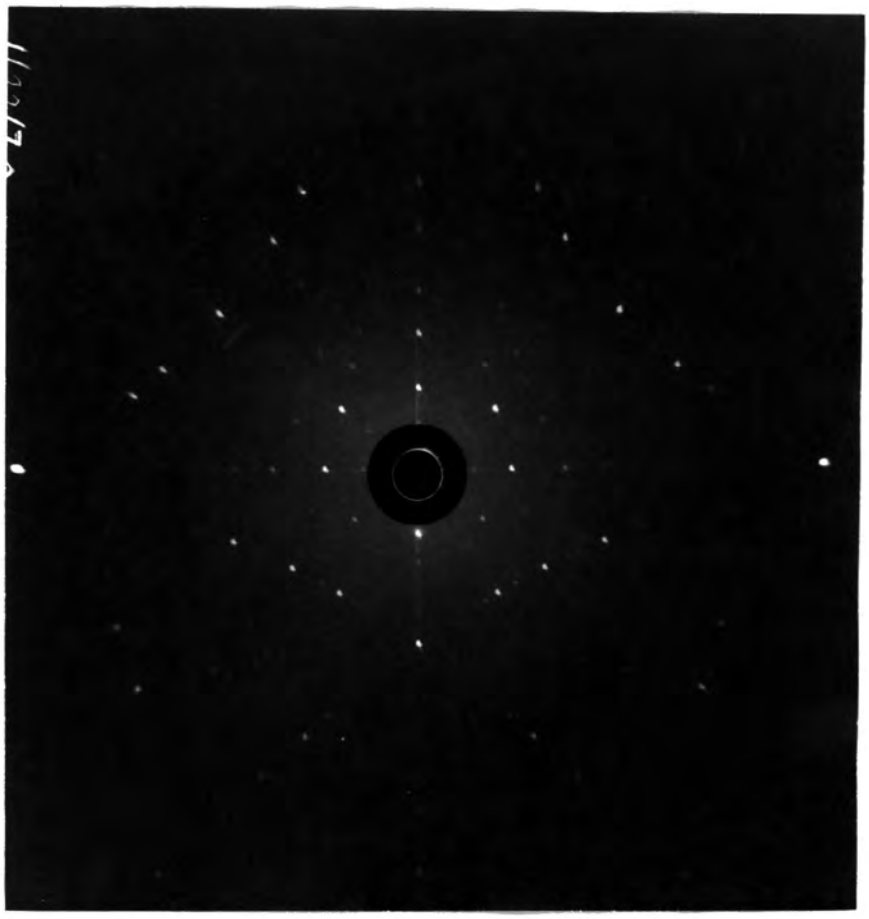

Figure (4-5) : Laue back-reflection X-ray photograph along the bisectrix (y) axis. If the + trigonal (z) is taken to point upward, the + bisectrix points into the figure.

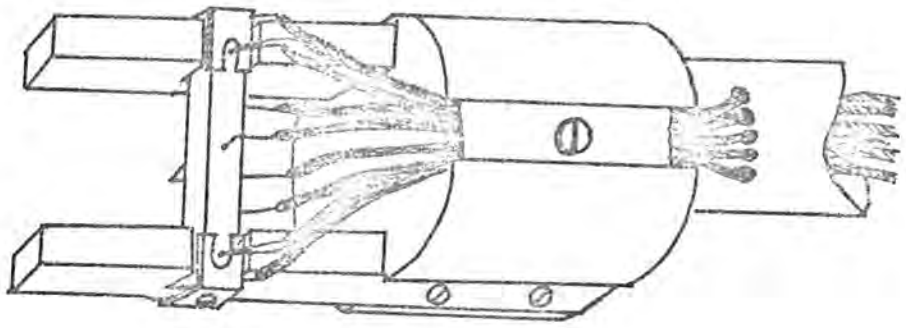

Figure (4-6) : The sample holder design used for galvanomagnetic measurements.

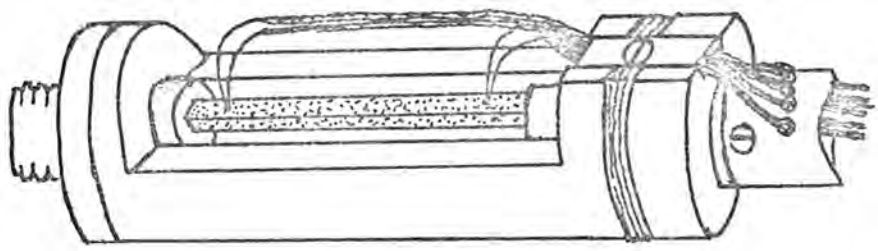

Figure (4-7) : The sample holder design used for thermomagnetic measurements.

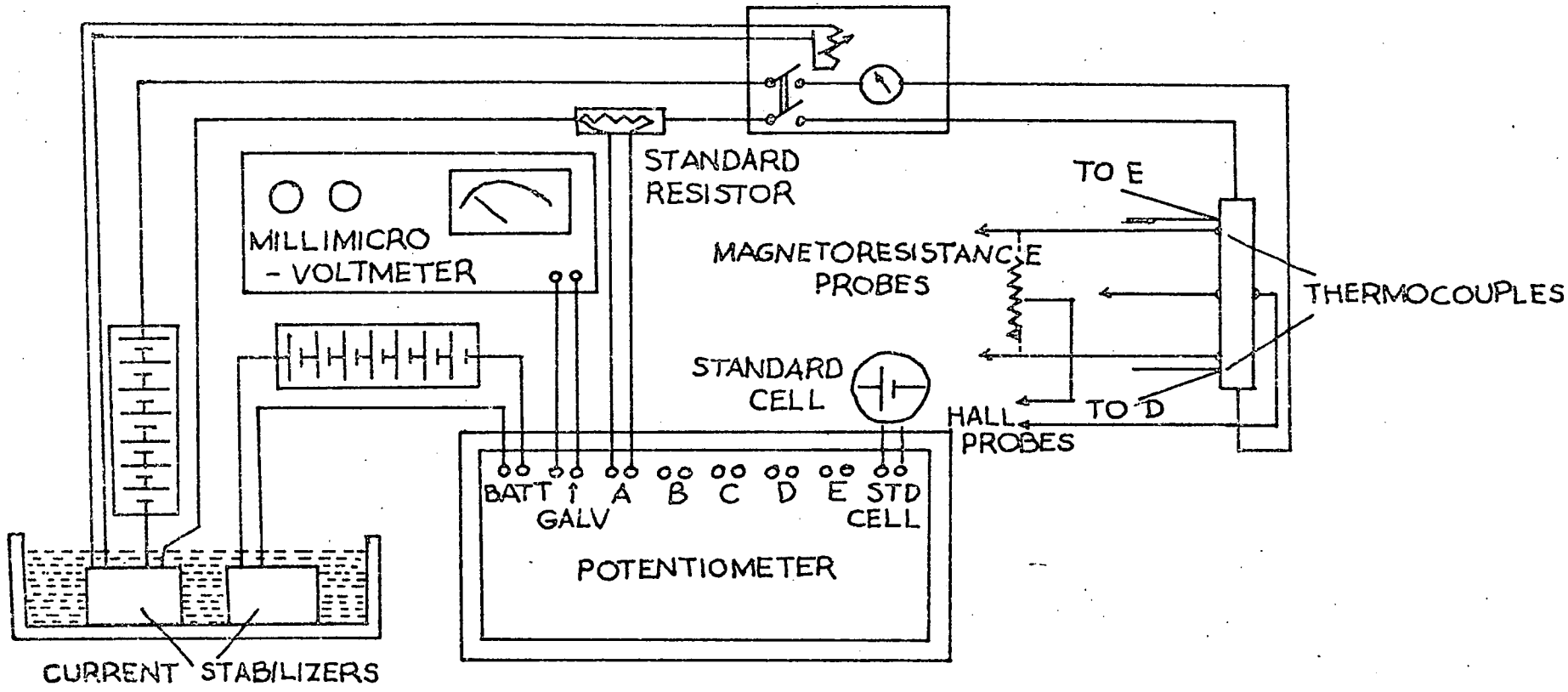

FIG (4-8) THE MEASURING SYSTEM

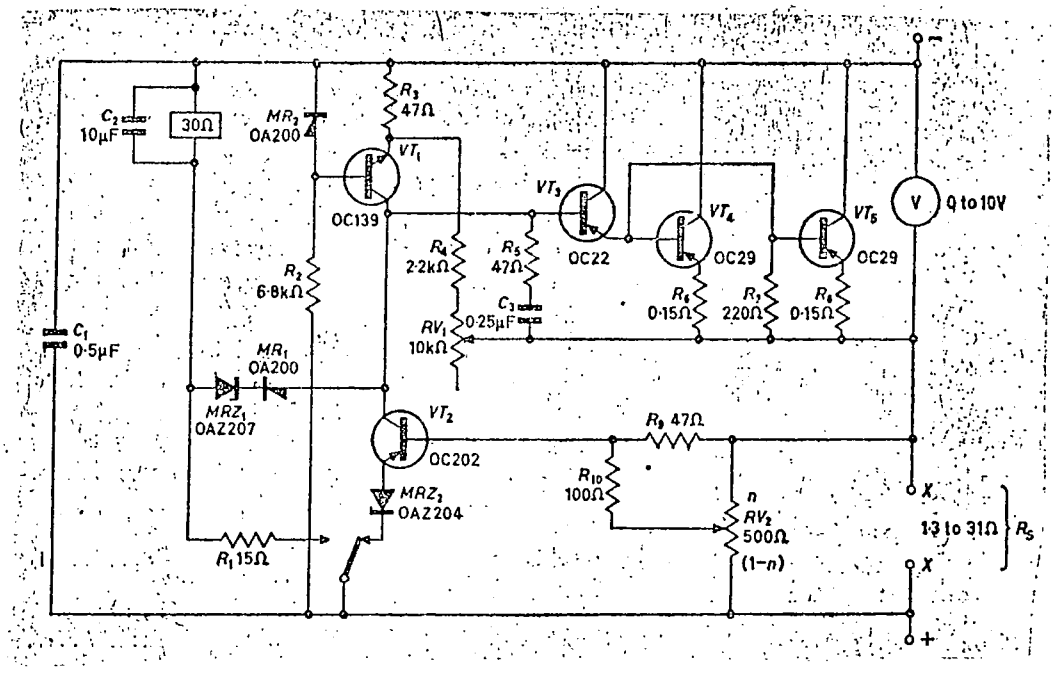

Figure (4-9) : Circuit diagram of the current regulator.

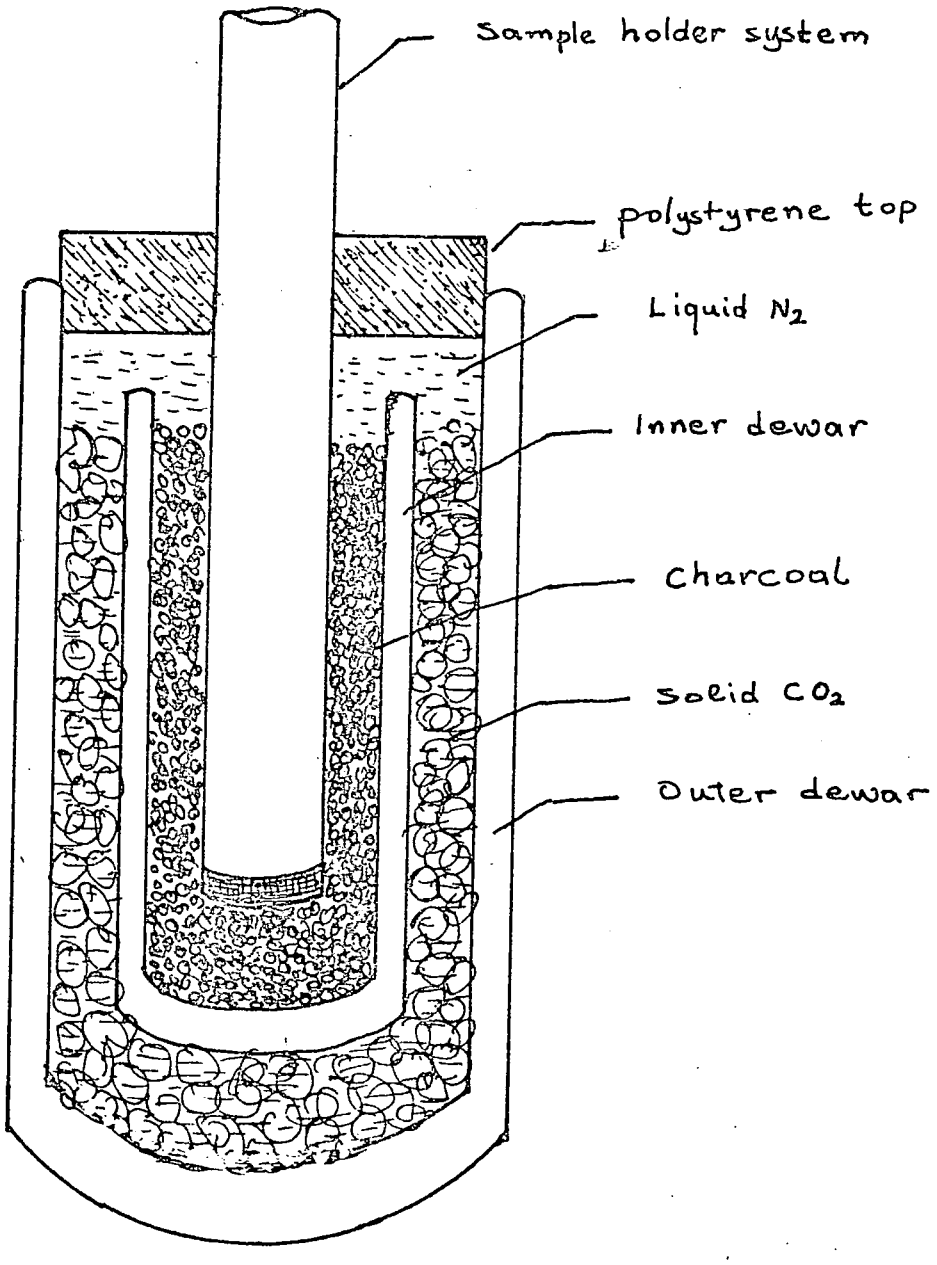

Figure (4-10) : System used to control the temperature variation for the thermoelectric power measurements.

CHAPTER V

THE EXPERIMENTAL CONFIGURATION AND RESULTS

I INTRODUCTION

In this chapter the procedures used for the determination of the tensor components in relation to the chosen sample configurations are described and the experimental results presented. The measurements made during the course of the experiments include

1) The galvanomagnetic tensor coefficients at 77°K and 300°K in the annealed and quenched states.

2) A continuous set of thermoelectric power measurements between 77°K and 300°K.

3) Certain magnetothermoelectric tensor coefficients at 77°K and 196°K.

In the thermomagnetic effect measurements, besides the investigation of the quenching effects on the thermoelectric properties of bismuth the interest was also directed to the application of the theoretical expressions derived for this purpose in chapter III. As discussed previously the peculiar symmetries and the appearance of the Umkehr effect in bismuth provide a very useful means for testing a particular model. The most important information for this purpose can be obtained from y-axis samples, thus an extensive investigation of this data will serve for the purposes of

a) The verification of the predictions of the phenomenological

theory at low fields.

b) The comparison of the results of the theory based on the established Fermi surface model with the experimental data at intermediate fields.

The measurements of the relevant magnetothermoelectric tensor components both on annealed and quenched samples at low and moderate fields were carried out.

II- SAMPLE CONFIGURATIONS USED FOR MAGNETORESISTIVITY TENSOR MEASUREMENTS

To measure the low field galvanomagnetic tensor components, different experimental configurations have been employed by various workers. They all aim at the determination of the 12 low field tensor components. The main difference in choosing a different configuration is probably a preference between employing the smallest possible number of samples or gaining the advantage of isolated measurements of the highest possible number of tensor components. In this work samples cut along each of the three major crystallographic directions have been used. The specimen configurations relative to the directions of current and applied fields are shown in figure (5-1). The requisite equations for each sample configuration can be obtained from equation (3-55) and the procedure for the determination of each one of tensor components for each sample configuration will now be detailed separately.

a) <u>The x-axis samples</u> :

The possible current and magnetic field components for the specimen arrangement, shown in figure (5-1), are given by

$$\bar{J} = (J_1, 0, 0) \quad \text{and} \quad \bar{B} = (B_1, 0, B_3)$$

and the equations corresponding to the longitudinal and tranverse voltage measurements are (see equation 3-55)

$$E_1 = [\rho_{11} + A_{11}B_1^2 + A_{13}B_3^2] J_1 \tag{5-1}$$

and

$$E_2 = [-\rho_{12,3} B_3 + 2A_{14}B_1B_3] J_1 \tag{5-2}$$

The longitudinal voltage measurement E_1 for the magnetic field direction along the x- and z-axes determines the tensor components A_{11} and A_{13} respectively. The transverse voltage measurement E_2 for a magnetic field direction along the z-axis determines $\rho_{12,3}$ directly, but, for the determination of the tensor component A_{14}, it is necessary to perform measurements for a convenient magnetic field direction other than any of the crystallographic axes. If the magnetic field makes an angle $\pm\phi$ with the x-axis in xz-plane, then the magnetic field vector can be resolved into two components in this plane :

$$B_1 = \pm B \cos \phi$$

$$B_3 = B \sin \phi$$

The equation (5-2) now for these magnetic field directions takes the forms

$$E_2(\phi) = [-\rho_{12,3} B \sin \phi + 2A_{14}B^2 \cos \phi \sin \phi] J_1$$

and

$$E_2(-\phi) = [\rho_{12,3} B \sin \phi + 2A_{14}B^2 \cos \phi \sin \phi] J_1$$

The sum of these two equations is written as

$$(E_2(\phi) + E_2(-\phi)) / (4J_1 \cos\phi \sin\phi) = A_{14}B^2 \qquad (5\text{-}3)$$

The plot of this equation for varying B^2 values can be used to determine the tensor component A_{14}. In this case the choice of an angle of $\phi = 45^\circ$ is probably best for maximizing the contribution of the tensor component under consideration. Thus from the x-axis sample the tensor components ρ_{11}, A_{11}, A_{13}, $\rho_{12,3}$ and A_{14} can be determined without changing the sample mounting.

b) <u>The y-axis samples</u> :

For the y-axis sample (see figure 5-1) the possible current and magnetic field components are

$$\overline{J} = (0, J_2, 0) \quad \text{and} \quad \overline{B} = (B_1, B_2, 0)$$

and the equations for longitudinal and transverse voltage measurements are

$$E_2 = [\rho_{11} + A_{12} B_1^2 + A_{11} B_2^2] \; J_2 \qquad (5\text{-}4)$$

and

$$E_3 = [-\rho_{23,1} B_1 + A_{41} (B_1^2 - B_2^2)] \; J_2 \qquad (5\text{-}5)$$

The tensor components A_{12} and A_{11} can be determined by performing the longitudinal voltage measurements for the magnetic field direction along the x- and y-axes respectively. The contribution to the transverse voltage from the Hall tensor component can be separated and measured, if the magnetic field is directed at an angle of 45° to one of the axes in xy-plane, because then the term $B_1^2 - B_2^2$ is equal to

zero and there is no contribution from the tensor component A_{41}. Also the same voltage measurement for the magnetic field direction along the y-axis enables determination of A_{41}. Hence in the y-axis sample the five tensor components can be isolated and measured independently for specific magnetic field directions.

c) The z-axis samples :

Fianlly for z-axis samples for the current and magnetic field components we have (see figure 5-1)

$$\bar{J} = (0, 0, J_3) \quad \text{and} \quad \bar{B} = (0, B_2, B_3)$$

and the equations for longitudinal and transverse voltage measurements are

$$E_3 = [\rho_{33} + A_{31} B_2^2 + A_{33} B_3^2] J_3 \tag{5-6}$$

and

$$E_2 = [-A_{41} B_2^2 + 2A_{44} B_2 B_3] J_3 \tag{5-7}$$

The contributions due to the tensor components A_{31}, A_{33} and A_{41} can be separated and measured in turn by applying the magnetic field along the y- and z-axes for longitudinal and transverse voltage measurements. The procedure for the determination of the tensor component A_{44} is similar to that used for A_{14}; the transverse voltages are measured for a field direction of ϕ and $-\phi$ from one of the axes. The magnetic field components can be written as

$$B_2 = B \sin \phi$$

$$B_3 = \pm B \cos \phi$$

Then the equation (5-7) for $E_2(\pm\phi)$ becomes

$$E_2(\phi) = [-A_{41} B^2 \sin^{12}\phi + 2A_{44}B^2 \sin\phi \cos\phi] J_3$$

and

$$E_2(-\phi) = [-A_{41} B^2 \sin^2\phi - 2A_{44}B^2 \sin\phi \cos\phi] J_3$$

The difference of these two equations can be put into the form

$$(E_2(\phi) - E_2(-\phi)) / (4J_3 \cos\phi \sin\phi) = A_{44} B^2$$

and used to determine the tensor component A_{44}. The choice of an angle of $\phi = 45^\circ$ is again preferable.

Due to the type of sample contacts required and the necessity of permanent sample mounting, only two types of electric field measurement were possible for each sample : one longitudinal, the other transverse. The sample configurations chosen here enabled the isolation of most of the tensor components, and hence the contributions resulting from most tensor components have been measured independently of the others. The exceptions are the two tensor components A_{14} and A_{44}.

An important aspect to be tested is whether the changes which occur in the electrical properties of samples on quenching arise from plastic deformation due to uneven temperature changes along the sample during the quench or if they truely result from a reversible process, such as the creation of point defects. The most important test of this is to repeat the measurements on a given sample in the annealed and quenched conditions created several times in succession. This procedure has been carried through many times : usually after several cycles of

annealing and quenching, the contacts become noisy and this precluded further repetition. Typical recorded plots of the sample cooling rate for x, y and z specimens are given in figure (5-2). These plots represent the voltage drop on copper constantan thermocouples from 576°K to 77°K against the time in seconds.

III - THE LOW FIELD MAGNETORESISTIVITY TENSOR RESULTS

The data were first obtained by measuring the voltages corresponding to the increase in magnetic field strength in steps of $25\text{-}10^{-4}$ T . (In the experimental work all the magnetic field quantities were measured in units of gauss. But theoretical calculations are based on SI units system. Hence from now on the magnetic field quantities will be referred in this terminology 1 gaus = 10^{-4}Weber/m^2 = 10^{-4} Tesla) and then for reversed current and magnetic field directions. The average of the four sets of measurements obtained are plotted and presented in figures (5-3) - (5-10). These plots represent the low field measurements on annealed and quenched samples; to show the relative change in magnetoresistivity on quenching, the annealed and quenched sample measurements are compared as $\rho_{ij}(B_k)$ versus B_k^2. The plots in figure (5-3) - (5-10) demonstrate an important point : the low field condition ($\hat{\mu} \cdot \bar{B} << 1$) is valid for magnetic field values up to 150.10^{-4} T in bismuth at 77°K.

The measured values of the twelve low field magnetoresistivity tensor components, obtained from several samples in the annealed and quenched conditions are listed in table (5-1).

TABLE (5-1) : Low field magneto-resistivity tensor components at 77°K.

z-sample	Tensor Components					Sample Condition
	ρ_{33}	A_{31}	A_{33}	A_{41}	A_{44}	
z(I)	3.40	152	12.0	20	-19	Annealed
	3.36	133	9±8	23	-14	Quenched
	3.42	155	12.5	19.7	-19	Annealed
	3.37	136	10.0	--	--	Quenched
z(II)	3.44	154	12.0	19.3	-17.4	Annealed
	3.37	132	9.2	13.0	-14.0	Quenched
	3.45	157	12.2	19.6	-17.1	Annealed
	3.37	130	9.4	23.3	-14.3	Quenched
	3.44	155	12.0	19.0	-17.0	Annealed
	3.38	133	9.0	--	--	Quenched

y-sample	Tensor Components					Sample Condition
	ρ_{11}	A_{11}	A_{12}	$\rho_{23,1}$	A_{41}	
y(I)	3.28	137	170	10.5	18.2	Annealed
	3.46	142	158	--	--	Quenched
y(II)	3.27	138	173	10.7	19.3	Annealed
	3.48	143	154	8.7	23.0	Quenched
	3.23	138	172	10.9	18.8	Annealed
	3.47	141	155	8.7	24.0	Quenched

TABLE (5-1) : Low field magneto-resistivity tensor components at $77^{o}K$ (Cont)

x-sample	Tensor Components					Sample Condition
	ρ_{11}	A_{11}	A_{13}	A_{14}	$\rho_{12,3}$	
x(I)	3.22	141	30.4	34	-0.20	As grown
	3.22	138	33	34	-0.21	Annealed
	3.45	143	26	36	-0.15	Quenched
	3.27	139	32.5	34	-0.20	Annealed
	3.48	142	26.3	36.5	-0.14	Quenched
	3.24	138	32	34	-0.20	Annealed
	3.51	137	26.4	36	-0.14	Quenched
	3.22	138	32.5	34	-0.20	Annealed

The units are $10^{-7}\ \Omega$ m, $10^{-6}\ \Omega$ m T^{-1} and $10^{-6}\ \Omega$m T^{-2} for ρ_{ij}, $\rho_{ij,k}$ and A_{ij} respectively.

Inspection of the changes induced by quenching on each tensor component does not provide an immediate simple picture: most tensor components are reduced but some are increased in value. An interesting observation is that the anisotropy of the zero-field resistivity is lessened: ρ_{11}, which is the smallest component, is increased and ρ_{33} is decreased.

As can be seen, certain tensor components (ρ_{11}, A_{11} A_{41}) were obtained twice because they are available from measurements made on different sample configurations. Their values are identical within the experimental error; the homegeneity of the boule is good. Further and even more important, the agreement shows that on quenching the different specimens behave in the same fashion and the number of quenched-in defects is the same for all of the samples. Another check is available both on the data and indeed on the model itself. The ellipsoidal band model for bismuth is described by eight independent variables (μ_1 , μ_2 , μ_3 , μ_4 , N , ν_1 , ν_3 and P). The number of measured tensor components up to B^2 terms in magnetic field are 12. Therefore there must be four identities among these tensor components. Two of these identities are particularly simple and can be used for checking the consistency between the measured values of these tensor components. These identities are given by Zitter (1962); they are expressed in terms of the conductivity tensor components as

$$S_{12} + 2S_{33} = 3S_{11} - 2S_{44} , \tag{5-8}$$

$$S_{11} + 4[(\sigma_{23,1} S_{13} / \sigma_{12,3}) + (\sigma_{11} S_{31} / \sigma_{33})] \tag{5-9}$$

$$= 3S_{12} - S_{44} [2 + (8 \sigma_{11} \sigma_{23,1} / \sigma_{12,3} \sigma_{33})]$$

The ratios between the two sides of equations for the measurements in this work compute as 0.90 and 1.12 for equation (5-8) and 0.92 and 1.13 for equation (5-9) for annealed and quenched data respectively. These values are consistent within the approximations related to the model and the experimental errors.

The signs of the tensor components A_{14} and A_{41} were determined by examining the results of the measurements corresponding to the equations (5-3) and (5-5) in relation to the right handed coordinate set (+x, +y, +z) assigned to the samples used. From equation (5-5), for a magnetic field direction along the y-axis, we have

$$E_3 = -A_{41} B_2^2 J_2$$

thus the sign of A_{41} is related directly to the signs of E_3 and J_2 and follows immediately. A similar examination of the results of equation (5-3) evidences the method used to obtain the sign of A_{14}. For the right-handed axial convention adopted here, both tensor components were found to be greater than zero in the annealed and quenched conditions.

The room temperature measurements for the low field tensor components are listed in table (5-2).

TABLE (5-2) : Low field magnetoresistivity tensor components at 300°K

ρ_{11}	ρ_{33}	$\rho_{12,3}$	$\rho_{23,1}$	A_{11}	A_{12}	A_{13}	A_{31}	A_{33}	A_{14}	A_{41}	A_{44}
11.7	13.8	-0.05	1.62	0.92	1.90	0.24	0.09	2.71	0.27	0.19	-0.14

The units are 10^{-7} Ω m, 10^{-6} Ω m T^{-1} and 10^{-6} Ω m T^{-2} for ρ_{ij}, $\rho_{ij,k}$ and A_{ij} respectively.

In direct contrast to the experimental observations at 77°K, the results of the measurements on annealed and quenched samples at room temperature are equal within the experimental errors. Experiment showed that after quenched samples have been heated up to the room temperature and left to stabilize for several hours, the resistivity had returned effectively to the room temperature values in the annealed state and further when these samples were taken back down to 77°K from room temperature they had resistivities which were almost identical ($\sim$ 1%) to the values they had had in the annealed conditions. These results imply that the quenched-in defects annealed out between 77°K and room temperature. Later it will be shown in section III of this chapter that the thermoelectric power obeys the same rule: annealed and quenched samples are different at 77°K but have become identical by the time that room temperature is reached. The point will be developed later. However, the annealing behaviour has been investigated still further. After a sample has been quenched to 77°K and left for a short time to achieve equilibrium, measurements showed that for several minutes the resistivity (ρ_{33}) of z-samples slowly increased from the immediate quenched value. This change was about 4%. However the x- and y-sample resistances ($\rho_{11} = \rho_{22}$) did not show this time change. No resistivity changes ensued after the samples had been left for many hours: it can be concluded that after the small and rapid change in ρ_{33} subsequent to quenching there is no appreciable diffusion of the quenched-in defects at 77°K in bismuth.

IV - THE MAGNETORESISTIVITY TENSOR AT INTERMEDIATE MAGNETIC FIELDS

Towards the end of this work Dr. J.E. Aubrey (Department of Applied Physics, University of Wales Institute of Science and Technology, Cathays Park, Cardiff) kindly supplied to us the results of his derivation of the magnetoresistivity expressions appropriate to the Fermi surface model for the A7 structure semimetals. We kindly thank him for his kind permission to use his results (Aubrey 1971). As a result, it was decided to extend the study further and find out the way in which quenching could effect the intermediate magnetic fields data for bismuth. So measurements on the x-axis sample were extended to the magnetoresistivity tensor coefficients at intermediate fields both in the annealed and quenched conditions. The sample configuration used was the same as that used for the low field case; thus the measurements of $\rho_{11}(B_1)$ and $\rho_{11}(B_3)$ tensor components could be made at intermediate magnetic fields. The field range covered was up to 0.5 T . The results of the measurements are presented in figures (5-11) and (5-12). The quenching effects were found to be again pronounced. The analysis of the intermediate field data, based on Dr. J.E. Aubrey's theoretical results, will be provided in the next chapter.

V - SAMPLE CONFIGURATIONS USED FOR THERMOELECTRIC AND MAGNETOTHERMOELECTRIC POWER MEASUREMENTS

The thermoelectric power measurements were carried out on two samples prepared and cut along the y- and z-axis directions. The two

zero-field tensor components α_{11} and α_{33} were measured between 77°K and 300°K in both annealed and quenched samples. The measurement sequence followed here was annealed-quenched-annealed using the procedures described previously. For both thermoelectric voltages and temperature measurements two precalibrated copper-constantan thermocouples were used. Calibration charts, computed separately for each thermocouple in steps of 0.1 °C, were drawn up and used to calculate the temperature gradients and the average sample temperatures. The copper leads of the thermocouples were employed for thermoelectric voltage measurements along the samples. Results, converted from Seebeck coefficients relative to copper to absolute values by subtraction of the absolute Seebeck coefficient of copper, for α_{11} and α_{33}, are given in figure (5-13). The effect of quenching on the thermoelectric properties of bismuth is pronounced and, furthermore the character of the induced changes along the y- and z-axis are given in reverse order, as observed for the resistivity: while the thermoelectric power increases in the y- direction on quenching, a reduction along the z-axis occurs.

The magnetothermoelectric power measurements were also carried out on the same specimens. The sample configuration, the direction of the temperature gradient and the plane including the magnetic field directions for these measurements are shown in figure (5-14). The y-axis sample data includes magnetothermoelectric power measurements for magnetic field directions along $\pm$x- and z-axis as a function of magnetic fields up to 0.5 T and magnetothermoelectric power polar diagrams for several constant magnetic field values. The polar diagrams

for $\alpha_{22}(\bar{B})$ at 77°K and 196°K are presented in figures (5-15) - (5-18), for both the annealed and quenched conditions. In quenched y-axis samples the magnetic field dependence are much smaller than those in annealed samples. This is emphasised when the magnetic field is directed along or nearly along the x-axis. In this configuration the magnetic field dependence is large for the sample in the annealed condition; after quenching, they are much reduced. Measurements at room temperature proved to be insensitive to the magnetic field strength up to a field value of 0.5 T ; this demonstrates that the tensor components at this temperature are extremely small.

Of particular interest are field reversal effects. When the magnetic field, directed along the x-axis, is made larger than 0.075T, the sign of $\alpha_{22}(B_1)$ reverses when the specimen is in the annealed condition. This effect occurs (see for instance figure 5-16) whenever the magnetic field is directed near to the x-axis direction but dies away rapidly as the field direction is deviated from the x-axis; furthermore the field required to produce sign reversal becomes larger the greater the direction of $\bar{B}$ from the x-axis. The entire effect is illustrated in figure (5-19), in which is plotted the field required to produce a zero thermoelectric voltage against angle of deviation of the applied magnetic field from the x-axis. It can be seen that there is a marked difference for this required field, when the magnetic field is taken through 180°. When the sample is quenched, the smaller magnetic field effects can be seen clearly in this figure. The required field to produce a zero thermoelectric voltage is now much greater than that for the annealed specimen; for the magnetic fields available (up to

about 0.5 T) the sign reversal can only be seen for a range of about 20^{o} around the x-axis for $-\bar{B}$. At 196^{o}K no sign reversal can be seen for magnetic fields up to 0.5 T even in the annealed specimen. The magnetothermoelectric power polar diagrams for $\alpha_{22}(\bar{B})$ show the symmetries predicted by the phenomenological theory presented in chapter III, i.e. $\alpha_{22}(+B_3) = \alpha_{22}(-B_3)$, $\alpha_{22}(+B_1) \neq \alpha_{22}(-B_1)$ and $\alpha_{22}(\theta) = \alpha_{22}(\pi - \theta)$ where θ is measured from the z-axis and represents the angle between the magnetic field direction and the trigonal z-axis.

The low field tensor components related to the y-axis data can be determined from equation (3-59); here the components of the magnetic field $\bar{B}$ and the temperature gradient $\bar{G}$ are given by (see figure 3-14)

$$\bar{B} = (B_1, 0, B_3) \quad \text{and} \quad \bar{G} = (0, G_2, 0)$$

and the corresponding equation for the thermomegnetic voltage then reduces to

$$E_2 = [\alpha_{11} - \alpha_{11,1} B_1 + D_{12}B_1^2 + D_{13}B_3^2] G_2$$

When the magnetic field is along the z-axis, we have for E_2

$$E_2 = [\alpha_{11} + D_{13} B_3^2] G_2$$

which can be used to determine tensor component D_{13}. For a magnetic field direction along $\pm$x-axis the following equations for E_2 are obtained

$$E_2(+B_1) = [\alpha_{11} - \alpha_{11,1}B_1 + D_{12}B_1^2] G_2$$

and

$$E_2(-B_1) = [\alpha_{11} + \alpha_{11,1}B_1 + D_{12}B_1^2] G_2$$

The sum of these two equations

$$(E_2(+B_1) + E_2(-B_1)) / 2G_2 = (\alpha_{11} + D_{12}B_1^2)$$

determines the tensor component D_{12} and the difference

$$(E_2(+B_1) - E_2(-B_1)) / 2G_2 = \alpha_{11,1}B_1$$

the tensor component $\alpha_{11,1}$.

The linear variation in $\alpha_{22}(B)$ for magnetic fields along the x- and z-axis is presented in figures (5-20) and (5-21). As is observed from the polar data, the Umkehr effect occurs only along the $\pm x$ direction. A least-mean-squares fit to this data (linear and polar) in terms of the bismuth band parameters is presented in the next chapter.

Similar measurements were carried out on the z-axis specimen. By use of equation (3-69) in relation to figure (5-14) for this sample configuration, we have

$$\bar{B} = (B_1, B_2, 0) \quad \text{and} \quad \bar{G} = (0, 0, G_3)$$

and

$$E_3 = [\alpha_{33} + D_{31}(B_1^2 + B_2^2)] G_3$$

For a field direction along either of the crystallographic axes ($\pm x$ or $\pm y$), the tensor component D_{31} can now be determined. The resulting low field tensor components at 77°K and 196°K are presented in table (5-3).

TABLE (5-3) : The low field magnetothermoelectric tensor components.

Tensor Components	α_{11}	α_{33}	$\alpha_{11,1}$	D_{12}	D_{13}	D_{31}	Temperature
Annealed	- 43	- 86	0.53	67.8	-25.0	-61.9	77°K
	- 53	-100	0.24	5.2	-2.2	-8.0	196°K
Quenched	- 47	- 79	0.44	63.2	-12.3	-58.6	77°K
	- 55	- 96	0.20	4.4	-0.9	-7.2	196°K
Units	10^{-6} V/°K		10^{-4}V/T°K	10^{-4} V/T^2 °K			

Magnetothermoelectric power polar diagrams for $\alpha_{33}(\bar{B})$ in xy- plane are presented in figure (5-17). Both for annealed and quenched specimens the data shows a uniform increase in $\alpha_{33}(B)$ as the field increases. However, the magnetic field induced anisotropy is less pronounced for the quenched sample condition. Another important result for $\alpha_{33}(B)$ is that it shows a 3-fold symmetry in xy- plane, indicating the existence of an Umkehr effect for field directions along the $\pm$x-axis.

The phenomenological theory presented in Chapter III, accounts quantitatively for the general features observed here. Indeed the measured values (Table 5-3) of $\alpha_{11,1}$ and D_{12} at 77°K for the low field contributions up to B^2 predict a sign reversal in $\alpha_{22}(B_1)$ at 0.0835 T which is in reasonable agreement with the measured value of 0.075 T.

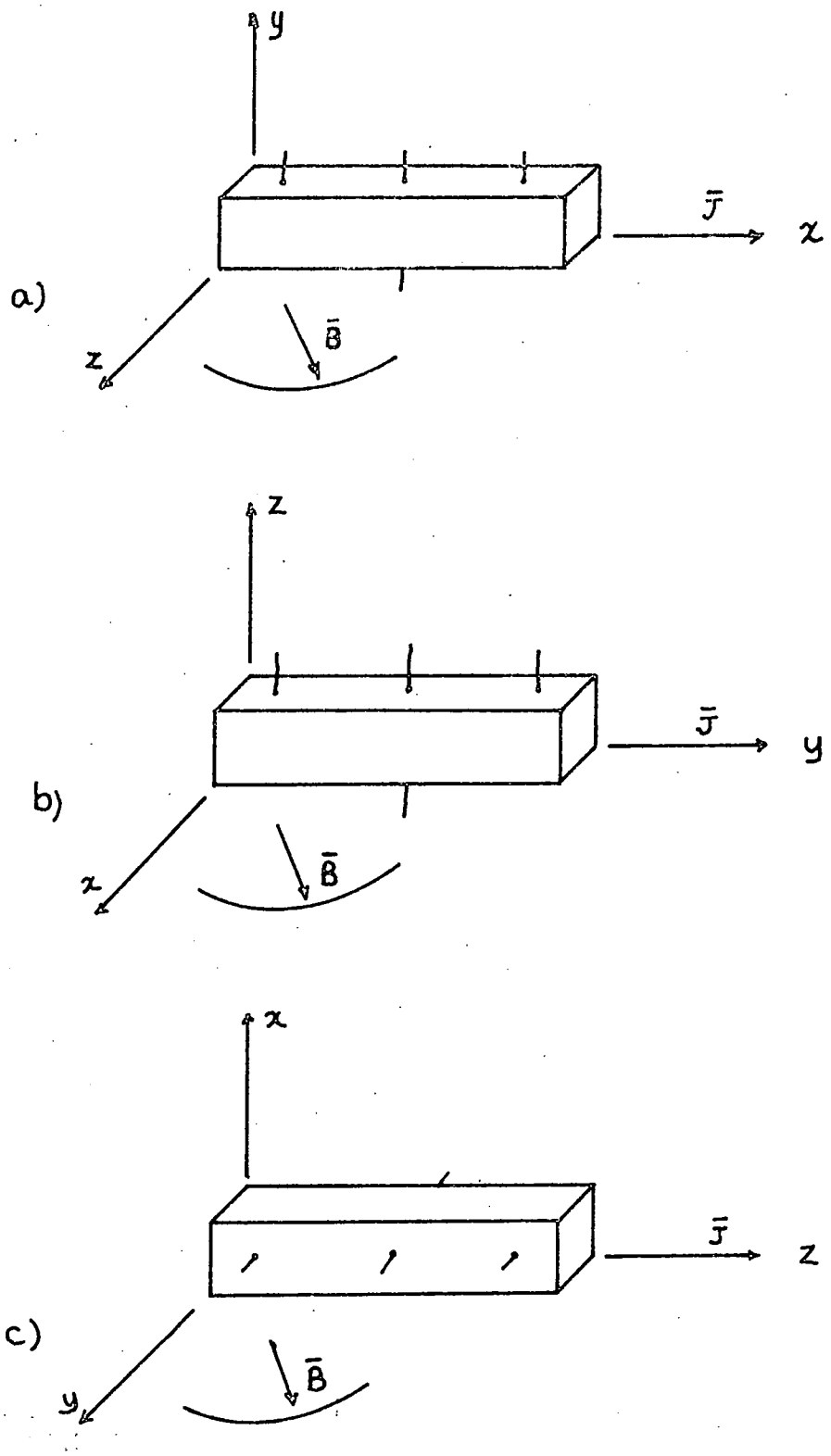

Figure (5-1) : The sample configurations used for the galvanomagnetic effect measurements.

a) x-axis sample, b) y-axis sample,

c) z-axis sample.

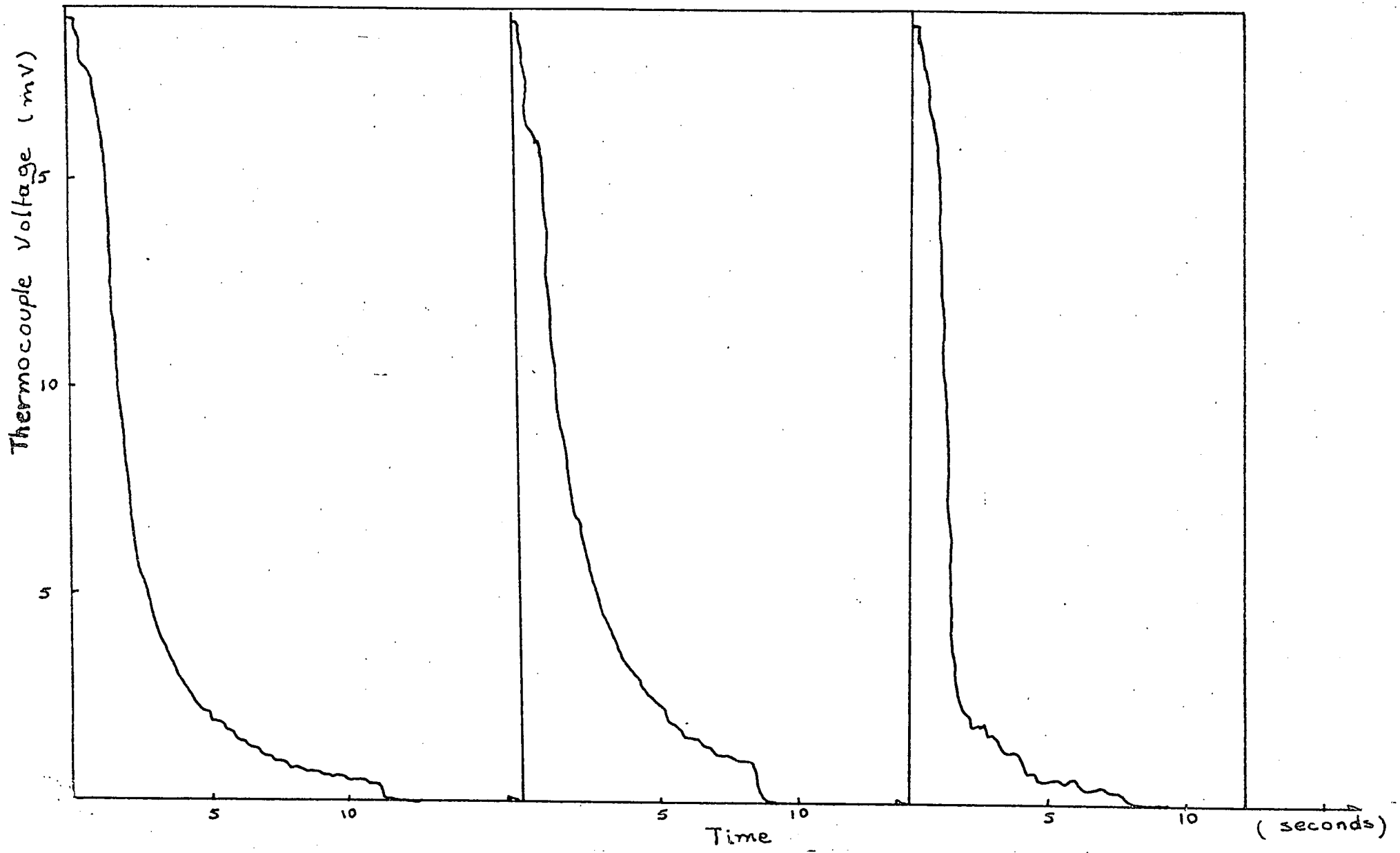

Figure (5-2) : Example of the sample cooling curves obtained from three different samples.

Figure (5-3) - (5-10)

Typical set of measurements of magnetoresistivity tensor components. The gradients of these curves give the low field coefficient indicated in figures. The filled circles are the data obtained after quenching and the open ones for the sample in the annealed state. (77°K)

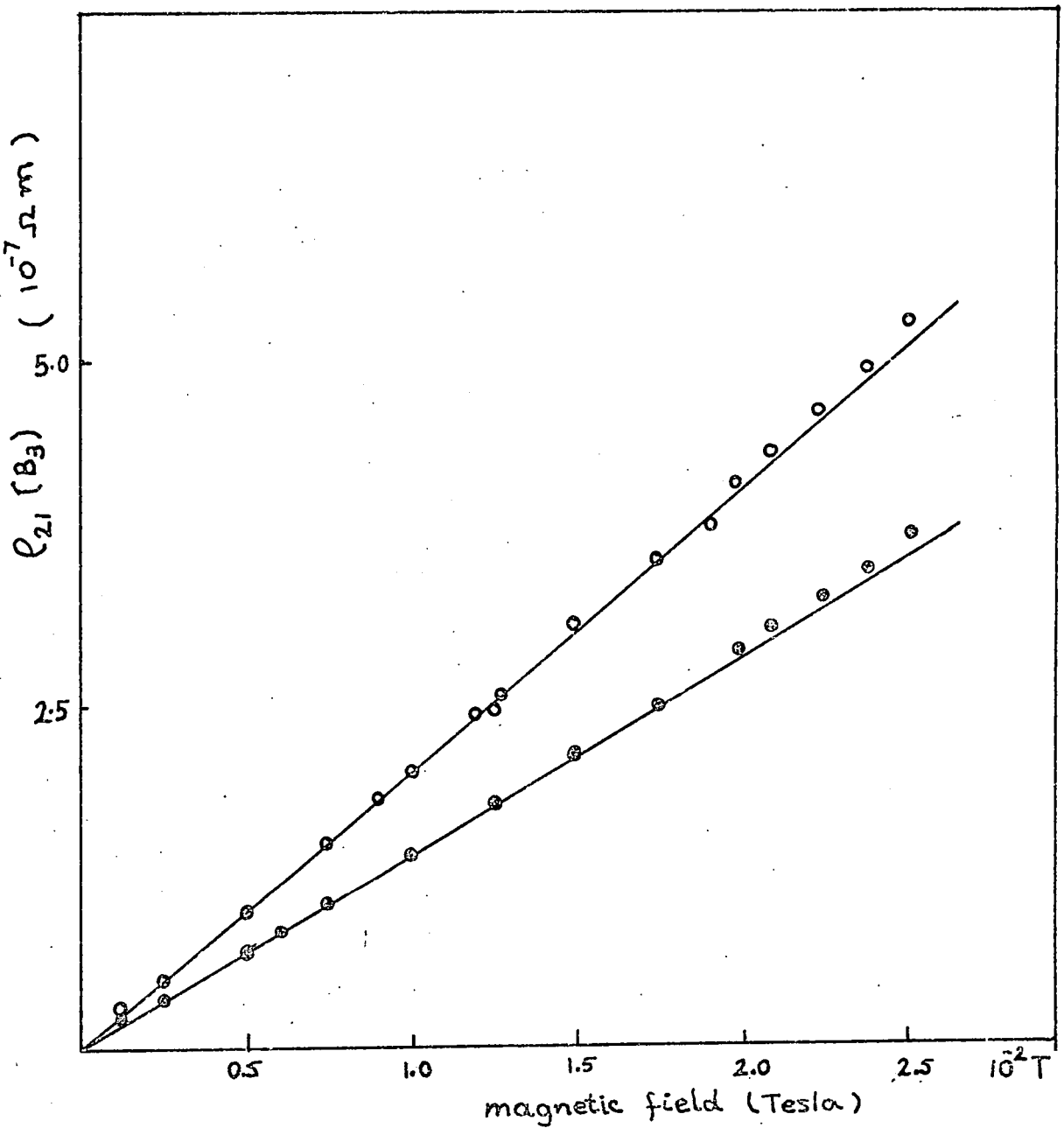
ρ_{21} (B_3) ($10^{-7}\Omega m$)
5.0
2.5
0.5
1.0
1.5
2.0
2.5
10^{-2}T
magnetic field (Tesla)

$\rho_{12,3}$

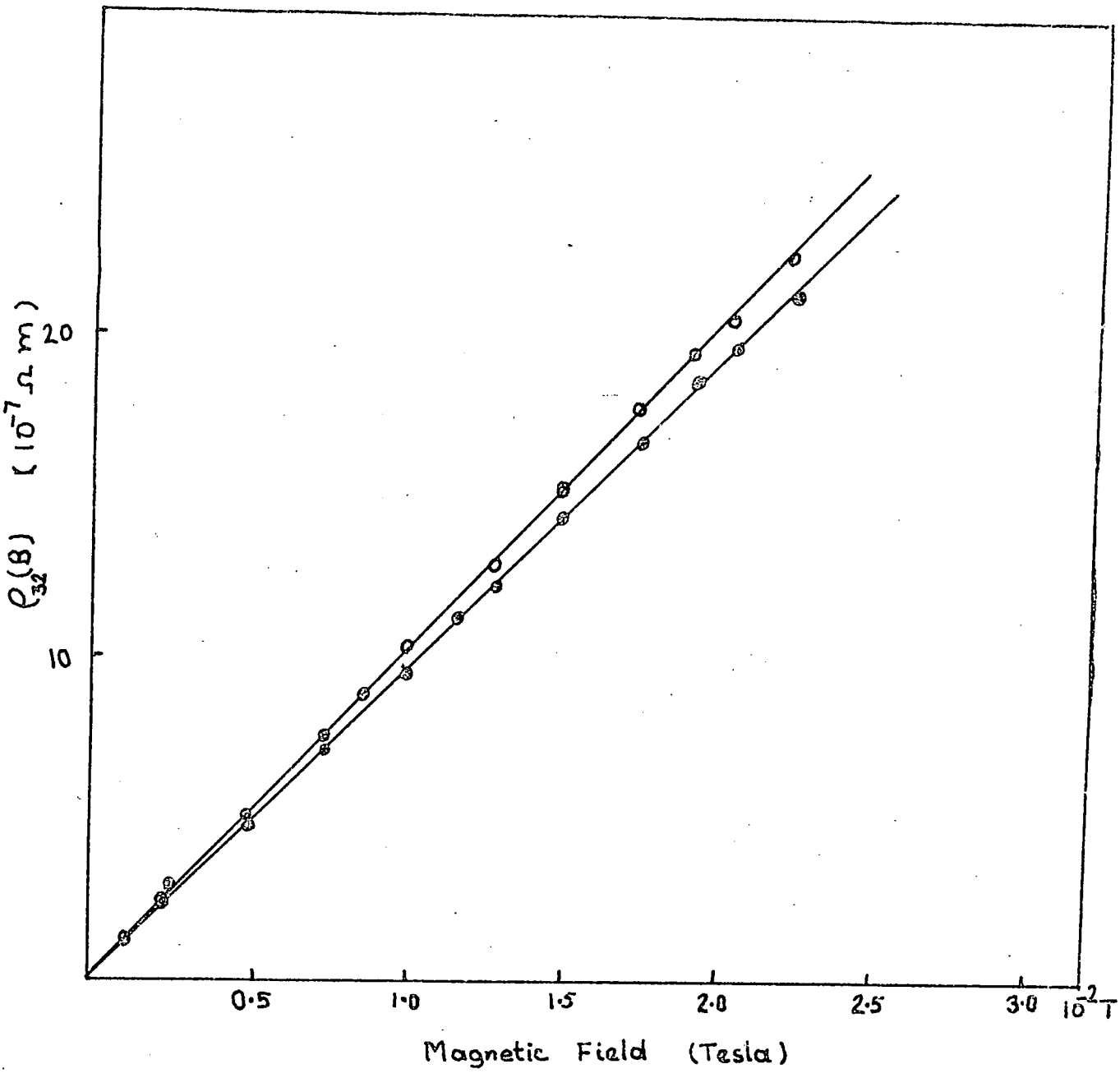
$\rho_{32}(B)$ ($10^{-7}\Omega m$)
20
10
0·5
1·0
1·5
2·0
2·5
3·0
10^{-2}T
Magnetic Field (Tesla)

$\rho_{23,1}$

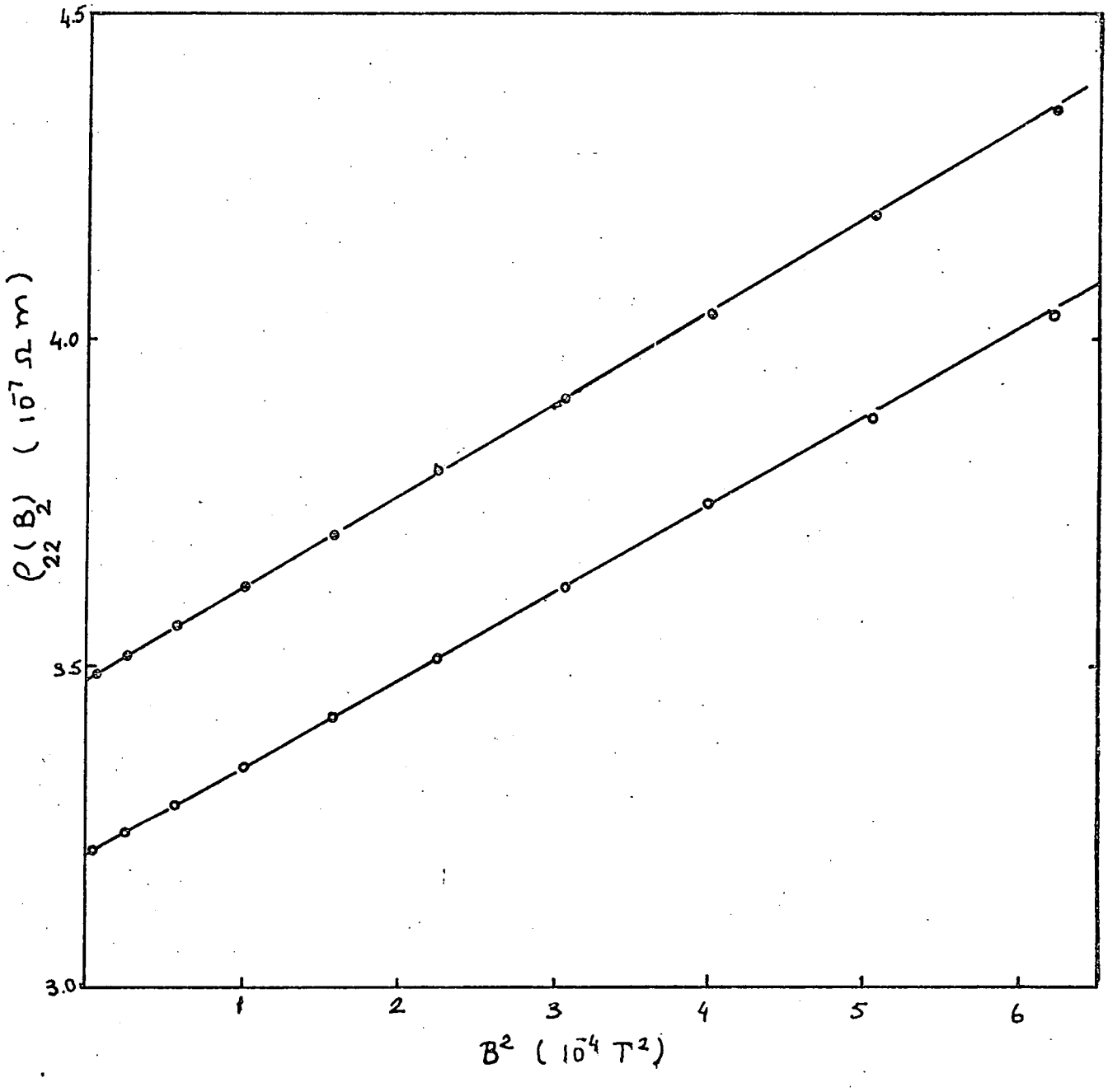

A_{11}

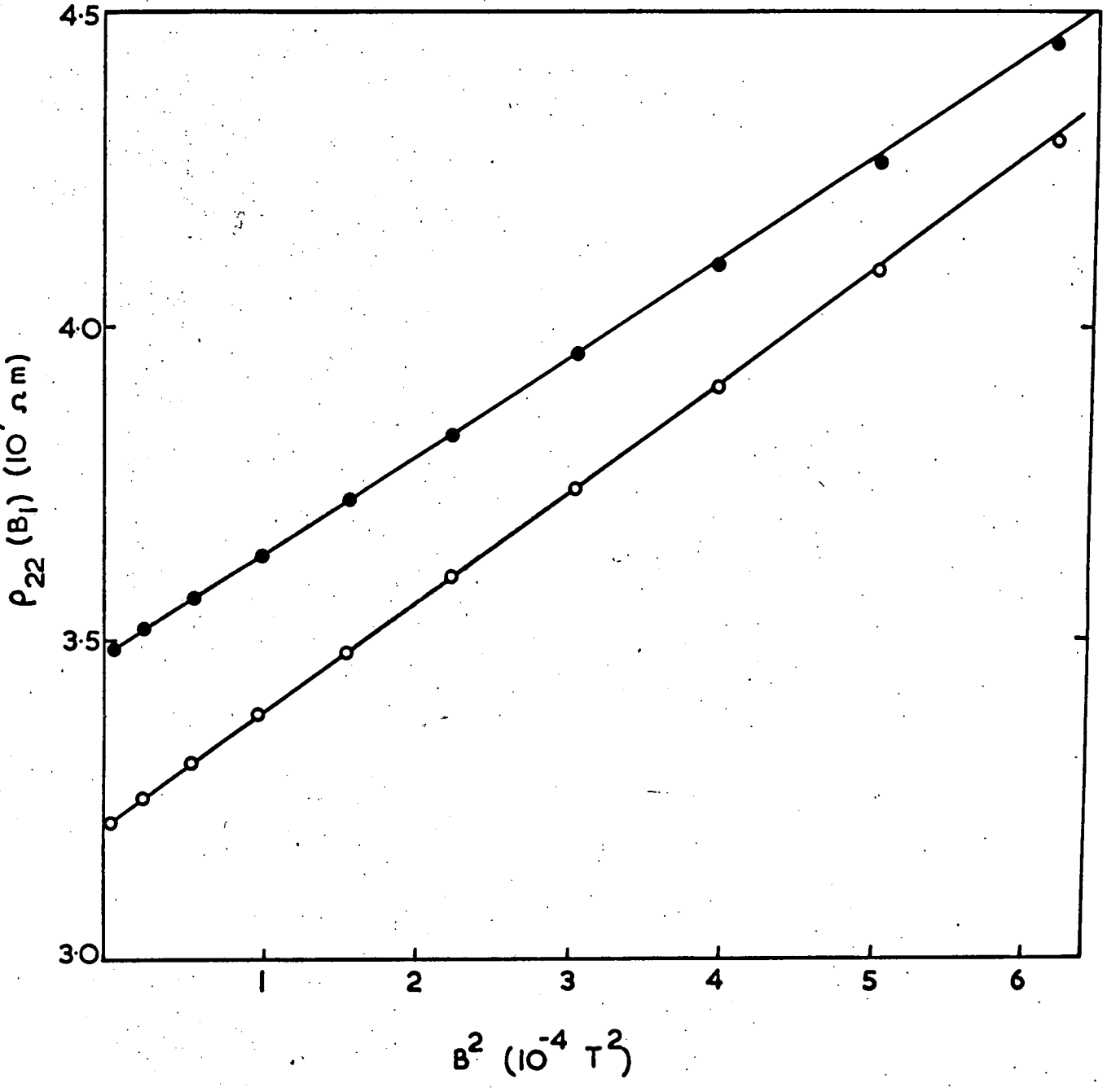

A_{12}

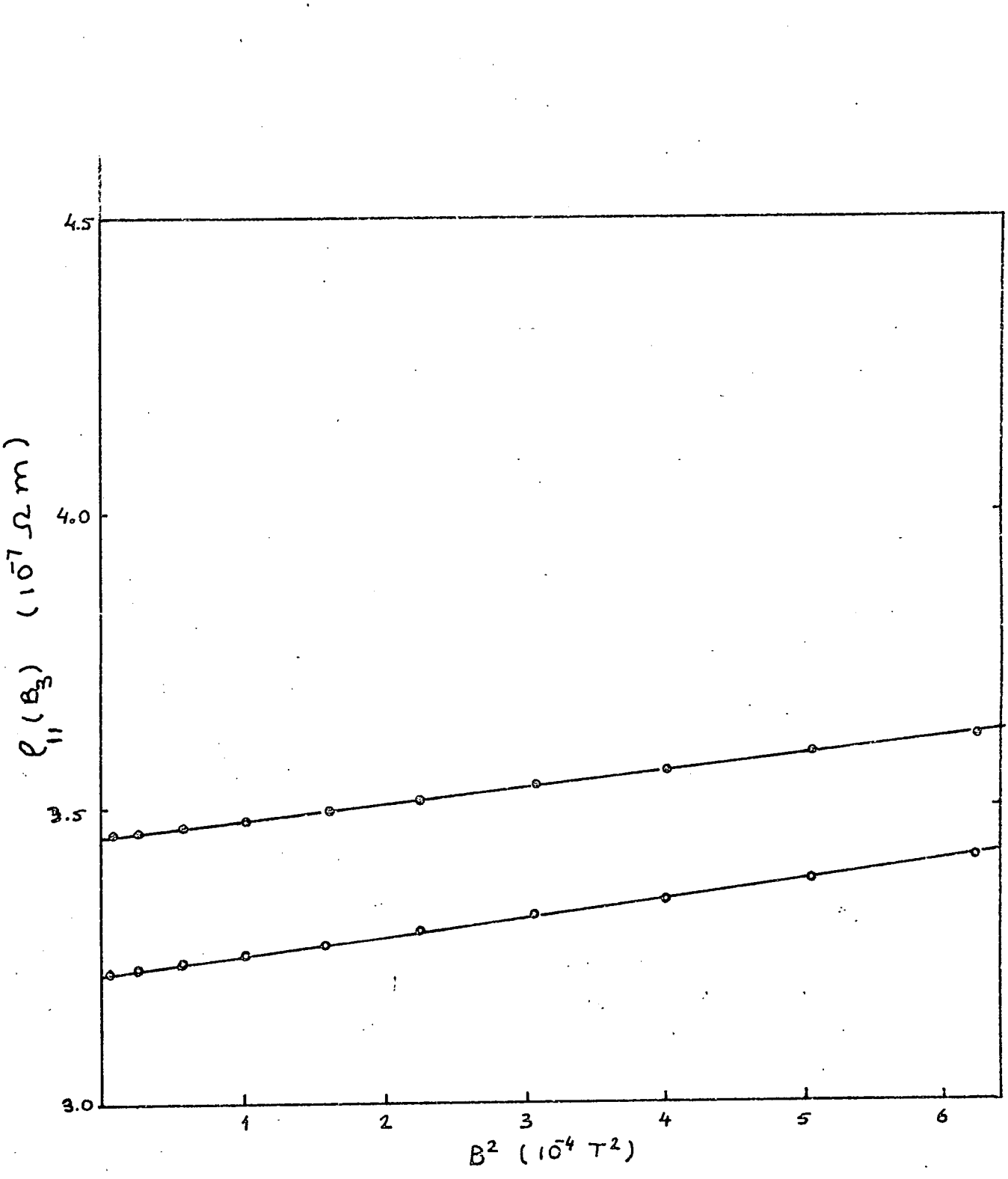
4.5
4.0
3.5
3.0
$\rho_{11}(B_3)$ $(10^{-7}\ \Omega\,m)$
1
2
3
4
5
6
B^2 $(10^{-4}\ T^2)$

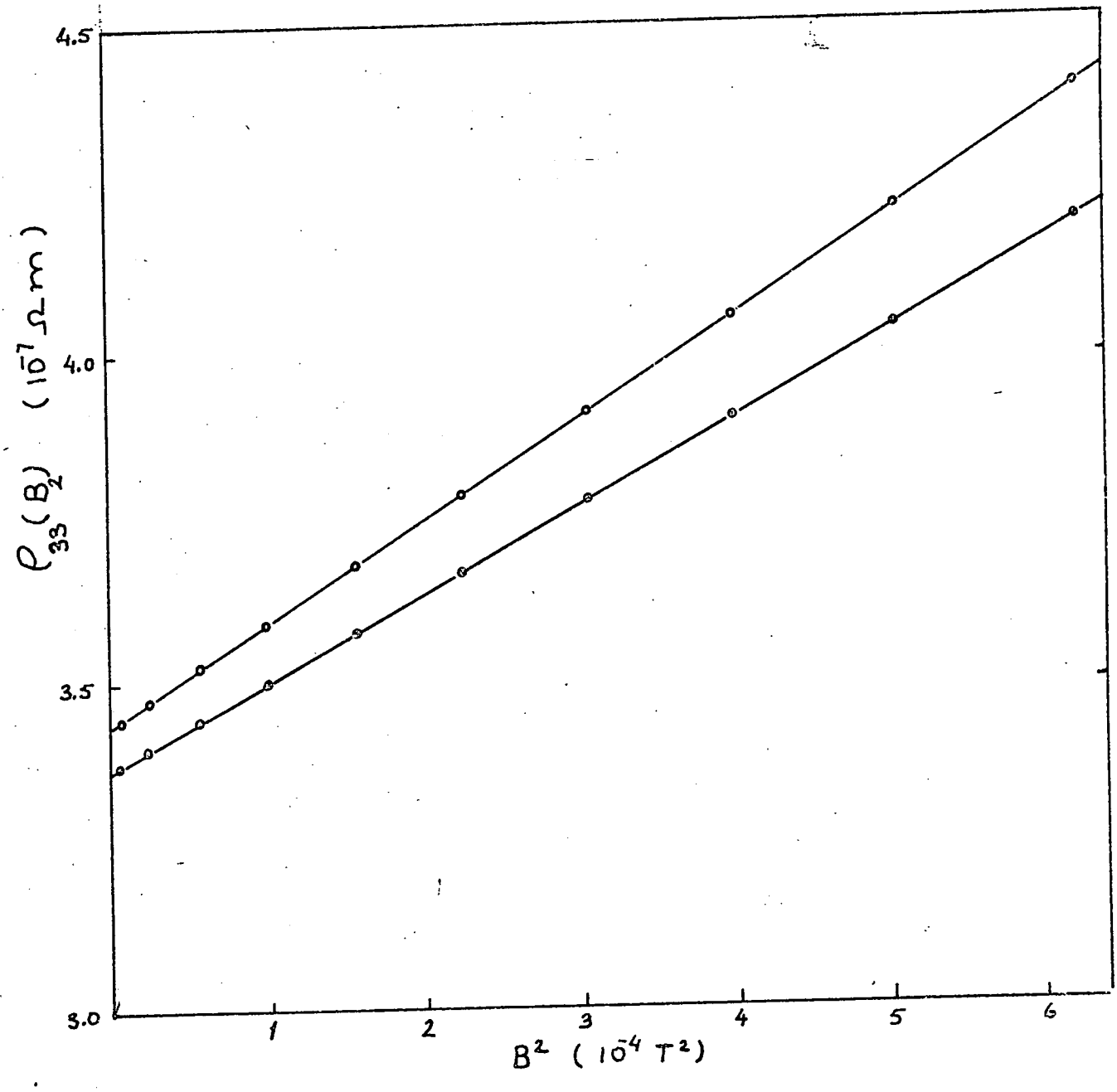

A_{31}

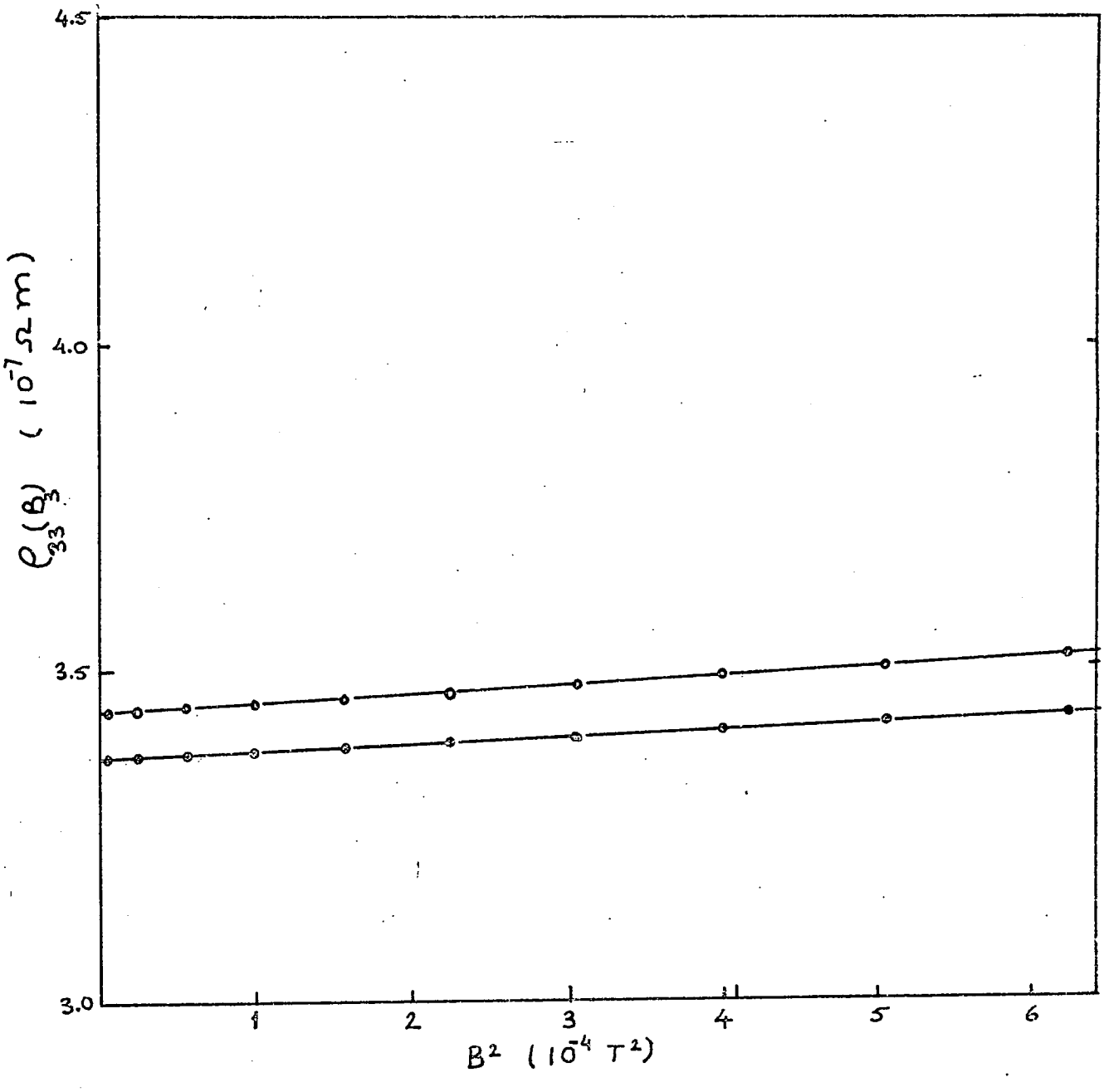

A_{33}

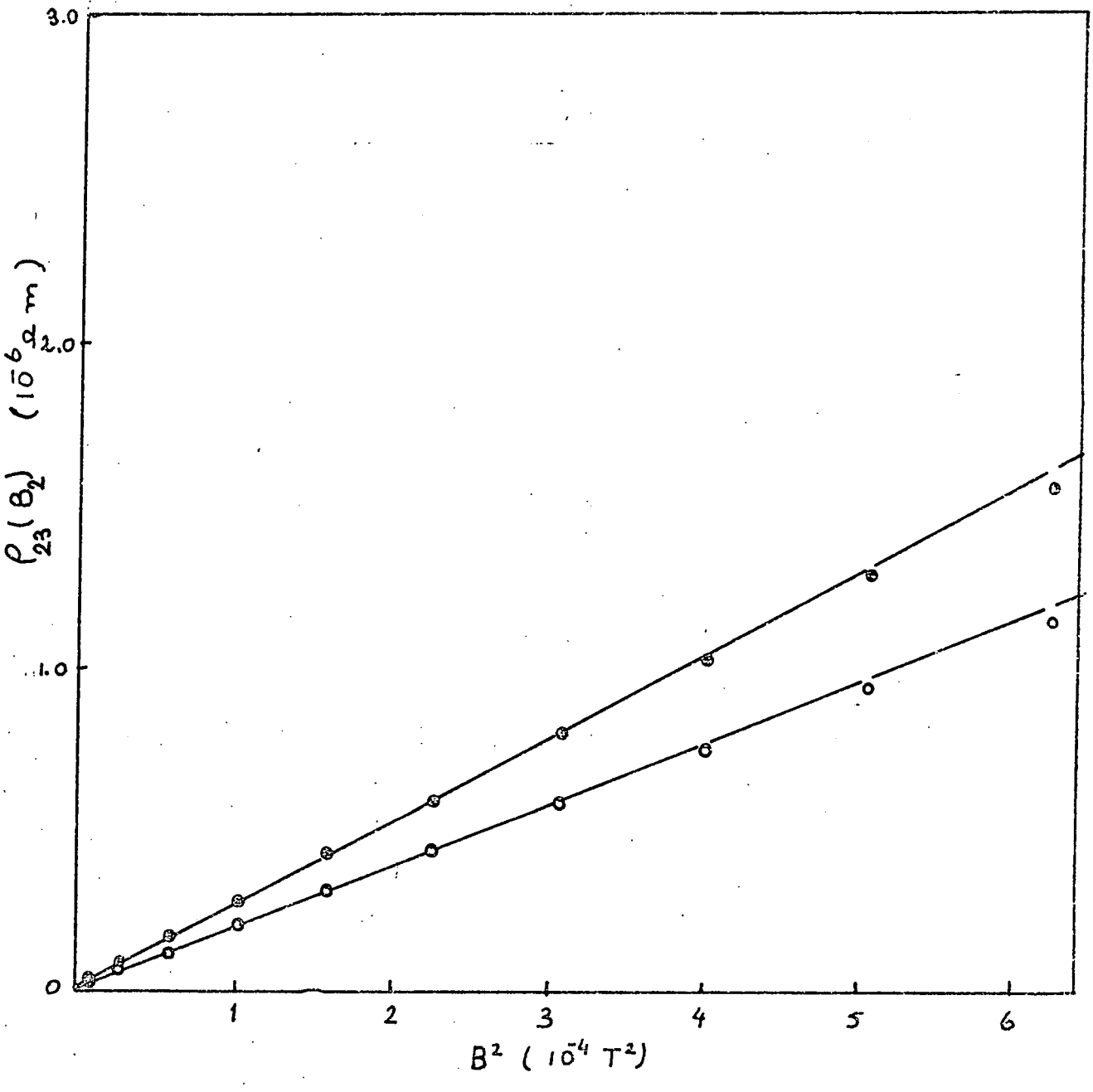

$-A_{41}$

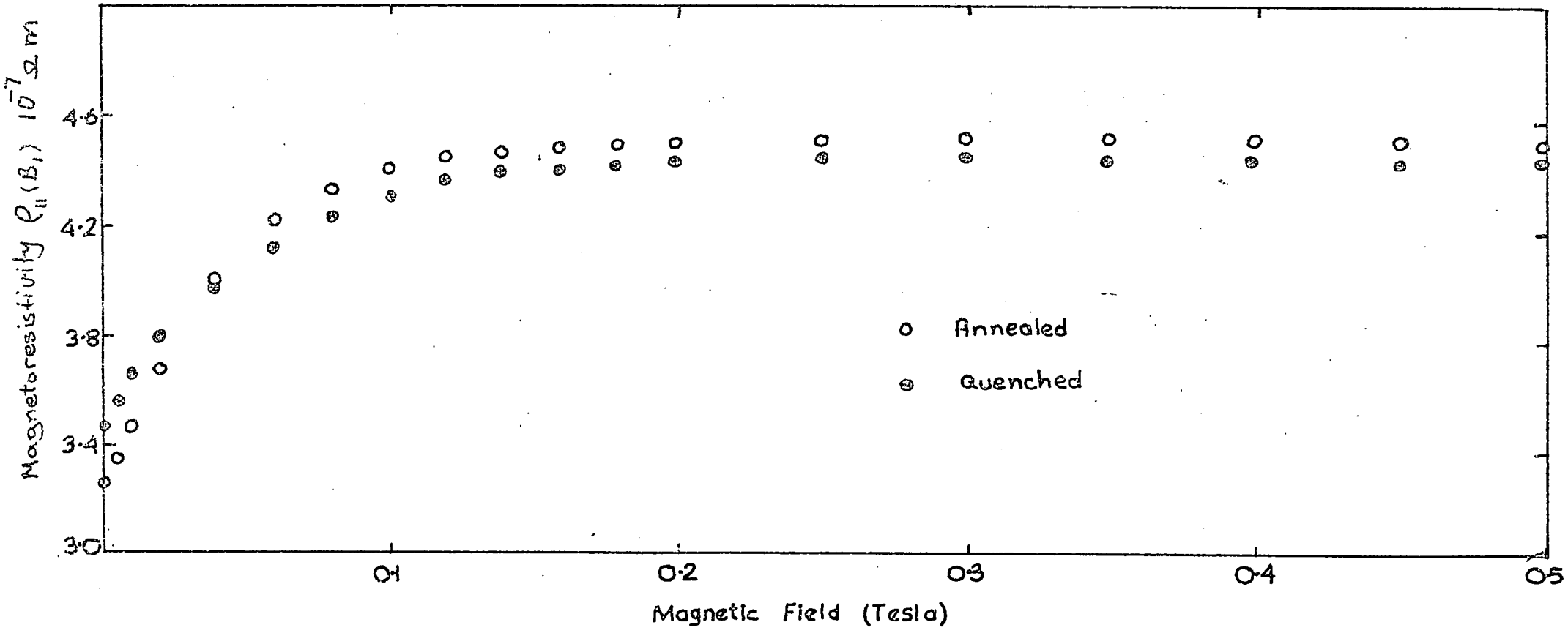

Figure (5-11) : Magnetoresistivity measurements for $\rho_{11}(B_1)$ at intermediate magnetic fields (77°K)

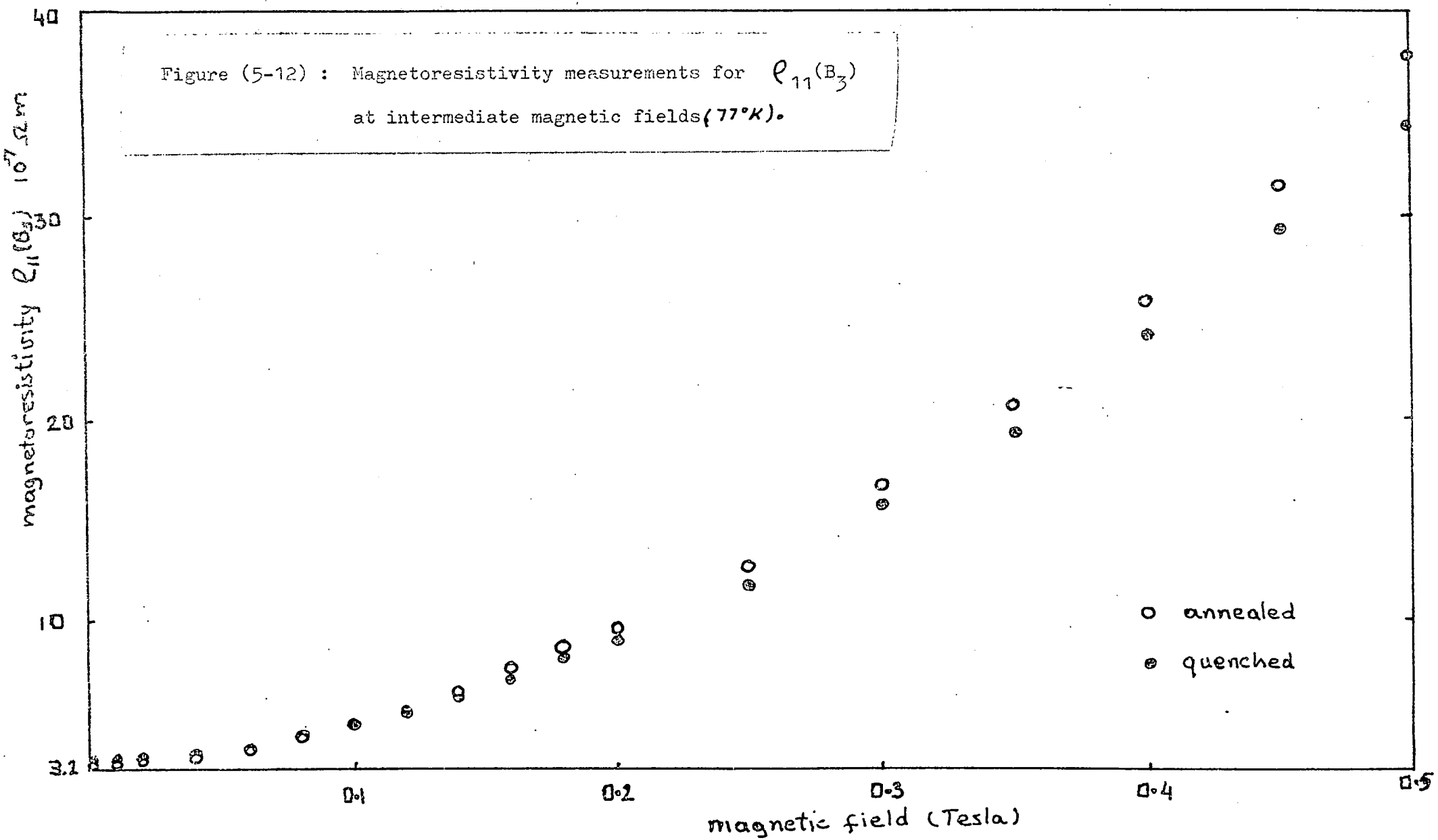

Figure (5-12) : Magnetoresistivity measurements for $\rho_{11}(B_3)$ at intermediate magnetic fields (77°K).

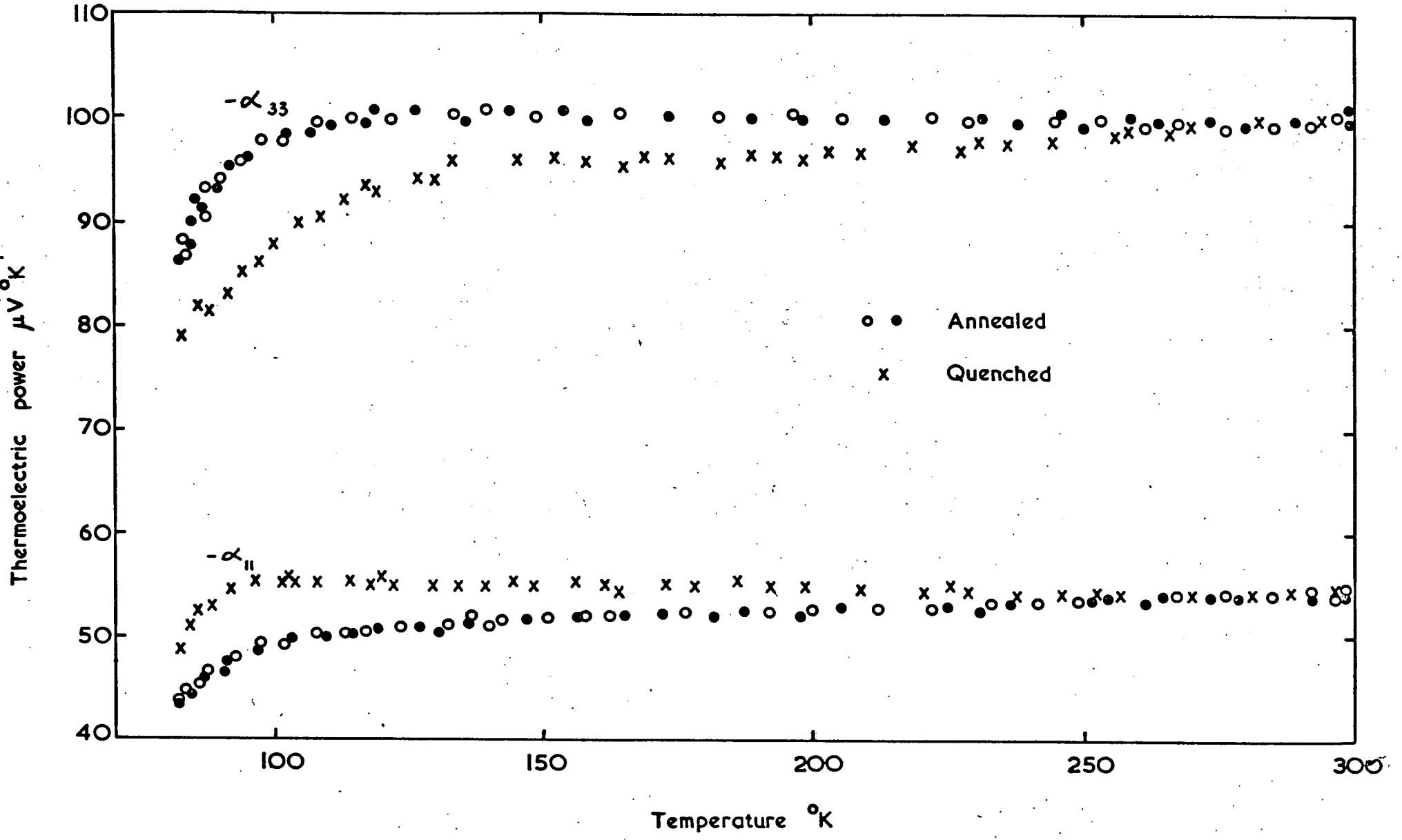

Figure (5-13) : Zero field thermoelectric power coefficients as a function of temperature.

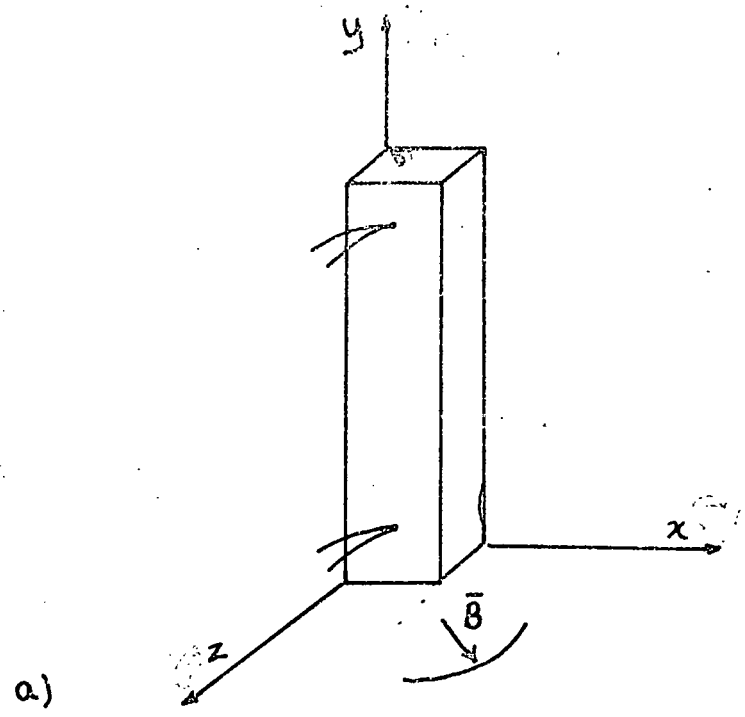

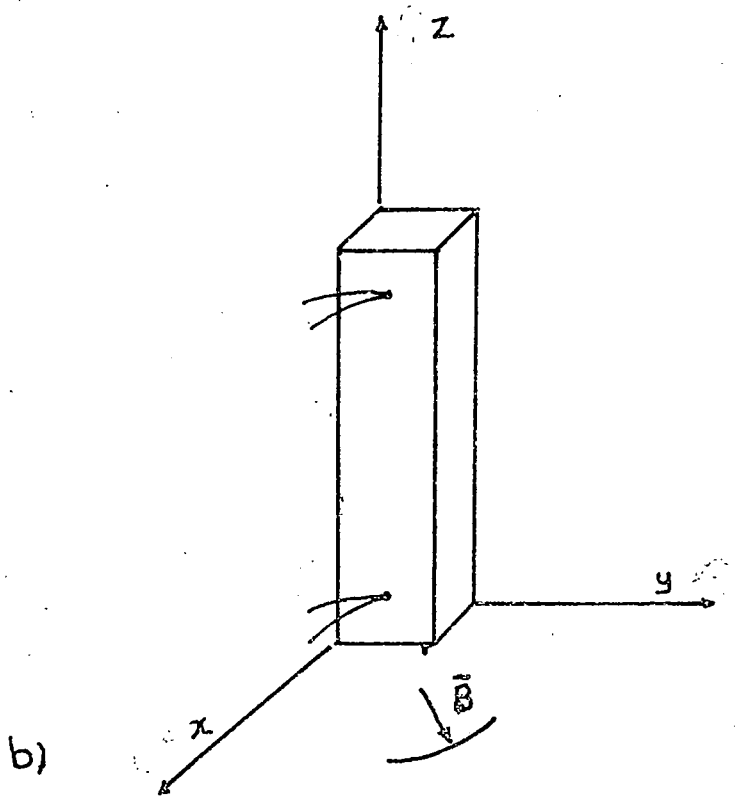

Figure (5-14) : The sample configurations used for the thermomagnetic power measurements.

a) y-axis sample b) z-axis sample.

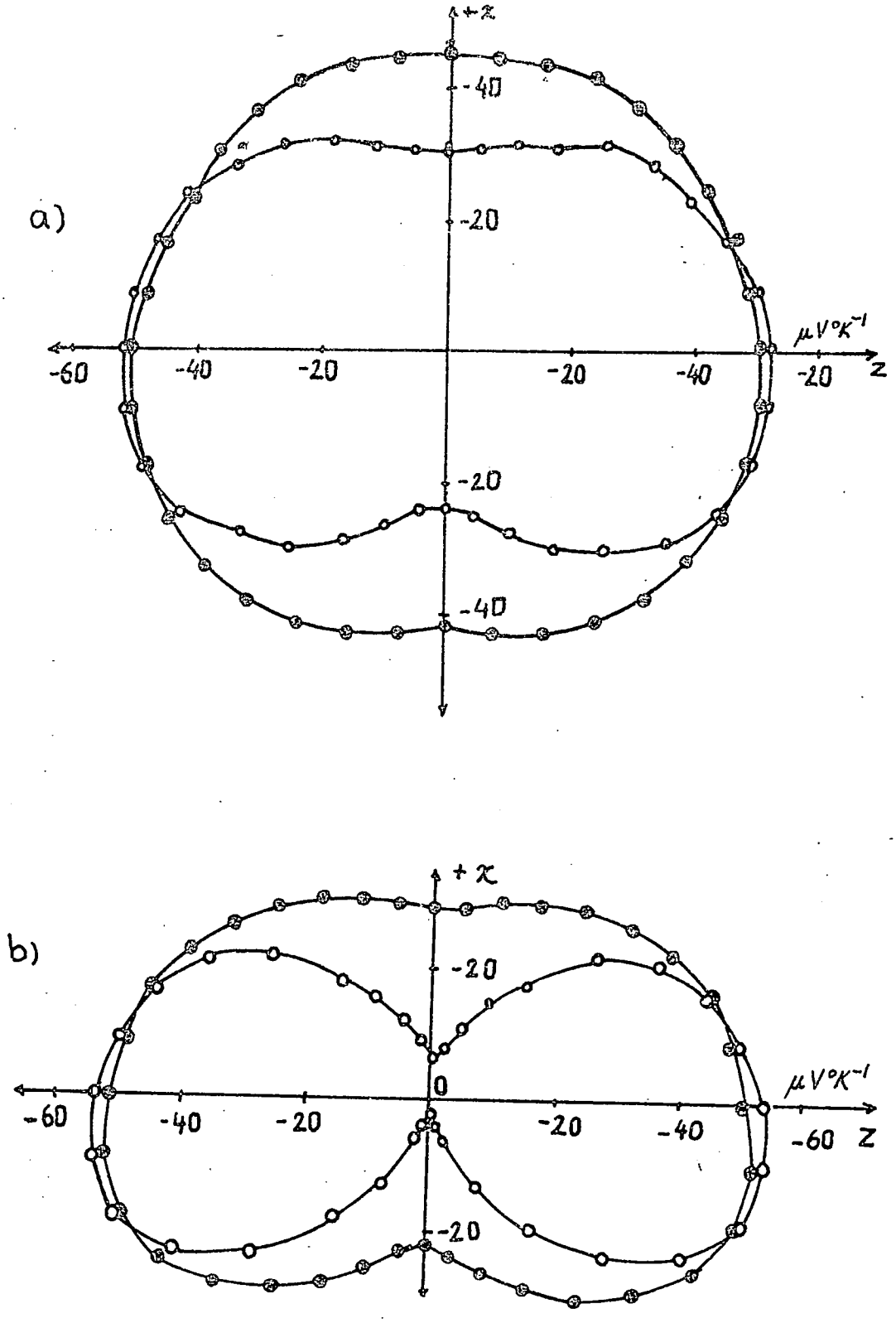

Figure (5-15) : The polar thermomagnetic power data for $\alpha_{22}(\bar{B})$ at 77°K, a) B_o = 0.05 T b) B_o = 0.075 T. Open circles correspond to measurements on annealed samples.

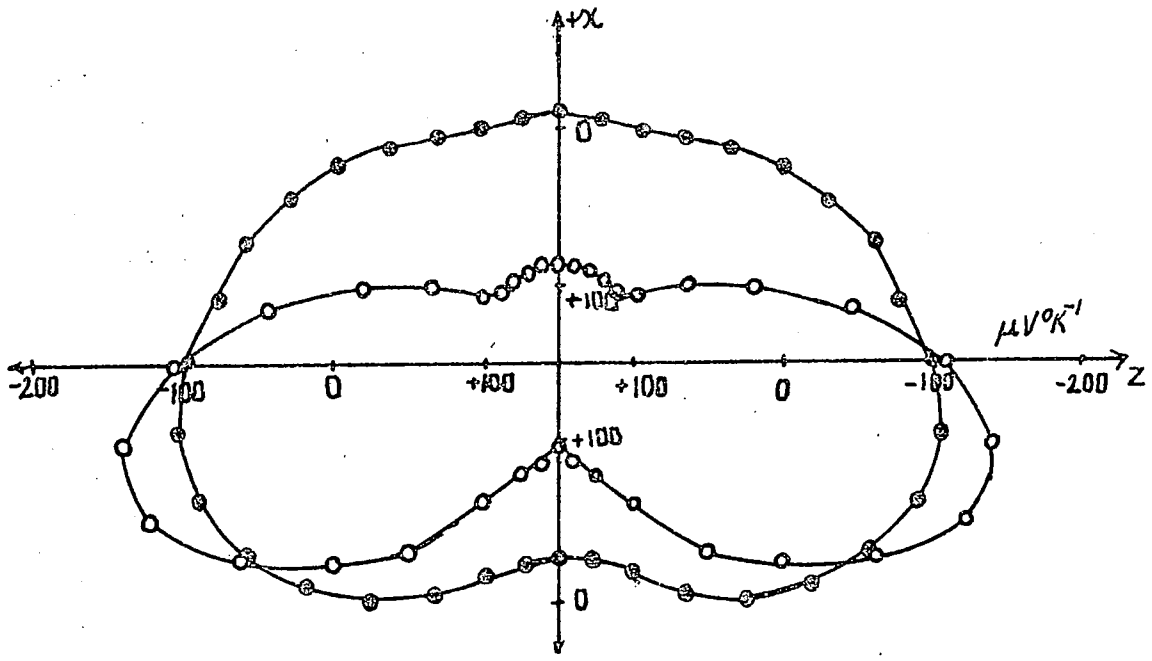

Figure (5-16) : The polar thermomagnetic power data for $\alpha_{22}(\bar{B})$ at 77°K, B_o = 0.38 T. Open circles correspon to measurements on annealed samples.

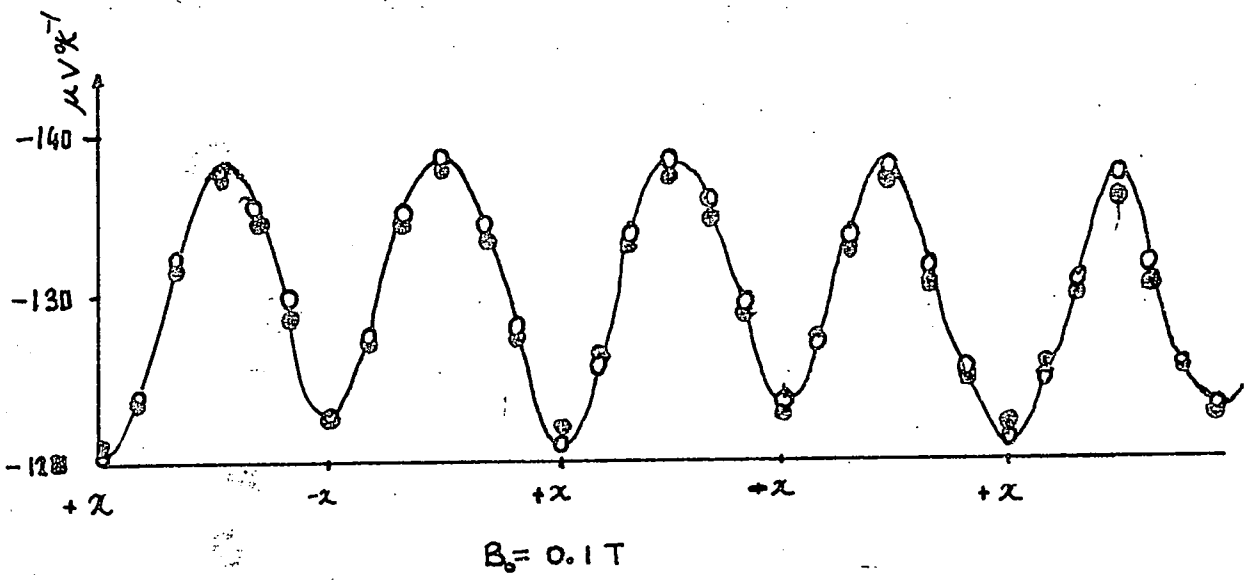

Figure (5-17) : The thermomagnetic power data for z-sample in xy plane, at 77°K, B_o = 0.1 T.

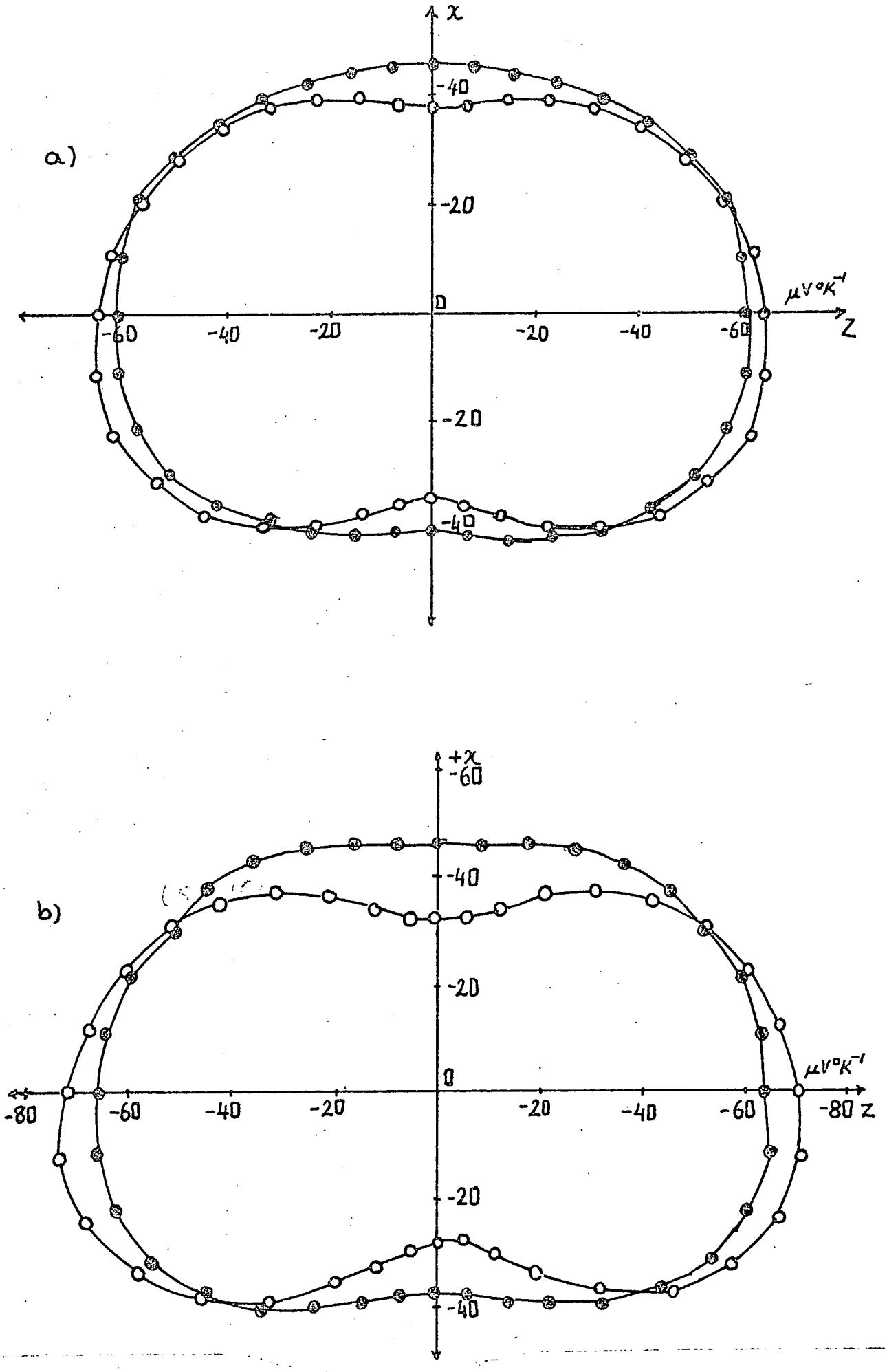

Figure (5-18) : The polar thermomagnetic power data for $\alpha_{22}(B)$ at 196°K, a) B_o = 0.4 T b) B_o = 0.5 T. Open circles correspond to measurements on annealed samples.

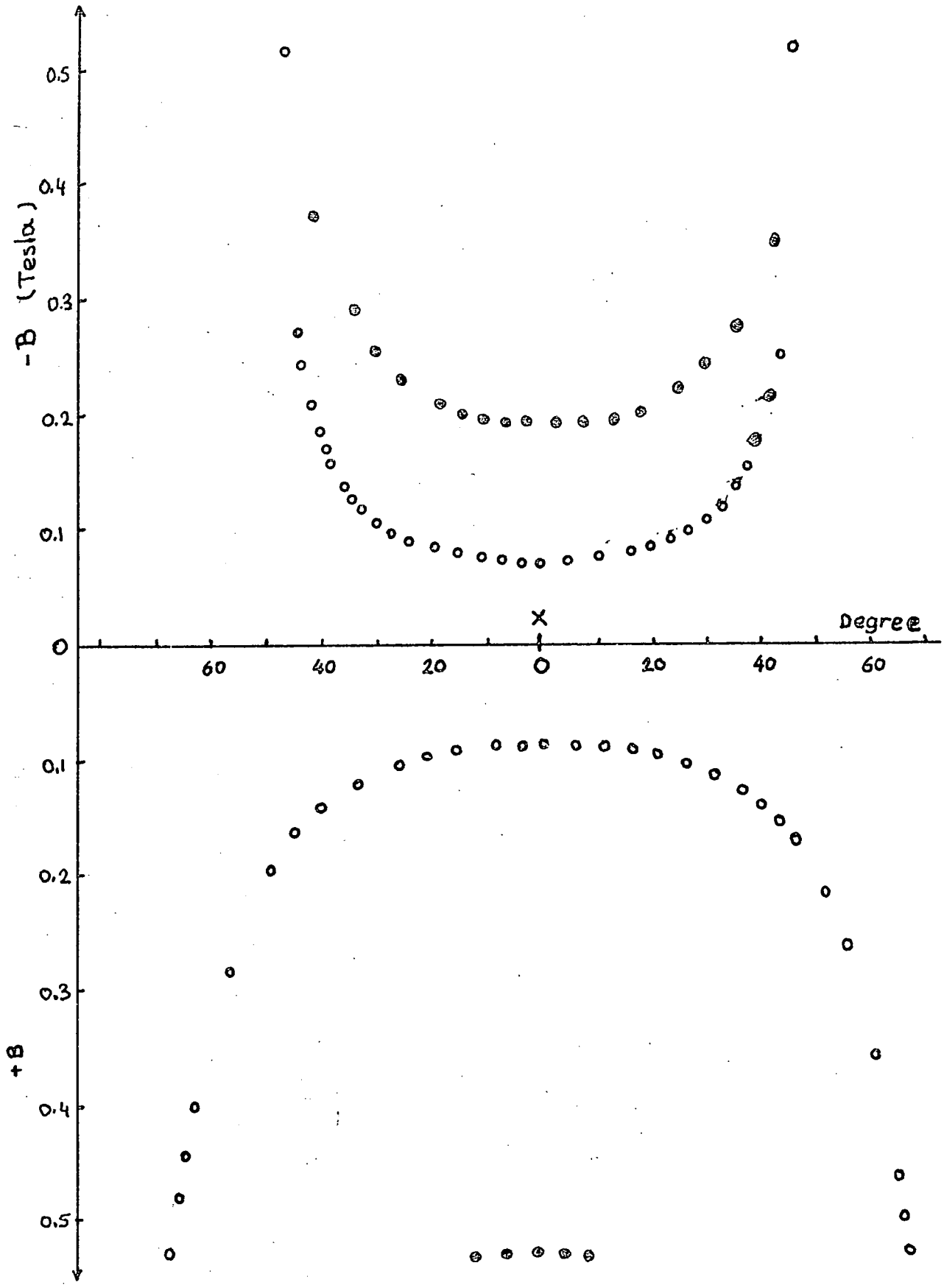

Figure (5-19) : The relation between the magnitude and the direction of the magnetic field vector in the xz plane at 77°K, corresponding to a zero thermoelectric voltage. Open circles denote the measurements on annealed samples.

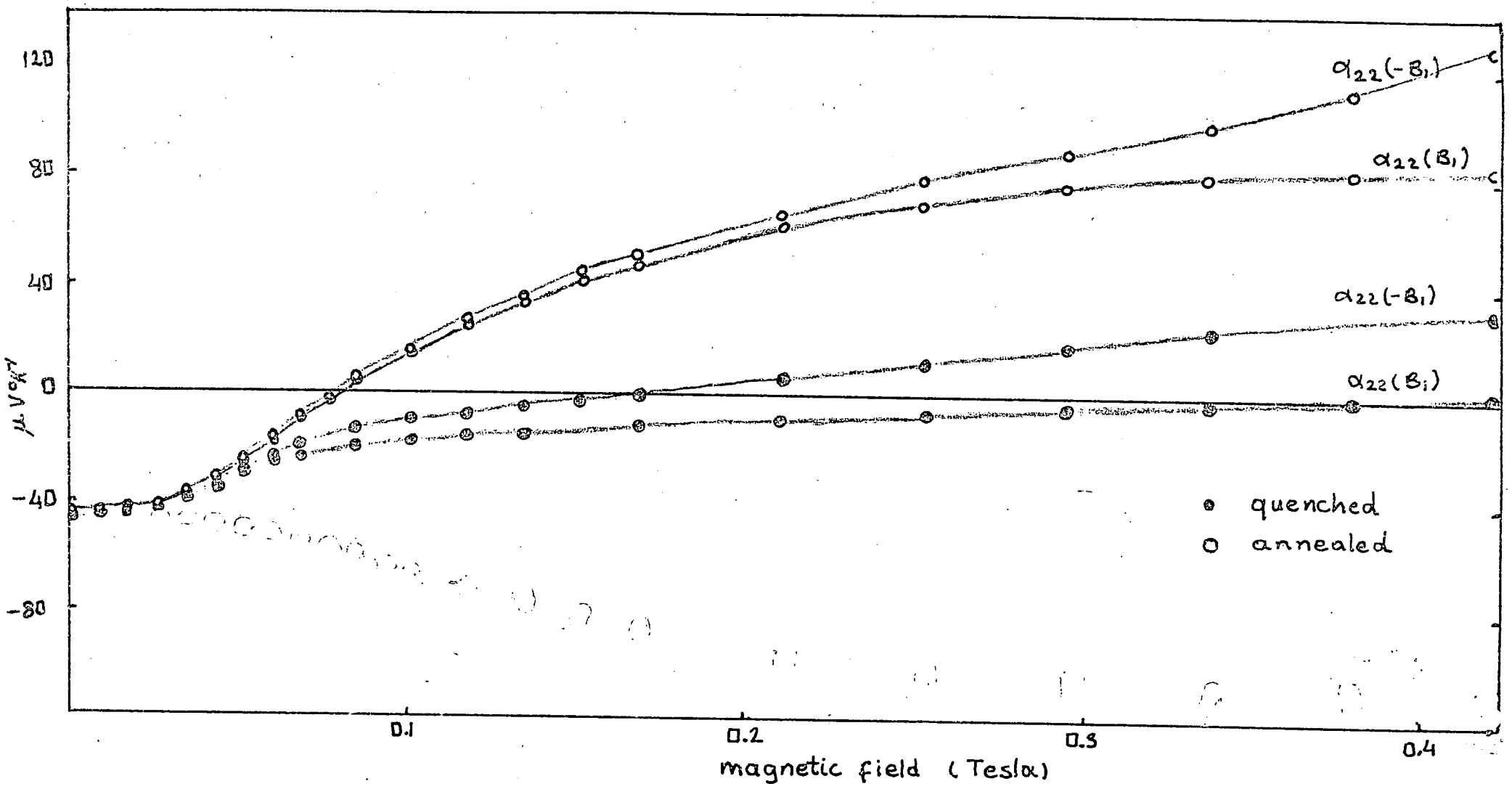

Figure (5-20) : The variation of $\alpha_{22}(\pm B_1)$ with the magnetic field at 77°K. Open circles correspond to measurements on annealed samples.

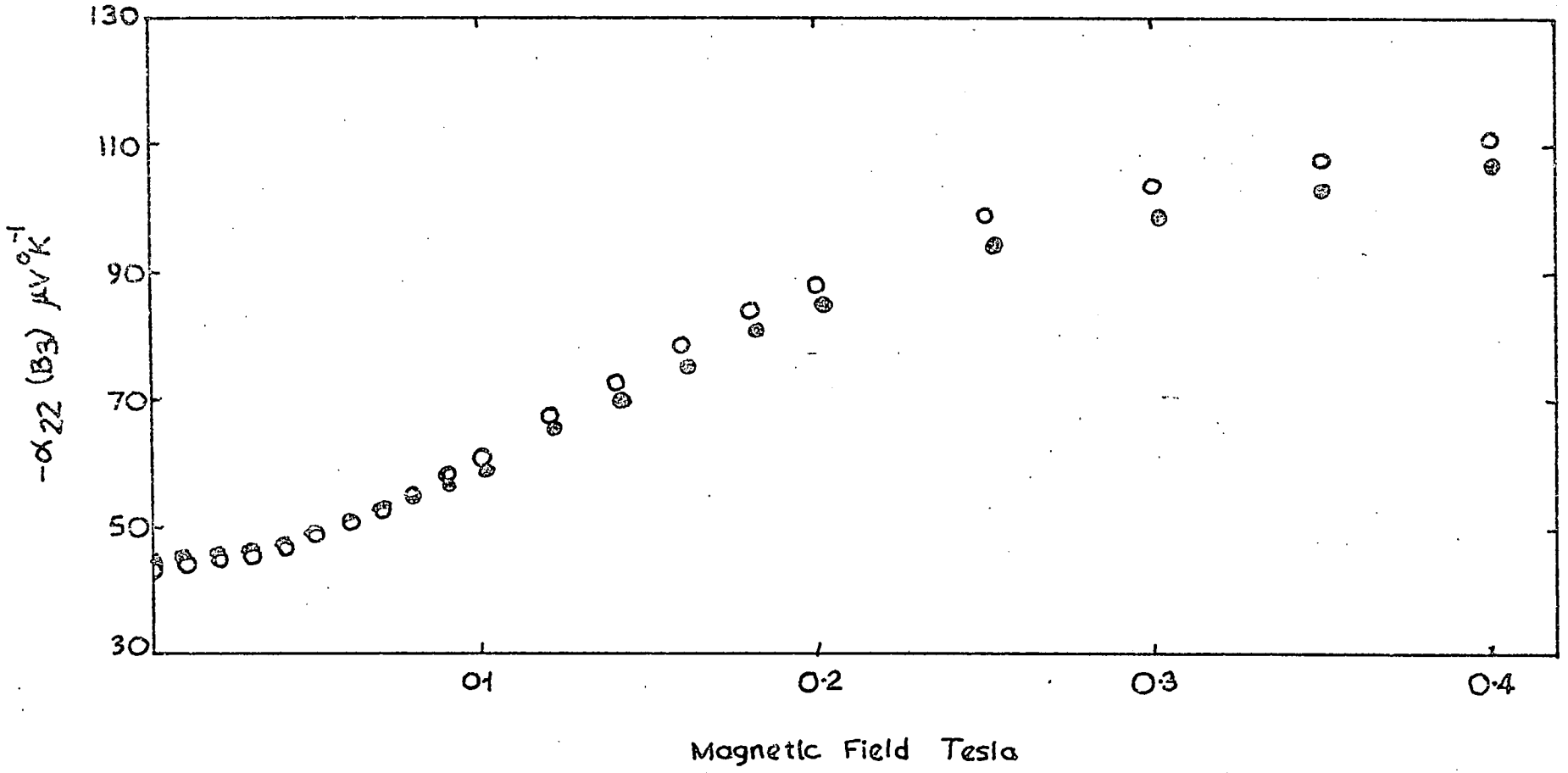

Figure (5-21) : The variation of $\alpha_{22}(B_3)$ with the magnetic field at 77°K. Open circles correspond to measurements on annealed samples.

CHAPTER VI

THE COMPUTATION AND DISCUSSION OF MODEL PARAMETERS

I - INTRODUCTION

The experimental results presented in Chapter V for both the galvanomagnetic and thermomagnetic effects in the annealed and quenched sample conditions can now be quantitatively discussed on the basis of the Fermi surface model presented in Chapter II for bismuth. In Chapter III, the theoretical expressions at low and intermediate fields have been formulated in terms of charge carrier densities and mobilities. A comparison between the theory and the experimental data requires a fit to the equations involved in terms of the eight band parameters μ_1, μ_2, μ_3, μ_4, ν_1, ν_3, N, P for bismuth. The determination of these parameters provide basic information on the carrier transport properties of bismuth and on the effects of quenching on them. The procedures leading to the evaluation of these eight parameters from the galvanomagnetic data are now detailed.

II - METHOD OF COMPUTATION

Determination of the model parameters from the measured data is a difficult task. The equations relating these parameters to the measured data are complex. A direct solution by the elimination of the unknown is not only impractical but also the adoption of such a procedure would magnify the experimental errors, because the measured

coefficients would then become involved in equations in high order powers. Also since the model itself can only be an approximation an exact solution cannot exist. One approach would be to take trial values for the model parameters, substitute them into the equations and try to improve the parameters by comparing the calculated values for the equations with the corresponding measured values. Of course this procedure cannot be based on arbitrary trial and error; adoption of a computational method is necessary. This approach has the added advantage that the number of measured coefficients usually exceeds the number of unknown. It is usual to use a generalized least-mean-squares fit of the measurements to the predictions of the equations (Jeavons and Saunders 1969), Hartman 1969), where the minimization of a function defined by

$$SUM = \sum_J \left[W_J \left(1 - \frac{CAL(J)}{CO(J)}\right)\right]^2 \qquad (6\text{-}1)$$

is required using the variable metric method of Davidon (1959). On substitution of arbitrary values for the eight unknown, a calculated value (CAL(J)) for a particular equation J in the set is obtained; CO(J) is the corresponding measured value. W_J is a weight factor used to put more emphasis on the most accurately measured coefficients, to avoid masking by contributions of the small and less precisely determined ones. To perform this computation, a Fortran IV programme has been devised: the variables μ_1, μ_2, μ_3, μ_4, ν_1, ν_3, N and ζ (the hole to electron carrier density ratio P/N) are scanned independently, and each time the numerical values of the equations are evaluated and then through equation (6-1) the

best least-mean-squares fit to the measured data is assessed. This also provides a 'feed-back' control for the values over which the variables mustbe swept for the minimization of the term SUM in equation (6-1). The result is a steady progress towards the best approximation. The starting trial solutions in principle could take any value, provided that appropriate sweep steps are chosen and a sufficiently large number of cycles is allowed. At the start of the solution procedure, arbitrary values have been assigned for each model parameter. Checks have shown that, whatever the initial points are, the final solutions are unchanged. The computing programmes used for the assessment of the model parameters from the galvanomagnetic and thermomagnetic data have essentially the same structure. They are reproduced in the appendix.

III - SOLUTIONS FOR THE GALVANOMAGNETIC DATA

A - Low Field Magnetoresistivity

A representative set of the low field, galvanomagnetic tensor components from table (5-1) has been taken (see table 6-1) to evaluate the band parameters in the annealed and quenched sample conditions.

The calculated model parameters for quenched and annealed bismuth at 77°K and at room temperature are listed in table (6-2). These results present for the first time the effect of quenched-in defects on the components of the mobility tensors $\hat{\mu}$ and $\hat{\nu}$ and on the carrier densities in each band. For direct comparison with other Fermi surface parameters, it is often convenient to know the components (μ_1^*, μ_2^*, μ_3^*) of the diagonalized tensor; these

TABLE (6-1) : Representative set of magnetoresistivity tensor coefficients of bismuth used in the computations

Sample Condition	Low Field magnetoresistivity tensor coefficients											
	ρ_{11}	ρ_{33}	$\rho_{12,3}$	$\rho_{23,1}$	A_{11}	A_{12}	A_{13}	A_{31}	A_{33}	A_{14}	A_{41}	A_{44}
Annealed ($77^{\circ}K$)	0.321	0.344	-0.20	10.5	138	173	32.5	152	12.0	34.0	19.3	-19.0
Quenched ($77^{\circ}K$)	0.348	0.337	-0.14	8.8	142	155	26.5	130	9.2	36.0	23.0	-14.3
Annealed or Quenched ($293^{\circ}K$)	1.17	1.38	-0.05	0.162	0.92	1.90	0.24	2.71	0.09	0.27	0.19	-0.14
Units	$10^{-6}\ \Omega\ m$		$10^{-6}\ \Omega\ m\ T^{-1}$		$10^{-6}\ \Omega\ m\ T^{-2}$							

TABLE (6-2) : Solutions for the model parameters obtained from the low field magnetoresistivity data

Sample Condition	Electron mobilities ($m^2\ V^{-1}\ sec^{-1}$) μ_1	μ_2	μ_3	μ_4	Electron tilt angle (Degrees) θ	Electron density ($10^{23} m^{-3}$) N	Hole mobilities ($m^2\ V^{-1}\ sec^{-1}$) ν_1	ν_3	Hole density ($10^{23} m^{-3}$) P
Annealed (77^oK)	68	1.6	38	-4.3	$+ 6.9^o$	4.4	12	2.1	4.4
Quenched (77^oK)	59	1.4	40	-4.6	$+ 6.7^o$	4.6	9.0	2.7	5.3
300^oK	3.5	0.06	1.4	-0.19	$+ 7.9^o$	24.0	0.58	0.45	24.0

Electron mobilities in principle axis system ($m^2\ V^{-1}\ sec^{-1}$)	μ_1^*	μ_2^*	μ_3^*
Annealed (77^oK)	68	1.1	38.5
Quenched (77^oK)	59	0.85	40.5

mobilities along the ellipsoidal principal axes are also given in table (6-2).

Some physical insight into the effects of quenching can be gained by considering the magnetoconductivity; the separate contributions of the electrons and holes to each coefficient of the magnetoconductivity tensor $\hat{\sigma}(\bar{B})$ at 77°K have been calculated from the model parameters in table (6-2) and are listed in table (6-3). Although quenching greatly increases the hole density, the much more mobile electrons still dominate the carrier transport properties in the quenched crystals. In the coefficients S_{11}, S_{33}, S_{41} holes play no part because they are sited in an ellipsoid of revolution about the z-axis. Furthermore, the hole contribution in S_{31} is directly proportional to the square of the very small component ν_3 and is negligible.

Carrier mobilities are somewhat lower in the xy plane in the quenched state than in the annealed condition; the quenched-in defects play a significant role in the carrier scattering. The z-axis mobilities μ_3 and ν_3 have been increased slightly by quenching; this anomalous behaviour is a direct reflection of the experimental observation that ρ_{33} is reduced by a small amount (-3 %) after quenching; the z-axis conductivity

$$\sigma_{33} = 1/\rho_{33} = Ne\ \mu_3 + Pe\ \nu_3 \qquad (6\text{-}2)$$

is almost completely dominated by the electron contribution (see table 6-3) and both the electron density N and the mobility tensor

TABLE (6-3) : Contributions made by holes and electrons to each magnetoconductivity tensor coefficient in annealed and quenched bismuth

Tensor Coefficient	Annealed condition			Quenched condition			Magnetoresistivity Ratios	
	Electron Contribution	%	Hole Contribution	Electron Contribution	%	Hole Contribution	Annealed	Quenched
σ^{o}_{11}	2.45×10^{8}	74.5	0.84×10^{8}	2.22×10^{8}	73.5	0.80×10^{8}	0.95	0.96
σ^{o}_{33}	2.68×10^{8}	95.0	0.14×10^{8}	2.94×10^{8}	92.4	0.24×10^{8}	1.02	0.98
$\sigma_{12,3}$	0.76×10^{7}	42.9	-1.01×10^{7}	0.60×10^{7}	45.8	-0.71×10^{7}	1.02	1.02
$\sigma_{23,1}$	9.24×10^{7}	98.2	-0.17×10^{7}	8.81×10^{7}	97.7	-0.21×10^{7}	0.92	1.10
S_{11}	153×10^{7}	100	0	128×10^{7}	100	0	1.03	1.01
S_{12}	470×10^{7}	99.6	2.0×10^{7}	389×10^{7}	99.7	1.0×10^{7}	1.01	1.00
S_{13}	26.7×10^{7}	68.8	12.1×10^{7}	18.4×10^{7}	74.2	6.4×10^{7}	1.07	1.06
S_{31}	351×10^{7}	99.7	1.0×10^{7}	353×10^{7}	100	0	0.83	0.82
S_{33}	8.85×10^{7}	100	0	9.2×10^{7}	100	0	0.97	1.08
S_{14}	34.2×10^{7}	100	0	28.8×10^{7}	100	0	0.96	0.89
S_{41}	19.2×10^{7}	100	0	19.7×10^{7}	100	0	1.09	0.94
S_{44}	-7.3×10^{7}	86.9	-1.10×10^{7}	-6.1×10^{7}	86.3	-0.97×10^{7}	1.04	1.09

component μ_3 are increased by quenching. Furthermore, on quenching both the electrons and holes have increased in number and also the equality between their densities has been destroyed in favour of the hole population. The quality of fit as estimated from SUM is about the same for the annealed (0.2072) and quenched (0.1925) conditions. For the individual tensor coefficients the fit, assessed by the ratios between the calculated and the measured coefficients, is in general excellent (see table 6-3).

B - Magnetoresistivity Data at Intermediate Fields

For the intermediate fields, the measured data (see figure 5-11,12) have been used in conjunction with the magnetoconductivity expressions (3-31) and (3-32). In principle the solutions for the complete set of model parameters can be obtained from the data points for each magnetoresistivity components for $\rho_{11}(B_1)$, and $\rho_{11}(B_3)$ alone. The success and the reliability of such a solution then mainly depends on the variation of magnetoresistivity as a function of magnetic field. If this variation is sufficiently large and sensitive to small trial changes in each model parameter, such a solution can be useful. Here the data for magnetoresistivity components $\rho_{11}(B_1)$ and $\rho_{11}(B_3)$ have been utilized. The computations have been based on 19 of the data points measured as a function of magnetic field. The expressions relating $\rho_{11}(B_1)$ and $\rho_{11}(B_3)$ to the magnetoconductivity components can be obtained through the inversion of $\hat{\sigma}(\bar{B})$ and they are

$$\rho_{11}(B_1) = 1 \,/\, \sigma_{11}(B_1)$$

(6-3)

$$\rho_{11}(B_3) = \left(\sigma_{22}(B_3) / \left(\sigma_{11}(B_3)\, \sigma_{22}(B_3) - \sigma_{12}(B_3)\, \sigma_{21}(B_3) \right) \right)$$

The magnetoconductivity terms involved in equation (6-3) are given by

$$\sigma_{11}(B_1) = ne\mu_1 + \frac{ne}{2}(\mu_1 + 3\mu_2 + 4dB_1^2)\left(1 + \tfrac{1}{4}\left(3\mu_1\mu_3 + \frac{d}{\mu_1}\right)B_1^2\right)^{-1}$$

$$+ Pe\ \nu_1 \qquad (6\text{-}4)$$

$$\sigma_{11}(B_3) = \sigma_{22}(B_3) = \frac{3ne}{2}(\mu_1 + \mu_2)(1 + \mu_1\mu_2 B_3^2)^{-1} + Pe\ \nu_1(1 + \nu_1^2 B_3^2)^{-1}$$

$$\sigma_{12}(B_3) = \sigma_{21}(-B_3) = -3ne\mu_1\mu_2(1 + \mu_1\mu_2 B_3^2)^{-1} B_3 + Pe\ \nu_1^2(1 + \nu_1^2 B_3^2) B_3$$

where d is the determinant of the electron mobility tensor and N(=3n), P are the electron and hole carrier densities. The model parameters evaluated through a least-mean-squares fit method are listed in table (6-4). The agreement between the measured and the calculated data is illustrated in figures (6-1) and (6-2).

The solutions obtained from the intermediate magnetoresistivity data serve two purposes: to test the applicability of the magnetoconductivity expressions at higher megnetic fields in bismuth, to assess the quenching induced changes on the model parameters.

The agreement between the theory and the experiment is excellent. Magnetoresistivity solutions at intermediate fields are consistent with the low field solutions for both the annealed and quenched sample conditions. The quenching induced changes on the

TABLE (6-4) : Solutions obtained from magnetoresistivity measurements at intermediate magnetic fields

Sample Condition	$\rho_{ij}(\bar{B})$	Electron mobilities ($m^2\ V^{-1}\ sec^{-1}$) μ_1	μ_2	μ_3	μ_4	Electron tilt angle (Degrees) θ	Hole mobilities ($m^2\ V^{-1}\ sec^{-1}$) ν_1	ν_3	Carrier densities ($10^{23}\ m^{-3}$) N	P
Annealed	$\rho_{11}(B_1)$	64	0.1	36	-4.2	6.35	12	2.6	4.2	4.2
Quenched	$\rho_{11}(B_1)$	59	0.4	37	-4.3	6.35	12	2.5	4.4	5.2
Annealed	$\rho_{11}(B_3)$	62	0.5	38	-4.3	6.43	13.6	1.3	4.3	4.3
Quenched	$\rho_{11}(B_3)$	56	0.5	39	-4.3	6.25	12	1.8	4.4	5.2

model parameters obtained by both methods are in reasonable agreement; the mobility components in the xy-plane are reduced while those along the z-axis slightly increased; quenching results in creation of an excess number of holes. However the intermediate field solution predicts slightly lower carrier densities than the low field data, but the prediction of increased carrier densities for both electrons and holes is consistent. Thus on the basis of magnetoresistivity data, the result of the introduction of the defects is to distort the band edges in such a way as to increase the band overlap. A quantitative assessment of the shifts in the Fermi levels can be obtained directly from the expressions for the density of carriers in a valley containing r ellipsoids. For the conduction band

$$(N/r_e = (4\pi/h^3)(2m_o kT)^{3/2}(m_e^*)^{3/2} F_{\frac{1}{2}}(\eta_e) \qquad (6\text{-}5)$$

where m_e^* (in units of m_o) is the density of states effective mass. A similar expression obtains for the valence band. The density of states effective mass at 77°K can be considered to be unchanged from the liquid helium values, an assumption that has proved successful for antimony (Saunders and Öktü 1968); the electron value of m_e^* is taken from Aubrey (1961) as 0.042 and that for holes m_h^* as 0.115 from Brandt (1960). The Fermi levels in the electron and hole bands and the band overlap in bismuth at 77°K before and after quenching are given in table (6-5). The band overlap is increased by 13 % on quenching. The increase (27 %) in energy separation between the Fermi level and the valence band edge is much larger than that (3 %) for the conduction band; this reflects the finding that after quenching the hole concentration has increased $4\frac{1}{2}$ times more than

that of the electrons (table 6-2) and shows that the hole ellipsoid expands much more than to the three electron pockets. The basic tendency of the quenched-in defects is to affect the Fermi surface as if they were electron traps. A parallel can be drawn with graphite in which excess holes are created by both electron and neutron irradiation damage (Blackman, Saunders and Ubbelohde 1961, Corbett 1966, Saunders 1970).

The Seebeck coefficient data provide further confirmation of the nature of the changes at the band edge following quenching. The Seebeck tensor components α_{11} and α_{33} are related to the isotropic partial Seebeck coefficients (P_e and P_h) by equation (3-37b). These quantities can be written in terms of the carrier mobilities and densities as

$$P_h = \frac{\alpha_{11}\mu_3(\mu_1+\mu_2+2c\nu_1) - \alpha_{33}(\mu_1+\mu_2)(\mu_3+c\nu_3)}{c(2\nu_1\mu_3 - \nu_3(\mu_1+\mu_2))}$$

$$P_e = \frac{\alpha_{11}\nu_3(\mu_1+\mu_2+2c\nu_1) - 2\alpha_{33}\nu_1(\mu_3+c\nu_3)}{\nu_3(\mu_1+\mu_2) - 2\nu_1\mu_3} \qquad (6\text{-}6)$$

where c, the ratio of the hole to electron densities, is 1.0 in annealed and 1.2 in quenched bismuth. Use of mobilities from table (6-2), shows that quenching has caused P_e to reduce from -97 $\mu V/^{\circ}K$ to -91 $\mu V/^{\circ}K$ and P_h from +114 $\mu V/^{\circ}K$ to 95 $\mu V/^{\circ}K$ at liquid nitrogen temperatures. These partial Seebeck coefficients have been used to calculate the electron and hole Fermi energies on the restrictive assumption of acoustic mode, intravalley scattering ($S = -\frac{1}{2}$) from

TABLE (6-5) : The Fermi level separation from the conduction and valence band edges and the band overlap in annealed and quenched bismuth

Sample condition	Fermi enrgy (eV)				Band overlap $-E_o$ (eV)	
	Conduction band (E_F^e)		Valence band (E_F^h)			
	Galvano-magnetic effect	Thermo-electric power	Galvano-magnetic effects	Thermo-electric power	Galvano-magnetic effects	Thermo-electric power
Annealed	0.0205	0.017 $\pm$ 0.002	0.0138	0.013 $\pm$ 0.002	0.0343	0.030 $\pm$ 0.004
Quenched	0.0212	0.019 $\pm$ 0.002	0.0175	0.018 $\pm$ 0.002	0.0387	0.036 $\pm$ 0.004

(Gallo et al 1962, Saunders and Öktü 1968)

$$Pe = -\frac{k}{e}\left[\frac{(5/2+s)\,F_{3/2+s}(\eta_e)}{(3/2+s)\,F_{\frac{1}{2}+s}(\eta_e)} - \eta_e\right]$$

$$P_h = \frac{k}{e}\left[\frac{(5/2+s)\,F_{3/2+s}(\eta_h)}{(3/2+s)\,F_{\frac{1}{2}+s}(\eta_h)} - \eta_h\right] \qquad (6\text{-}7)$$

where $\eta_{e,h}$ are the partial, reduced Fermi energies of electron and holes. The Fermi levels and band overlap calculated by this method are given in table (6-5); although they have a substantially wider margin of error than those calculated by the other method they do serve to confirm the basic findings from low and intermediate field magnetoresistivity data. As a result of quenching in bismuth, the band overlap is increased; the relative energies of the Fermi level with respect to both band edges increase, that in the valence band markedly: the quenched-in defects show predomiantly acceptor-like character.

IV - APPLICATION TO THE THERMOMAGNETIC DATA

For the thermomagnetic power data the programme was extended so as to facilitate the solutions of the band parameters from linear and polar magnetothermoelectric polar plots for $\alpha_{22}(\bar{B})$. The variation of the thermomagnetic power data as a function of magnetic field is not as large as the magnetoresistivity data. The quenching effects on the thermomagnetic properties of bismuth are dramatic (see figures 5- 15, 16) and the general tendency is towards the

reduction of magnetic field effects and angular anisotropy in $\alpha_{22}(\bar{B})$ in xz-plane. For this reason, quenched magnetothermoelectric power polar data do not allow quantitative assessment of the quenching induced changes on the model parameters. The only data set in the quenched condition which can be analysed quantitatively is that for $\alpha_{22}(B_3)$, and the determination of a set of model parameters based on this data will be presented. The data obtained from the z-axis sample (see figure 5-17) in both sample conditions is again not analysable, because not only are the magnetic field effects much smaller but also the main features of the angular change in magnetothermoelectric power data in the xy-plane are completed in about 30° angular sections of the plane. However, for the y-axis sample in the annealed state both the linear and polar data show sufficiently large field or angular dependent variations for analysis to be possible. Least-mean-squares procedure solutions based on these data have been obtained for both $\alpha_{22}(\bar{B})$ polar plots and $\alpha_{22}(+B_1)$ and $\alpha_{22}(B_3)$. The extraordinary changes in $\alpha_{22}(\bar{B})$ in the xz-plane show both the sign reversal in magnetothermoelectric power and the characteristic features of the Umkehr effect. A fit to this data in terms of the model parameters is a most valuable test for the validity of the theory developed for the thermomagnetic effects and of the adopted Fermi surface model. For this purpose two of the polar data sets have been utilized: one for a magnetic field (0.075 T) just less than that required for observation of sign reversal for any orientation in the xz-plane, the other large enough (0.38 T) so that sign reversal is manifested over a large angular region in that plane. The solutions were also extended to the polar

plots obtained at 0.68 T by Michenaud et al (1970) and at 1.00 T by Smith et al (1964): it is pertinent to test the theory with these classic results, as well as with our own. The shapes of these polar diagrams are very sensitive to the direction, sense and magnitude of the applied magnetic fields.

For the component $\alpha_{22}(B_1, 0, B_3)$ of the thermomagnetic tensor we have from equation (3-37)

$$\alpha_{22}(\bar{B}) = \rho^{t}_{21}(\bar{B})\,(P_e\,\sigma^{e}_{12}(\bar{B}) + P_h\,\sigma^{h}_{12}(\bar{B}))$$

$$+ \rho^{t}_{22}(B)\,(P_e\,\sigma^{e}_{22}(\bar{B}) + P_h\,\sigma^{h}_{22}(\bar{B})) \qquad (6\text{-}8)$$

$$+ \rho_{23}(\bar{B})(P_e\,\sigma^{e}_{32}(\bar{B}) + P_h\,\sigma^{h}_{32}(\bar{B}))$$

where the partial magnetoconductivities $\sigma^{e}_{ij}(\bar{B})$ and $\sigma^{h}_{ij}(\bar{B})$ for electrons and holes respectively can be obtained from equations (3-31) and (3-32); the total magnetoresistivities $\rho^{t}_{ij}(\bar{B})$ have been found by inverting $\hat{\sigma}^{t}(\bar{B})$. Then the angular dependence of $\alpha_{22}(\bar{B})$ has been calculated using equation (6-8) by writing the magnetic field in the xz-plane as

$$B_1 = B_o \cos \phi$$

$$B_3 = B_o \sin \phi$$

A set of nine model parameters, corresponding to the multivalley, two carrier, ellipsoidal Fermi surface, is computed, including the components of mobility tensors for electrons $\hat{\mu}$ and holes $\hat{\nu}$ in the

crystallographic frame of reference, two partial thermoelectric powers P_e and P_h and the carrier densities which enter into the magnetothermoelectric power expressions as a ratio $c(= P/N)$.

To obtain the solutions, a similar least-mean-squares procedure has been used to fit the theory to the polar data for $\bar{\alpha}_{22}(\emptyset)$. Computations have been performed at 10^{o} intervals in the xz plane around the y-axis; taking the symmetry into account, this provides an overdetermined set of 19 effective angular data points from which to calculate the 9 unknowns. A theoretical computation of each $\alpha_{22}(\emptyset_J)$ is carried through by inserting an arbitrary set of model parameters into equation (6-8), each calculated value is then divided by the corresponding experimental value of the $\alpha_{22}(\emptyset_J)$ and next used in equation (6-1) to minimize the term SUM.

The same procedures apply for linear data for which $\bar{B}$ is replaced by the appropriate component.

The fits obtained are plotted in figures (6-3), (6-4) and (6-5), to allow direct comparison with the experimental observations of $\alpha_{22}(\bar{B})$; the characteristic shapes of the experimental polar diagrams, including the finer topological details, are reproduced by the theoretically computed curves. The Umkehr effect and the sign reversal have come naturally out of the transport theory with the correct magnitude and the orientation dependences.

The calculated model parameters corresponding to the theoretical fits in figure (6-3) and (6-4), (6-5) are collected in table (6-6) and (6-7). The solutions obtained for band parameters from

TABLE (6-6) : Solutions for the model parameters obtained from linear magnetothermoelectric power data

Sample Condition	$\alpha_{22}(B_k)$	Electron mobilities ($m^2\ V^{-1}\ sec^{-1}$) μ_1	μ_2	μ_3	μ_3	Electron Tilt angle (degrees) θ	Hole mobilities ($m^2\ V^{-1}\ sec^{-1}$) ν_1	ν_3	Carrier density ratio C	Partial T.E. Powers ($\mu V^{o}K^{-1}$) P_e	P_h
Annealed	$\alpha_{22}(B_1)$	48	6.6	32	-2.6	5.68	12.8	3.3	0.97	-190	198
Annealed	$\alpha_{22}(B_3)$	49	1.2	33	-2.5	4.49	10.5	3.5	1.0	-154	237
Quenched	$\alpha_{22}(B_3)$	43	1.0	30	-2.5	5.82	11	3.4	1.0	-180	210

TABLE (6-7) : Solutions for the model parameters obtained from the thermomagnetic power data for $\alpha_{22}(B_1, 0, B_3)$ and also from the low field magnetoresistivity tensor coefficients (annealed).

Magnetic field (Tesla)	Electron mobilities ($m^2 V^{-1} sec^{-1}$)				Electron tilt angle (Degrees)	Hole mobilities ($m^2 V^{-1} sec^{-1}$)		Carrier density ratio	Partial Thermoelectric powers $\mu V {}^{o}K^{-1}$	
B	μ_1	μ_2	μ_3	μ_4	θ	ν_1	ν_3	C	Pe	P_h
0.075	43	30	21	-2.5	7.7	13	8.0	1.0	-130	66
0.38	58	2.9	21	-2.5	9.1	22	2.4	0.97	-180	79
0.68	54	3.3	25	-2.5	6.6	19	1.9	0.99	-240	48
1.00	55	2.8	28	-2.5	5.5	17	3.1	1.0	-200	89
Low field magneto resistivity solutions	68	1.6	38	-4.4	6.9	12	2.1	$N_e = N_h = 4.4 \times 10^{23}\ m^{-3}$		

different sources are in reasonable agreement.

In addition to accounting for the appearance of an Umkehr effect in $\alpha_{22}(\bar{B})$, the theory can also be used to predict which other tensor components and experimental configurations should show this property. It is valuable to set up the procedure prerequisite for this purpose. Each tensor component $\alpha_{ij}(\bar{B})$ can be decomposed into odd and even terms with respect to $\bar{B}$. An Umkehr effect is to be expected only if the particular $\alpha_{ij}(\bar{B})$ under study contains odd terms. Using equation (3-31) and (3-32) the fulfilment or otherwise of this condition can be established. As an example, let us consider those cases in which the magnetic field is directed along the x-axis ($B_1 \neq 0$, $B_2 = B_3 = 0$) while the temperature gradient is established along any of the three major (x, y or z) crystallographic axes and the thermoelectric voltage is measured along the temperature gradient direction. Then

$$\alpha_{ii}^{(odd)}(B_1) = \sum_{k=1,3} \Big[\rho_{ik}^{(even)} \left(P_e \, \sigma_{ki}^{e\,(odd)} + P_h \, \sigma_{ki}^{h(odd)} \right) + \rho_{ik}^{(odd)} \left(P_e \, \sigma_{ki}^{e(even)} + P_h \, \sigma_{ki}^{h(even)} \right) \Big] \tag{6-9}$$

Using equations (3-31) and (3-32) for σ_{ki} s in equation (6-9) we have

$$\alpha_{11}^{(odd)}(B_1) = 0$$

$$\alpha_{22}^{(odd)}(B_1) = \frac{-\sigma_{32}^{e(even)}}{\sigma_{22}\sigma_{33} - \sigma_{23}\sigma_{32}}\left[2P_e\ \sigma_{32}^{e(odd)} + (P_e + P_h)\,\sigma_{32}^{h(odd)}\right]$$

$$\alpha_{33}^{(odd)}(B_1) = \frac{-\sigma_{32}^{e(even)}}{\sigma_{22}\sigma_{33} - \sigma_{23}\sigma_{32}}\left[2P_e\ \sigma_{23}^{e(odd)} + (P_e + P_h)\,\sigma_{32}^{h(odd)}\right] \qquad (6\text{-}10)$$

Thus on the basis of the Fermi surface model adopted for bismuth, the x-cut sample should not show an Umkehr effect, while the y- and z- cut samples should. By following this procedure through, we have ascertained which of the tensor components are expected to exhibit the effect. Those that do are enclosed in rectangles in the complete scheme below.

$$\hat{\alpha}(B_1) = \begin{vmatrix} \alpha_{11}(B_1) & \alpha_{12}(B_1) & \alpha_{13}(B_1) \\ \alpha_{21}(B_1) & \boxed{\alpha_{22}(B_1)} & \boxed{\alpha_{23}(B_1)} \\ \alpha_{31}(B_1) & \boxed{\alpha_{32}(B_1)} & \boxed{\alpha_{33}(B_1)} \end{vmatrix}$$

$$\hat{\alpha}(B_2) = \begin{vmatrix} \alpha_{11}(B_2) & \boxed{\alpha_{12}(B_2)} & \boxed{\alpha_{13}(B_2)} \\ \boxed{\alpha_{21}(B_2)} & \alpha_{22}(B_2) & \alpha_{23}(B_2) \\ \boxed{\alpha_{31}(B_2)} & \alpha_{32}(B_2) & \alpha_{33}(B_2) \end{vmatrix} \qquad (6\text{-}11)$$

$$\hat{\alpha}(B_3) = \begin{vmatrix} \alpha_{11}(B_3) & \boxed{\alpha_{12}(B_3)} & \alpha_{13}(B_3) \\ \boxed{\alpha_{21}(B_3)} & \alpha_{22}(B_3) & \alpha_{23}(B_3) \\ \alpha_{31}(B_3) & \alpha_{32}(B_3) & \alpha_{33}(B_3) \end{vmatrix}$$

The occurrence of an Umkehr effect in $\alpha_{22}(\pm B_1)$ already discussed in detail here is consistent with these predictions. Furthermore, measurements on the z-axis sample show the existence of an Umkehr effect in $\alpha_{33}(\pm B_1)$ (see figure 5-17) and the plots presented by Gitsu et al (1970) have shown that $\alpha_{11}(B_1)$ does not show an Umkehr effect, as predicted here.

Finally we turn briefly to the interesting problem of how the Umkehr effect and the electron Fermi ellipsoid tilt angle are related. This question can be examined by recourse to equations of the form of (6-10). If the tilt angle is set to zero, μ_4 becomes zero. In this case the expressions for σ_{32}^{I} and $\sigma_{32}^{II,III}$ (see equations (3-31) and (3-32)) show that $\sigma_{32}^{e(even)}$ becomes zero and this leads immediately to the disappearance of the Umkehr effect.

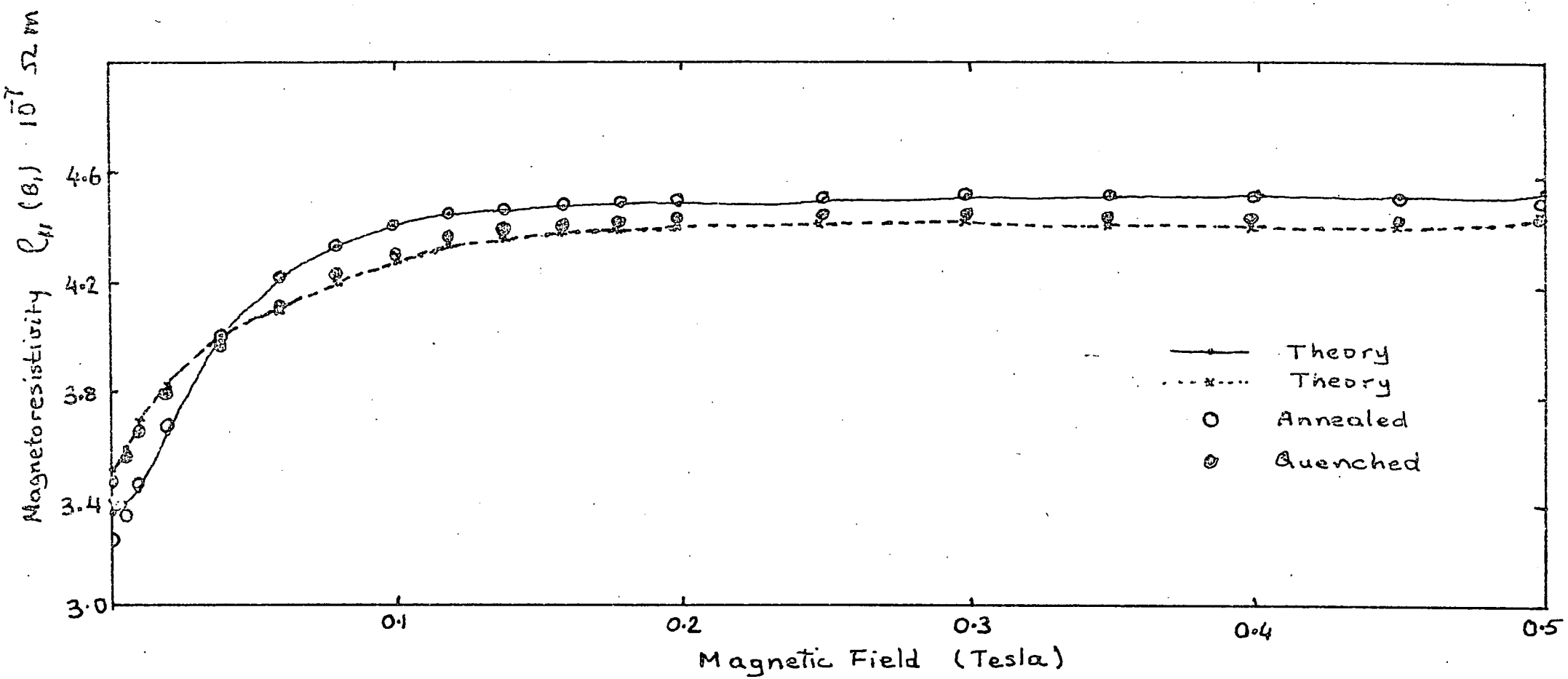

Figure (6-1) : Theoretically computed values for the magneto-resistivity at intermediate magnetic fields are shown in relation to the experimental points.

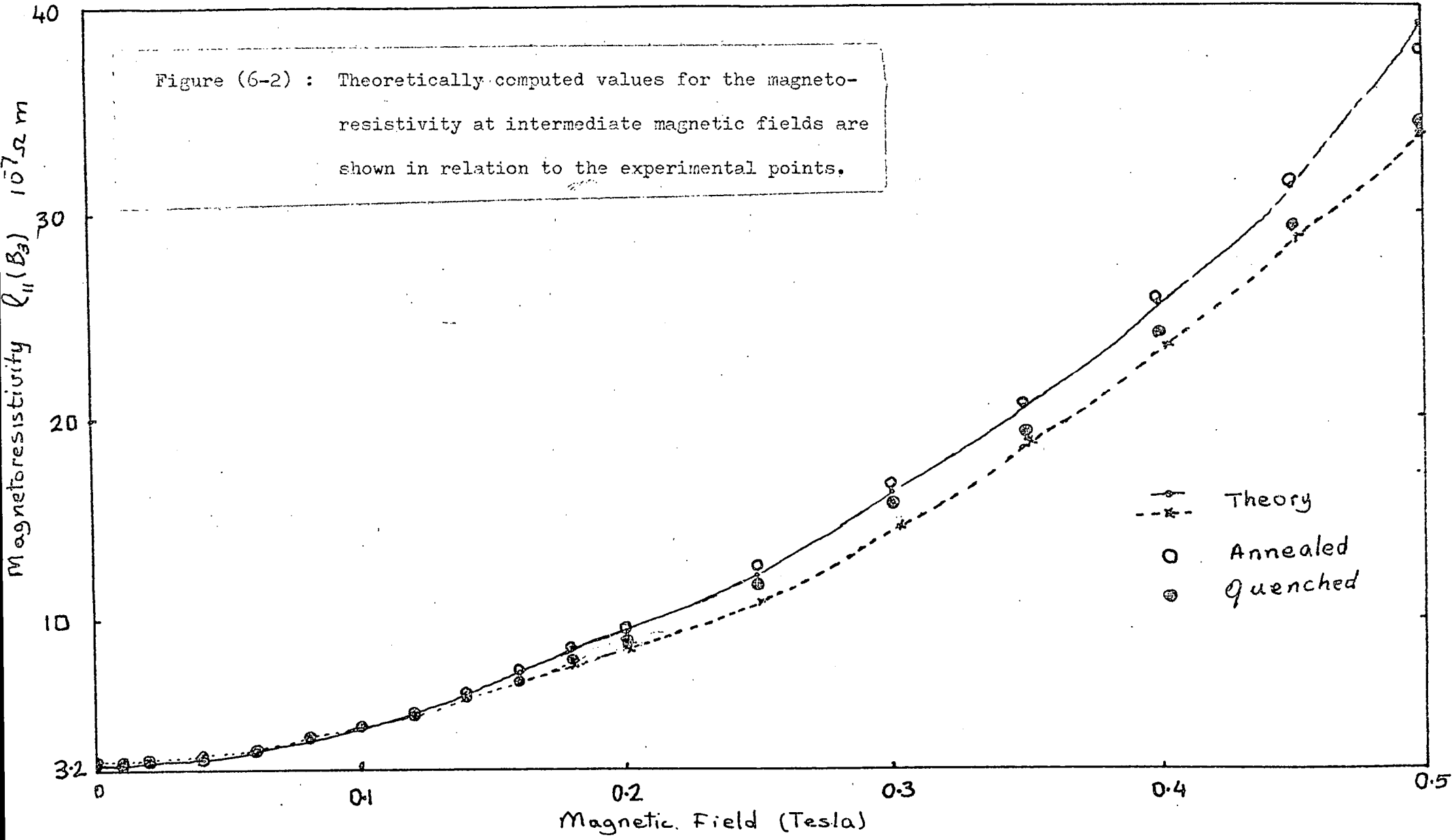

Figure (6-2) : Theoretically computed values for the magneto-resistivity at intermediate magnetic fields are shown in relation to the experimental points.

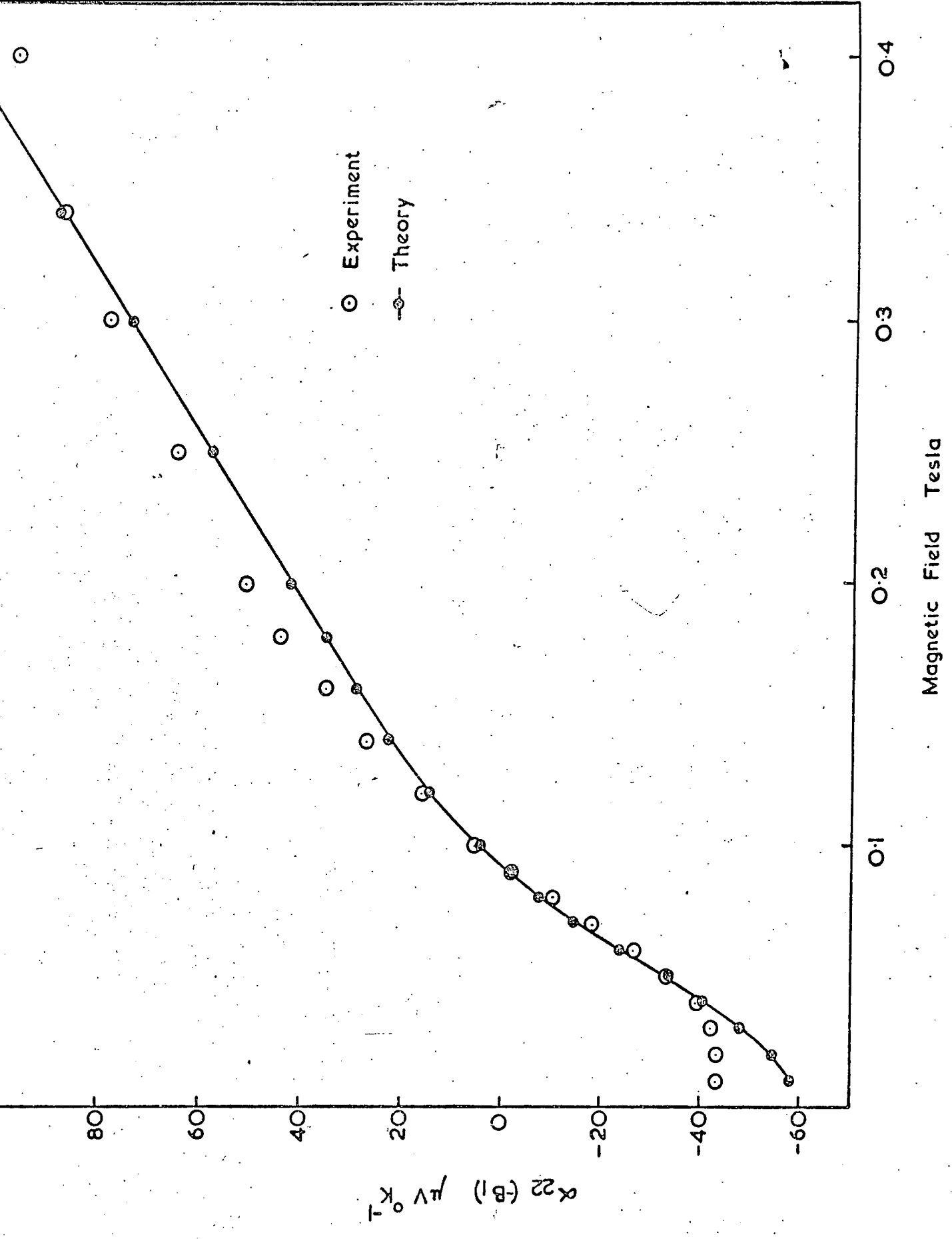

Figure (6-3) : Linear thermomagnetic data for $\alpha_{22}(-B_1)$. The points on the solid line correspond to the theoretically computed values (annealed).

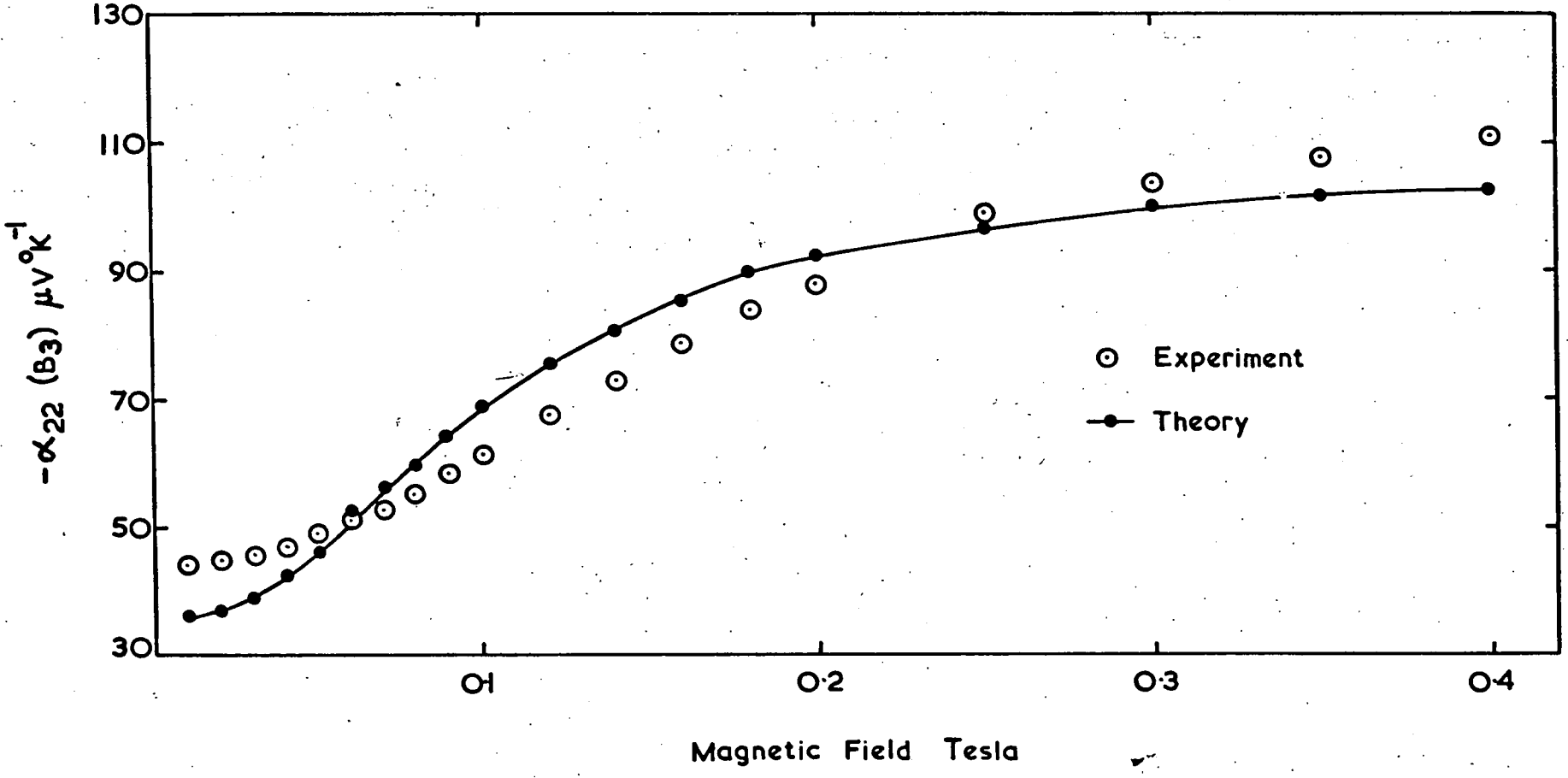

Figure (6-4) : Linear thermomagnetic data for $\alpha_{22}(B_3)$. The points on the solid line correspond to the theoretically calculated values. (annealed).

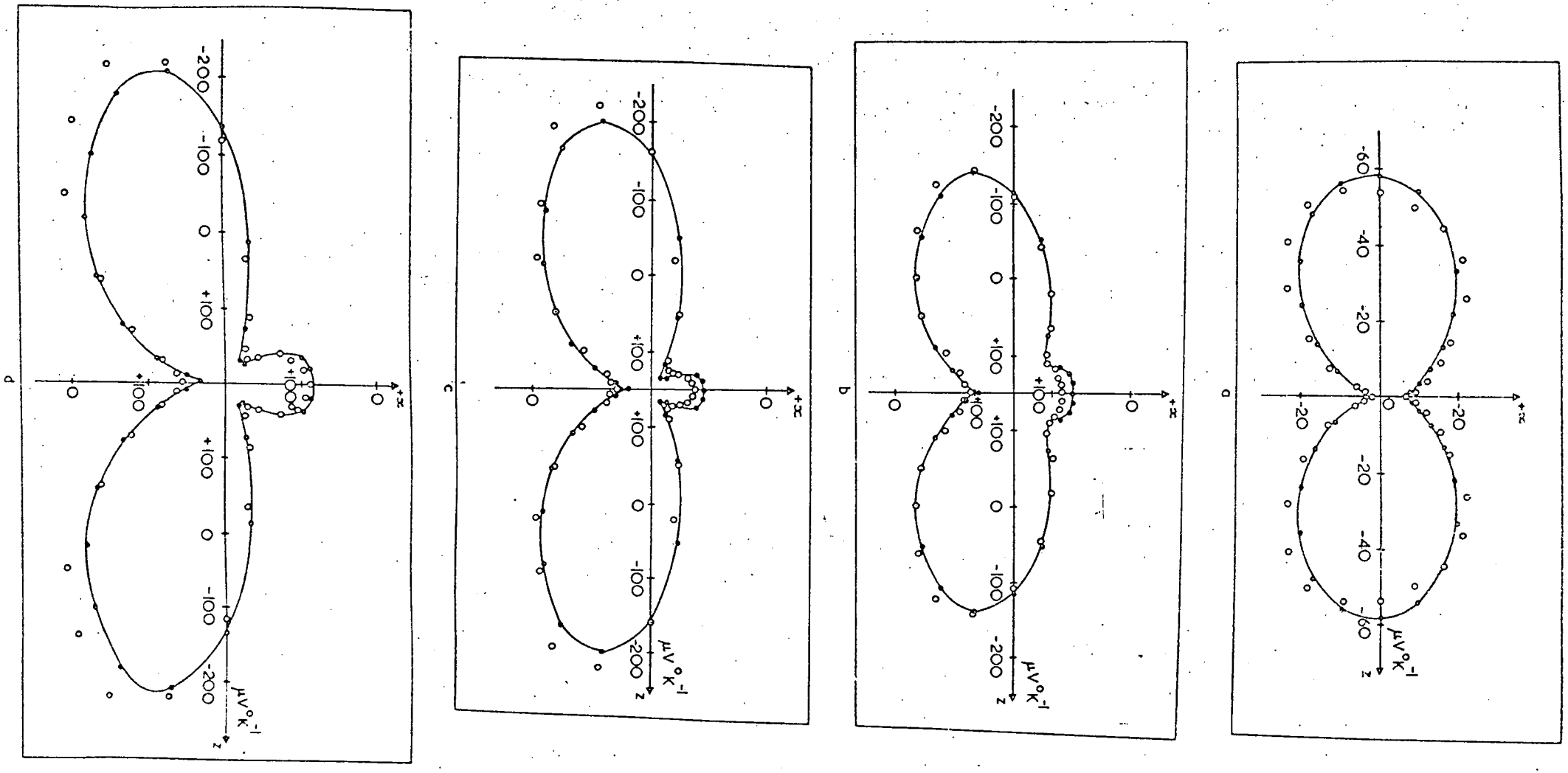

Figure (6-5) : Polar plots of $\alpha_{22}(B)$ in the xz plane for magnetic fields a) 0.075 T, b) 0.38 T, c) 0.68 T (Michenaud et al 1970) and d) 1.00 T (Smith et al 1964). The experimental measurements are marked with open circles. The theoretically computed values are marked with closed circles and the smooth curves are drawn through these.

APPENDIX

```
C      BAND STRUCTURE CALCULATION (LOW FIELD GALVANOMAGNETIC DATA)
       DIMENSION S(8),MAX(8),MIN(8),STEP(8),CO(12),SUM(2),Q(12),Z(12),
      1H(8),SOL(8),WE(12),W(12)
       INTEGER I,J,K,C,U
       REAL SMALL
    1  FORMAT (8E10.0)
   11  FORMAT (12F4.1)
    2  FORMAT (20X,'INITIAL SOLUTIONS FITTED'/ 25X,'MEASURED COEFF'/
      1(2(6E12.3/)))
   10  FORMAT (25X,'CALCULATED COEFF'/ (2(6E12.3/)))
   80  FORMAT (25X,'STEPS'/(8E12.2/))
   59  FORMAT (25X,'SOLUTIONS'/(8E10.2/))
    4  FORMAT (25X,'RATIOES'/ (2(6F12.2/)))
    5  FORMAT(25X,'SUM'/ (2F20.4))
    3  FORMAT (25X,'FINAL SOLUTIONS'/ (3E10.2,F6.2,4E10.2/))
    6  FORMAT (25X,'MEASURED COEFF'/ (2(6E12.3/)))
       READ(5,11) (W(K),K=1,12)
       READ(5,1) (MAX(I),I=1,8)
       READ(5,1) (MIN(I),I=1,8)
   50  READ(5,1,END=99) (S(I),I=1,8)
       READ(5,1) (STEP(I),I=1,8)
       READ(5,1) (CO(I),I=1,12)
       SMALL=0.001
       HK=0.0
       DO 7 I=1,8
       SOL(I)=S(I)
       H(I)=1
    7  CONTINUE
       SUM(1)=0
       SUM(2)=0
       DO 16 C=1,10
       DO 19 U=1,50
       DO 13 I=1,8
       SUM(2)=0
       S(I)=S(I)+STEP(I)
       IF(S(I).GT.MAX(I)) GO TO 15
       IF(S(I).LT.MIN(I)) GO TO 15
       CALL DEV (S,Z)
       DO 18 K=1,12
       Q(K)=(Z(K)/CO(K))
       WE(K)=(Q(K)-1)
       WE(K)=W(K)*WE(K)
       SUM(2)=SUM(2)+WE(K)**2
   18  CONTINUE
       IF (HK.EQ.1.0) GO TO 77
       WRITE(6,2) (CO(K),K=1,12)
       WRITE(6,10) (Z(K),K=1,12)
       WRITE(6,59) (SOL(I),I=1,8)
       WRITE(6,80) (STEP(K),K=1,8)
       WRITE(6,4) (Q(K),K=1,12)
       WRITE(6,5)(SUM(I),I=1,2)
       HK=1.0
   77  IF (SUM(1)-SUM(2))15,14,14
   15  IF(H(I)-25) 21,21,22
   21  STEP(I)=-STEP(I)
       S(I)=SOL(I)
       H(I)=H(I)+1
       GO TO 13
```

```
22   STEP(I)=-0.5*STEP(I)
     S(I)=SOL(I)
     H(I)=1
     GO TO 13
14   IF(SUM(2)-SMALL) 9,9,20
20   SOL(I)=S(I)
     SUM(1)=SUM(2)
13   CONTINUE
19   CONTINUE
     WRITE(6,59) (SOL(I),I=1,8)
     WRITE(6,80) (STEP(K),K=1,8)
     WRITE(6,6) (CO(K),K=1,12)
     WRITE(6,10) (Z(K),K=1,12)
     WRITE(6,4) (Q(K),K=1,12)
     WRITE(6,5)(SUM(I),I=1,2)
16   CONTINUE
9    DO 25 I=1,8
     S(I)=SOL(I)
25   CONTINUE
     SOL(4)=(90.0/3.1416)*ATAN((2.0*SOL(4))/(SOL(2)-SOL(3)))
     WRITE(6,3) (SOL(I),I=1,8)
     WRITE(6,10) (Z(K),K=1,12)
     WRITE(6,6) (CO(K),K=1,12)
     WRITE(6,4) (Q(K),K=1,12)
     WRITE(6,5)(SUM(I),I=1,2)
     GO TO 50
99   STOP
     END
     SUBROUTINE DEV(A,Z)
     DIMENSION A(8),Z(12)
     REAL Q
     Q=1.6
     Z(1)=(2/(A(5)*Q*(A(1)+A(2)+2*A(8)*A(6))))
     Z(2)=(1/(A(5)*Q*(A(3)+A(8)*A(7))))
     Z(3)=(4*(A(1)*A(2)-A(8)*A(6)**2)/(A(5)*Q*(A(1)+A(2)+2*A(8)*A(6))
    1**2))
     Z(4)=(A(3)*(A(1)+A(2))-2*A(8)*A(6)*A(7)-A(4)**2)/(A(5)*Q*(A(1)+A
    1)+2*A(8)*A(6))*(A(3)+A(8)*A(7)))
     Z(5)=(A(3)*(A(1)-A(2))**2+A(4)**2*(5*A(1)-A(2)))/(2*A(5)*Q*(A(1)
    1A(2)+2*A(8)*A(6))**2)
     Z(6)=(1/(2*A(5)*Q))*(A(1)*(3*A(1)*A(3)+A(4)**2)+(2*A(1)+3*A(2))*
    1(A(2)*A(3)-A(4)**2)+8*A(8)*A(7)*A(6)**2-2*((A(1)+A(2))*A(3)-2*
    2A(8)*A(6)*A(7)-A(4)**2)**2/(A(3)+A(8)*A(7)))/(A(1)+A(2)+2*A(8)*A
    3))**2
     Z(7)=(2*(A(1)*A(2)*(A(1)+A(2))+2*A(8)*A(6)**3-4*(A(1)*A(2)-A(8)*
    16)**2)**2/(A(1)+A(2)+2*A(8)*A(6)))/(((A(1)+A(2)+2*A(8)*A(6))**2)
    2A(5)*Q))
     Z(8)=1/(2*A(5)*Q)*(2*A(8)*A(6)*(A(1)+A(2))*(A(3)+A(7))**2+(A(3)*
    1A(1)+A(2))-A(4)**2-2*A(8)*A(6)*(A(3)+2*A(7)))*A(4)**2)/((A(1)+A(
    2+2*A(8)*A(6))*(A(3)+A(8)*A(7))**2)
     Z(9)=(A(1)*A(4)**2)/(A(5)*Q*(A(3)+A(8)*A(7))**2)
     Z(10)=-(A(4)*(A(1)*(A(1)-A(2)))/(A(5)*Q*(A(1)+A(2)+2*A(8)*A(6))
    2**2))
     Z(11)=-(A(4)*(A(3)*(A(1)-A(2))+A(4)**2)/((A(1)+A(2)+2*A(8)*A(6))
    1(A(3)+A(8)*A(7))*2*A(5)*Q))
     Z(12)=-1/(A(5)*Q)*(A(1)*A(2)*(A(4)**2+2*A(8)*A(6)*(A(3)+A(7)))+A
    18)*A(6)**2*((A(1)+A(2))*(A(3)+A(7))-A(4)**2))/((A(1)+A(2)+2*A(8)
    2A(6))**2*(A(3)+A(8)*A(7)))
     RETURN
```

```
C       BISMUTH BAND STRACTURE(POLAR THERMOMAGNETIC DATA)
        DIMENSION S(11),SAX(11),SIM(11),STEP(11),CO(72),SUM(2),Q(72),
       1Z(72),H(11),SOL(11),WE(72),A(5),D(5),SE(9),SH(9),SHT(9),BB(3),
       2RES(9),B(3),ST(9),SET(9),DD(5),W(19)
        REAL SMALL,PE,PH,HK,DELTA,P,FC,FS,TC,TS,PI,PJ,DEG,HH
        INTEGER I,J,K,C,U,N
    1   FORMAT (8E10.0)
    2   FORMAT (20X,'INITIAL SOLUTIONS FITTED'/ 25X,'MEASURED COEFF'/
       1(9E12.2/(10E12.2/)))
    3   FORMAT (25X,'FINAL SOLUTIONS'/(3E11.3,F6.2,5E11.3/))
    4   FORMAT (25X,'RATIOES'/ (9F12.2/(10F12.2/)))
    5   FORMAT(25X,'SUM'/ (2F15.4))
   10   FORMAT (25X,'CALCULATED COEFF'/ (9E12.3/(10E12.3/)))
   11   FORMAT (19F4.0)
   59   FORMAT (25X,'SOLUTIONS'/(10E11.3/))
   80   FORMAT (25X,'STEPS'/(10E10.2/))
    6   FORMAT (25X,'MEASURED COEFF'/ (9E12.3/(10E12.3/)))
        READ(5,11) (W(K),K=1,19)
        READ(5,1) (SAX(I),I=1,10)
        READ(5,1) (SIM(I),I=1,10)
   50   READ(5,1,END=99) (S(I),I=1,10)
        READ(5,1) (STEP(I),I=1,10)
        READ(5,1) (CO(I),I=1,19)
        READ(5,1) HH
        SMALL=0.001
        HK=0.0
        DO 7 I=1,10
        SOL(I)=S(I)
        H(I)=1
    7   CONTINUE
        SUM(1)=0
        SUM(2)=0
        DO 16 C=1,7
        DO 19 U=1,50
        DO 13 I=1,10
        IF(STEP(I).EQ.0.0)GO TO 13
        SUM(2)=0
        S(I)=S(I)+HK*STEP(I)
        IF(STEP(I).EQ.0.0) GO TO 13
        IF(S(I).GT.SAX(I)) GO TO 15
        IF(S(I).LT.SIM(I)) GO TO 15
        DO 36 J=1,5
        A(J)=S(J)
   36   CONTINUE
        D(1)=S(6)
        D(2)=D(1)
        D(3)=S(7)
        D(4)=0.0
        D(5)=3.0*S(5)
        PE=S(9)
        PH=S(10)
        FC=0.0
        FS=1.0
        BB(2)=0.0
        B(2)=0.0
```

```
      DEG=-0.1745
      DO 100 K=1,19
      DEG=DEG+0.1745
       TC=COS(DEG)
      TS=SIN(DEG)
      B(1)=HH*FS*TC
      BB(1)=-B(1)
      B(3)=HH*FS*TS
      BB(3)=-B(3)
      DO 47 J=1,9
      SE(J)=0.0
      SH(J)=0.0
      SET(J)=0.0
      SHT(J)=0.0
      RES(J)=0.0
      ST(J)=0.0
47    CONTINUE
      CALL DEV(B,D,SH)
      CALL DEV(BB,A,SE)
      DO 48 J=1,9
      SHT(J)=SHT(J)+SH(J)
      SET(J)=SET(J)+SE(J)
      SE(J)=0.0
48    CONTINUE
      CALL SEV(BB,A,SE,1.0)
      DO 49 J=1,9
      SET(J)=SET(J)+SE(J)
      SE(J)=0.0
49    CONTINUE
      CALL SEV(BB,A,SE,-1.0)
      DO 60 J=1,9
      SET(J)=SET(J)+SE(J)
60    CONTINUE
      DO 51 J=1,9
      ST(J)=SET(J)+SHT(J)
51    CONTINUE
      DELTA=ST(1)*(ST(2)*ST(3)-ST(5)*ST(8))+ST(4)*(ST(6)*ST(5)-ST(7)*
     1ST(3))+ST(9)*(ST(7)*ST(8)-ST(2)*ST(6))
      RES(2)=(ST(1)*ST(3)-ST(6)*ST(9))/DELTA
      RES(5)=(ST(4)*ST(6)-ST(1)*ST(8))/DELTA
      RES(7)=(ST(8)*ST(9)-ST(3)*ST(4))/DELTA
      Z(K)=RES(7)*(PE*SET(4)+PH*SHT(4))+RES(2)*(PE*SET(2)+PH*SHT(2))+
     1RES(5)*(PE*SET(8)+PH*SHT(8))
100   CONTINUE
      DO 18 K=1,19
      Q(K)=(Z(K)/CO(K))
      WE(K)=(Q(K)-1)
      WE(K)=W(K)*WE(K)
      SUM(2)=SUM(2)+WE(K)**2
18    CONTINUE
      IF(HK.EQ.0.0) SUM(1)=SUM(2)
      IF (SUM(1)-SUM(2))15,14,14
15    IF(H(I)-10) 21,21,22
21    STEP(I)=-STEP(I)
      S(I)=SOL(I)
```

```
      H(I)=H(I)+1
      GO TO 13
   22 STEP(I)=-0.5*STEP(I)
      H(I)=1
      S(I)=SOL(I)
      GO TO 13
   14 IF(SUM(2)-SMALL) 9,9,20
   20 SOL(I)=S(I)
      HK=1.0
      SUM(1)=SUM(2)
   13 CONTINUE
   19 CONTINUE
      WRITE(6,59) (SOL(I),I=1,10)
      WRITE(6,80) (STEP(K),K=1,10)
      WRITE(6,4) (Q(K),K=1,19)
      WRITE(6,5)(SUM(I),I=1,2)
   16 CONTINUE
    9 DO 25 I=1,10
      S(I)=SOL(I)
   25 CONTINUE
      WRITE(6,3) (SOL(I),I=1,10)
      WRITE(6,6) (CO(K),K=1,19)
      WRITE(6,10) (Z(K),K=1,19)
      WRITE(6,4) (Q(K),K=1,19)
      WRITE(6,5)(SUM(I),I=1,2)
      GO TO 50
   99 STOP
      END
```

```
C       BISMUTH BAND STRACTURE(HIGH FIELD GALVANOMAGNETIC DATA)
        DIMENSION S(15),SAX(15),SIM(15),STEP(15),CO(19),SUM(2),Q(19),
       1Z(19),H(15),SOL(15),WE(19),A(5),D(5),SE(9),SH(9),SHT(9),BB(3),
       2RES(19),B(3),ST(9),SET(9),DD(5),W(19),HH(19)
        REAL SMALL,PE,PH,HK,DELTA,P,FC,FS,TC,TS,PI,PJ
        INTEGER I,J,K,C,U,N
    1   FORMAT (8E10.0)
    2   FORMAT (20X,'INITIAL SOLUTIONS FITTED'/ 25X,'MEASURED COEFF'/
       1(9E12.2/(10E12.2/)))
    3   FORMAT (25X,'FINAL SOLUTIONS'/(3E10.2,F6.2,6E10.3/))
    4   FORMAT (25X,'RATIOS'/ (9F12.2/(10F12.2/)))
    5   FORMAT(25X,'SUM'/ (2F15.4))
   10   FORMAT (25X,'CALCULATED COEFF'/ (9E12.3/(10E12.3/)))
   11   FORMAT (19F4.0)
    6   FORMAT (25X,'MEASURED COEFF'/ (9E12.3/(10E12.3/)))
   59   FORMAT (25X,'SOLUTIONS'/(10E10.2/))
   80   FORMAT (25X,'STEPS'/(10E10.2/))
        READ(5,11) (W(K),K=1,19)
        READ(5,1) (HH(K),K=1,19)
        READ(5,1) (SAX(I),I=1,8)
        READ(5,1) (SIM(I),I=1,8)
   50   READ(5,1,END=99) (S(I),I=1,8)
        READ(5,1) (STEP(I),I=1,8)
        READ(5,1) (CO(I),I=1,19)
        SMALL=0.001
        HK=0.0
        DO 7 I=1,8
        SOL(I)=S(I)
        H(I)=1
    7   CONTINUE
        WRITE(6,59) (SOL(I),I=1,8)
        B(1)=0.0
        BB(1)=0.0
        B(2)=0.0
        BB(2)=0.0
        SUM(1)=0
        SUM(2)=0
        DO 16 C=1,5
        DO 19 U=1,50
        DO 13 I=1,8
        SUM(2)=0
        S(I)=S(I)+HK*STEP(I)
        IF(S(I).GT.SAX(I)) GO TO 15
        IF(S(I).LT.SIM(I)) GO TO 15
        DO 36 J=1,5
        A(J)=S(J)
   36   CONTINUE
        D(1)=S(6)
        D(2)=D(1)
        D(3)=S(7)
        D(4)=0.0
        D(5)=3.0*S(5)
        DO 100 K=1,19
        B(3)=HH(K)
        BB(3)=-B(3)
```

```
      DO 47 J=1,9
      SE(J)=0.0
      SH(J)=0.0
      SET(J)=0.0
      SHT(J)=0.0
      ST(J)=0.0
   47 CONTINUE
      CALL DEV(B,D,SH)
      DO 66 J=1,9
      SHT(J)=SHT(J)+SH(J)
      SH(J)=0.0
   66 CONTINUE
      CALL DEV(BB,A,SE)
      DO 48 J=1,9
      SET(J)=SET(J)+SE(J)
      SE(J)=0.0
   48 CONTINUE
      CALL SEV(BB,A,SE,1.0)
      DO 49 J=1,9
      SET(J)=SET(J)+SE(J)
      SE(J)=0.0
   49 CONTINUE
      CALL SEV(BB,A,SE,-1.0)
      DO 60 J=1,9
      SET(J)=SET(J)+SE(J)
   60 CONTINUE
      DO 51 J=1,9
      ST(J)=SET(J)+SHT(J)
   51 CONTINUE
      DELTA=ST(1)*(ST(2)*ST(3)-ST(5)*ST(8))+ST(4)*(ST(6)*ST(5)-ST(7)*
     1ST(3))+ST(9)*(ST(7)*ST(8)-ST(2)*ST(6))
      RES(K)=(ST(2)*ST(3)-ST(8)*ST(5))/DELTA
  100 CONTINUE
      DO 18 K=1,19
      Q(K)=(RES(K)/CO(K))
      WE(K)=(Q(K)-1)
      WE(K)=W(K)*WE(K)
      SUM(2)=SUM(2)+WE(K)**2
   18 CONTINUE
      IF(HK.EQ.1.0) GO TO 8
      HK=1.0
      SUM(1)=SUM(2)
      WRITE(6,10) (RES(K),K=1,19)
    8 IF (SUM(1)-SUM(2))15,14,14
   15 IF(H(I)-10) 21,21,22
   21 STEP(I)=-STEP(I)
      S(I)=SOL(I)
      H(I)=H(I)+1
      GO TO 13
   22 STEP(I)=-0.5*STEP(I)
      H(I)=1
      S(I)=SOL(I)
      GO TO 13
   14 IF(SUM(2)-SMALL) 9,9,20
   20 SOL(I)=S(I)
```

```
      SUM(1)=SUM(2)
   13 CONTINUE
   19 CONTINUE
      WRITE(6,6) (CO(K),K=1,19)
      WRITE(6,10) (RES(K),K=1,19)
      WRITE(6,59) (SOL(I),I=1,8)
      WRITE(6,80) (STEP(K),K=1,8)
      WRITE(6,4) (Q(K),K=1,19)
      WRITE(6,5)(SUM(I),I=1,2)
   16 CONTINUE
    9 DO 25 I=1,8
      S(I)=SOL(I)
   25 CONTINUE
      SOL(4)=(90.0/3.1416)*ATAN((2.0*SOL(4))/(SOL(2)-SOL(3)))
      WRITE(6,3) (SOL(I),I=1,8)
      WRITE(6,6) (CO(K),K=1,19)
      WRITE(6,4) (Q(K),K=1,19)
      WRITE(6,10) (RES(K),K=1,19)
      WRITE(6,5)(SUM(I),I=1,2)
      GO TO 50
   99 STOP
      END
```

```
      SUBROUTINE DEV(B,A,S)
      DIMENSION B(3),A(5),S(9)
      REAL G,V,Q
      Q=1.6E-19
      V=A(1)*(A(2)*A(3)-A(4)**2)
      G=(1.0+(V/A(1))*B(1)**2+A(1)*(A(3)*B(2)**2-2*A(4)*B(2)*B(3)+A(2)*
     1B(3)**2))
      S(1)=((A(1)+V*B(1)**2)/G)*A(5)*Q
      S(2)=((A(2)+V*B(2)**2)/G)*A(5)*Q
      S(3)=((A(3)+V*B(3)**2)/G)*A(5)*Q
      S(4)=((-A(1)*(A(4)*B(2)-A(2)*B(3))+V*B(1)*B(2))/G)*A(5)*Q
      S(5)=((A(4)+(V/A(1))*B(1)+V*B(2)*B(3))/G)*A(5)*Q
      S(6)=((A(1)*(A(3)*B(2)-A(4)*B(3))+V*B(1)*B(3))/G)*A(5)*Q
      S(7)=((A(1)*(A(4)*B(2)-A(2)*B(3))+V*B(1)*B(2))/G)*A(5)*Q
      S(8)=((A(4)-(V/A(1))*B(1)+V*B(2)*B(3))/G)*A(5)*Q
      S(9)=((-A(1)*(A(3)*B(2)-A(4)*B(3))+V*B(3)*B(1))/G)*A(5)*Q
      RETURN
      END
```

```
      SUBROUTINE SEV(B,A,S,P)
      DIMENSION B(3),A(5),S(9)
      REAL P,G,V,Q
      Q=1.6E-19
      V=A(1)*(A(2)*A(3)-A(4)**2)
      G=(1.0+0.25*(3*A(1)*A(3)+(V/A(1)))*B(1)**2+0.25*(A(1)*A(3)+
     13*(V/A(1)))*B(2)**2+A(1)*A(2)*B(3)**2-P*0.864*(A(1)*A(3)-(V/A(1)))
     2*B(1)*B(2)+A(1)*A(4)*B(2)*B(3)-1.73*P*A(1)*A(4)*B(3)*B(1))
      S(1)= (0.25*(A(1)+3*A(2)+4*V*B(1)**2)/G)*A(5)*Q
      S(2)= (0.25*(3*A(1)+A(2)+4*V*B(2)**2)/G)*A(5)*Q
      S(3)=((A(3)+V*B(3)**2)/G)*A(5)*Q
      S(4)=((0.432*P*(A(1)-A(2))-A(1)*A(4)*(0.864*P*B(1)-0.5*B(2))+A(1)
     1*A(2)*B(3)+V*B(1)*B(2))/G)*A(5)*Q
      S(5)=((-0.5*A(4)+0.25*(3*A(1)*A(3)+(V/A(1)))*B(1)-0.432*P*(A(1)*
     1A(3)-(V/A(1)))*B(2)-0.864*P*A(1)*A(4)*B(3)+V*B(2)*B(3))/G)*A(5)*Q
      S(6)=((0.864*P*A(4)-0.432*P*(A(1)*A(3)-(V/A(1)))*B(1)+0.25*(A(1)
     1*A(3)+3*(V/A(1)))*B(2)+0.5*A(1)*A(4)*B(3)+V*B(3)*B(1))/G)*A(5)*Q
      S(7)=((0.432*P*(A(1)-A(2))+A(1)*A(4)*(0.864*P*B(1)-0.5*B(2))-
     1A(1)*A(2)*B(3)+V*B(1)*B(2))/G)*A(5)*Q
      S(8)=((-0.5*A(4)-0.25*(3*A(1)*A(3)+(V/A(1)))*B(1)+0.432*P*(A(1)
     1*A(3)-(V/A(1)))*B(2)+0.864*P*A(1)*A(4)*B(3)+V*B(2)*B(3))/G)*A(5)*Q
      S(9)=((0.864*P*A(4)+0.432*P*(A(1)*A(3)-(V/A(1)))*B(1)-0.25*(A(1)
     1*A(3)+3*(V/A(1)))*B(2)-0.5*A(1)*A(4)*B(3)+V*B(3)*B(1))/G)*A(5)*Q
      RETURN
      END
```

REFERENCES

Abeles, B. and Meiboom, S., 1954, Phys. Rev., 95, 31.

Abeles, B. and Meiboom, S., 1956, Phys. Rev., 101, 544.

Aubrey, J.E. and Chambers, R.G., 1957, J. Phys. Chem. Solids 3, 128.

Aubrey, J.E., 1961, J. Phys. Chem. Solids 19, 321.

Aubrey, J.E., 1971, J. Phys. F: Metal Phys., 1, 493.

Bhagavantam, S., 1966, "Crystal Symmetry and Physical Properties" (Academic Press, London & New York).

Bhargava, R.N., 1967, Phys. Rev. 156, 785.

Blackman, L.C.F., Saunders, G.A. and Ubbelohde, A.R., 1961, Proc. Phys. Soc. 78, 1048.

Boyle, W.S. and Brailsford, A.D., 1960, Phys. Rev. 120, 1943.

Brandt, N.B., 1960, Sov. Phys. JETP 11, 975.

Brandt, N.B., Dolgolenko, T.F. and Stupuchenko, N.N., 1963, Zh. Eksp. Teor. Fiz. 45, 1319.
1964, Sov. Phys. JETP. 18, 908 .

Brown, R.D., Hartman, R.L. and Koenig, S.H. 1968, Phys. Rev. 172, 5981.

Burton, J.J. and Lazarus, D., 1970, Phys. Rev. B2, 787.

Cohen, M.H., Falicov, L.M. and Golin, S., 1964, IBM. J. Res Dev. 8, 215.

Corbett, J.W., 1966, "Electron Radiation Damage in Semiconductors and Metals" Academic Press, P.162.

Damask, A.C. and Dienes, G.J., 1963, "Point Defects in Metals" (Gordon and Breach).

Davidon, W.C., 1959, Argonne National Laboratory Report No. ANL-5990 Rev. Phys. and Math. TID, 14th.ed.

Drabble, J.R. and Wolfe, R., 1956, Proc. Phys. Soc., B69, 1101.

Erdman, R.J. and Praglin, J., 1964, Instrument Society of America, 19th. Annual ISA Conference and exhibit, New York.

Ettingshausen, A. and Nernst, W., 1886, Wied. Ann. 29, 343.

Freedman, S.J. and Juretschke, H.J., 1961, Phys. Rev. 124, 1379.

Fuchser, T.D., Mackey H.J. and Sybert, J.R., 1970, Phys. Rev. B2, 3863.

Fumi, F.G., 1952, Nuovo Cimento IX, 739.

Gallo, C.F., Chandrasekhar, B.S. and Sutter, P.H., 1963, J. Appl. Phys. 34, 144.

Galt, J.K., Yager, W.A., Merritt, F.R. and Celtin, B.B., 1959, Phys. Rev. 114, 1396.

Gitsu, D.V., Muntyanu, F.M. and Fedorko, A.S., 1970, Phys. Stat. Sol. 42, 173.

Giura, M., Markon, R., Papa, T. and Wanderlingh, F., 1967, Nuovo Cimento 51 B, 150.

Gruneisen, E. and Gielessen, J., 1936, Ann. Physik 26, 449., 27, 243.

Hartman, R., 1969, Phys. Rev. 181, 1070.

Herring, C., 1955, Bell Syst. Tech. Jour. 34, 237.

Herring, C. and Vogt, E., 1956, Phys. Rev. 101, 944.

Hurle, D.T.J., 1960, Ph.D. Thesis, University of Southampton, (Part I and II).

Jeavons, A.P., 1969, Ph.D. Thesis, University of Durham.

Jeavons, A.P. and Saunders, G.A., 1969, Proc. Roy. Soc. A 310, 415.

Jones, H., 1936, Proc. Roy. Soc., A 147, 653.

Juretschke, H.J., 1952, Acta Cryst. 5, 148.

Juretschke, H.J., 1955, Acta Cryst. 8, 716.

Khaikin, M.S. and Edel'man, V.S., 1965, Zh Eskp. Teor. Fiz., 49, 1695. 1966, Sov. Phys. JETP, 22, 1159 .

Korolyuk, A.P., 1966, Sov. Phys. JETP, 22, 701.

Lax, B., Mavroides, J.G., Zeiger, H.J. and Keyes, R.J., 1960, Phys. Rev. Letters, 5, 241.

Mackey H.J. and Sybert, J.R., 1969, Phys. Rev. 180, 678.

Michenaud, J.P., Streydio, J.M., Issi, J.P. and Luyckx, A., 1970, Solid State Commun. 8, 455.

Okada, J., 1955, Mem. Fac. Sci. Kyushu Univ. B1, 168.

Oktu, O., 1967, Ph.D. Thesis, University of Durham.

Oktu, O. and Saunders, G.A., 1967, Proc. Phys. Soc. 91, 156.

Palmer, T.M., 1966, Electr. Engng., 38, 467.

Reneker, D.H., 1959, Phys. Rev. 115, 303.

Saunders, G.A. and Oktu, O., 1968, J. Phys. Chem. Solids, 29, 327.

Saunders, G.A., 1970, "Modern Aspects of Graphite Technology", ed. Blackman, L.C.F. Academic Press, P.79.

Shoenberg, D., 1939, Proc. Roy. Soc. A 170, 341.

Smith, G.E., Wolfe, R. and Hasko, S.E., 1964, Proc. Int. Conf. Semiconductors Physics, Paris, P. 399.

Smith, G.E., 1959, Phys. Rev. 115, 1561.

Stout, M.B., 1960, "Basic Electrical Measurements" (Prentice Hall), Chap. 7.

Volger, J., 1950, Phys. Rev., 79, 1023.

Vickers, W. and Greenough, G.B., 1956, Nature, 178, 536.

Wilson, A.H., 1959, "The theory of metals" (London, Cambridge University Press), P. 208 ff.

Zitter, R.N., 1962, Phys. Rev., 127, 1471.

PUBLICATIONS

1) The elastic constants and interatomic binding in yttria - stabilized zirconia

N.G. Pace, G.A. Saunders, Z. Sümengen and J.S. Thorp

J. Mat. Sci., 4, 1106, (1969)

2) The elastic constants and interatomic binding forces in arsenic

N.G. Pace, G.A. Saunders and Z. Sümengen

J. Phys. Chem. Solids, 31, 1467, (1970)

3) Elastic wave propagation in $Bi_{1.60}Sb_{0.40}Te_3$ and Bi_2Te_3

Y.C. Akgoz, G.A. Saunders and Z. Sümengen

J. Mat. Sci., (in press)

4) Low field thermomagnetic power tensor in bismuth

Z. Sümengen and G.A. Saunders

Solid State Commun., (in press)

5) The thermomagnetic tensor and the Umkehr effect in Bismuth

Z. Sümengen and G.A. Saunders

(Submitted to J. Phys. I: Metal Phys.)

6) Quenching effects on the magnetoresistivity and thermoelectric power tensor components of bismuth

G.A. Saunders and Z. Sümengen

(in preparation)